

QUARTERLY REPORT of

RTRI

May 2023 Vol. 64 No. 2
CONTENTS

Design and Maintenance Technology in the Field of Signal Communication

PERSPECTIVE

- 77 Trends in Research and Development Activities Related to Railway Signalling and Telecommunication Systems H.ARAI, M.FUKUDA

PAPERS

- 90 Configuration and Safety Confirmation Method of Image Processing System Applicable to Signalling Systems
..... A.GION, T.ICHIKAWA, H.MUKOJIMA, N.NAGAMINE, M.FUKUDA, T.ITAGAKI
- 96 Lifetime Estimation of Electronic Signalling Equipment Based on Sensing Data from Usage Environment H.FUJITA, K.TSUBAKI, K.TAKASAKI, N.OKO
- 103 Verification of the Applicability of Fifth Generation Mobile Communication Systems to Railway Operations
... K.NAKAMURA, T.KITANO, K.KAWASAKI, T.OOMI, K.FUJISHIMA, S.ICHIKAWA

Recent Research on Railway-specific Dynamic Issues

PERSPECTIVE

- 81 Recent Research on Railway-specific Dynamic Issues F.UEHAN

PAPERS

- 109 Analytical Study on the Influence of Friction on Unstable Oscillation of Pantograph
..... Y.AMANO, S.KOBAYASHI
- 115 Structural Performance Evaluation of Existing Bridges Based on Acceleration Monitoring
..... M.TOKUNAGA, M.IKEDA
- 121 Development of Simulator to Accurately Reproduce Snow Accretion Phenomenon for Railway Vehicles Traveling in Snowy Areas ... K.MUROTANI, K.NAKADE, Y.KAMATA

Acoustics and Aerodynamics

PERSPECTIVE

- 86 Recent Studies on Railway Aerodynamics S.SAITO

PAPERS

- 129 Measures Against Snow Accretion Around Shinkansen Bogies Using Running Wind
..... H.TAKAMI, Y.ARAKI, K.MUROTANI, H.ISHII, Y.KAMATA
- 135 Reducing Micro-pressure Waves Using Train Nose Optimization Based on Linear Acoustic Theory T.MIYACHI, H.OKUBO, K.KIKUCHI
- 142 Method to Evaluate Aerodynamic Bogie Noise from Shinkansen High-speed Trains by Considering Acoustic Fields N.YAMAZAKI, M.NAKAYAMA, T.NISHIURA
- 148 Summaries of RTRI REPORT (in Japanese)
- 150 Annual Index: Subjects Vol.64, No.1-No.2 (2023)



CONTENTS

PERSPECTIVES

- 77 Trends in Research and Development Activities Related to Railway Signalling and Telecommunication Systems H.ARAI, M.FUKUDA
81 Recent Research on Railway-specific Dynamic Issues F.FUEHAN
86 Recent Studies on Railway Aerodynamics S.SAITO

PAPERS

- 90 Configuration and Safety Confirmation Method of Image Processing System Applicable to Signalling Systems A.GION, T.ICHIKAWA, H.MUKOJIMA, N.NAGAMINE, M.FUKUDA, T.ITAGAKI
96 Lifetime Estimation of Electronic Signalling Equipment Based on Sensing Data from Usage Environment H.FUJITA, K.TSUBAKI, K.TAKASAKI, N.OKO
103 Verification of the Applicability of Fifth Generation Mobile Communication Systems to Railway Operations K.NAKAMURA, T.KITANO, K.KAWASAKI, T.OOMI, K.FUJISHIMA, S.ICHIKAWA
109 Analytical Study on the Influence of Friction on Unstable Oscillation of Pantograph Y.AMANO, S.KOBAYASHI
115 Structural Performance Evaluation of Existing Bridges Based on Acceleration Monitoring M.TOKUNAGA, M.IKEDA
121 Development of Simulator to Accurately Reproduce Snow Accretion Phenomenon for Railway Vehicles Traveling in Snowy Areas K.MUROTANI, K.NAKADE, Y.KAMATA
129 Measures Against Snow Accretion Around Shinkansen Bogies Using Running Wind H.TAKAMI, Y.ARAKI, K.MUROTANI, H.ISHII, Y.KAMATA
135 Reducing Micro-pressure Waves Using Train Nose Optimization Based on Linear Acoustic Theory T.MIYACHI, H.OKUBO, K.KIKUCHI
142 Method to Evaluate Aerodynamic Bogie Noise from Shinkansen High-speed Trains by Considering Acoustic Fields N.YAMAZAKI, M.NAKAYAMA, T.NISHIURA

SUMMARIES

- 148 Summaries of RTRI REPORT (in Japanese)

ANNUAL INDEX

- 150 Annual Index: Subjects Vol.64, No.1-No.2 (2023)

Editorial Board

Chairperson: Kimitoshi ASHIYA

Co-Chairperson: Toru MIYAUCHI

Editors: Shinya FUKAGAI, Ryohei IKEDA, Masateru IKEHATA, Yasutaka MAKI, Nozomi NAGAMINE, Erimitsu SUZUKI, Munemasa TOKUNAGA, Masahiro TSUJIE, Kazuhide YASHIRO

Copyright © 2023 Railway Technical Research Institute, Tokyo JAPAN All rights reserved.

Trends in Research and Development Activities Related to Railway Signalling and Telecommunication Systems

Hideki ARAI

Signalling and Operation Systems Technology Division

Mitsuyoshi FUKUDA

Information and Communication Technology Division

The Railway Technical Research Institute (RTRI) partially revised its organization to create a focus on railway system innovation with digital technology on April 1, 2022. In order to accelerate R&D for a digital railway innovation, two divisions, Signalling and Operation Systems Technology Div. and Information and Communication Technology Div. were newly established. This paper introduces the trends in R&D activities related to signalling and telecommunication systems.

Key words: digital technology, RESEARCH 2025, autonomous train operation, digital maintenance

1. Introduction

The environment surrounding the railway business has changed significantly due to the spread of COVID-19, and improved safety, including resilience against natural disasters, as well as innovation in the railway system using digital technology and the realization of carbon neutrality by 2050 have become urgent issues. Based on these factors, as of April 1, 2022, the Railway Technology Research Institute (RTRI) reorganized itself in order to create research and development results more efficiently and quickly, and to operate our businesses more efficiently [1].

In order to accelerate research and development in railway system innovation using the above digital technologies, the former Signalling and Telecommunications Technology Division was abolished, and the following two divisions were newly established: the Signalling and Operations Technology Division, which now forms the core of research and development that contributes to the automation and autonomy of train operations; and the Information and Communication Technology Division, which is now the core of research and development that promotes the use of digital technologies across fields, and contributes to unmanned and manpower/labor-conserving railway systems (Fig. 1).

The Signalling and Operations Technology Division consists of three laboratories (Signalling Systems, Train Control Systems, Transport Operation Systems), where it contributes to the safety, reliability, convenience, and energy conservation of railways through research and development for high safety signal systems, wireless train control systems, and automatic operations; construction support and safety evaluation of those systems; and research and development and technical support relating to transport planning, driving curves that include energy-conserving driving, and traffic rescheduling. Additionally, the Division aims to quickly provide results that contribute to labor-conserving, unmanned, and equipment-conserving railway operations by integrating the unique technology relating to railway operation and safety control that we have accumulated to date with ICT and security technology.

The Information and Communication Technology Division consists of three laboratories (Data Analytics, Image Analysis, Telecommunications and Networking), where it works to achieve manpower-conserving, unmanned, and labor-conserving railway operations as well as maintenance using research and development on data analysis in each railway field, analysis technologies and analysis infrastruc-

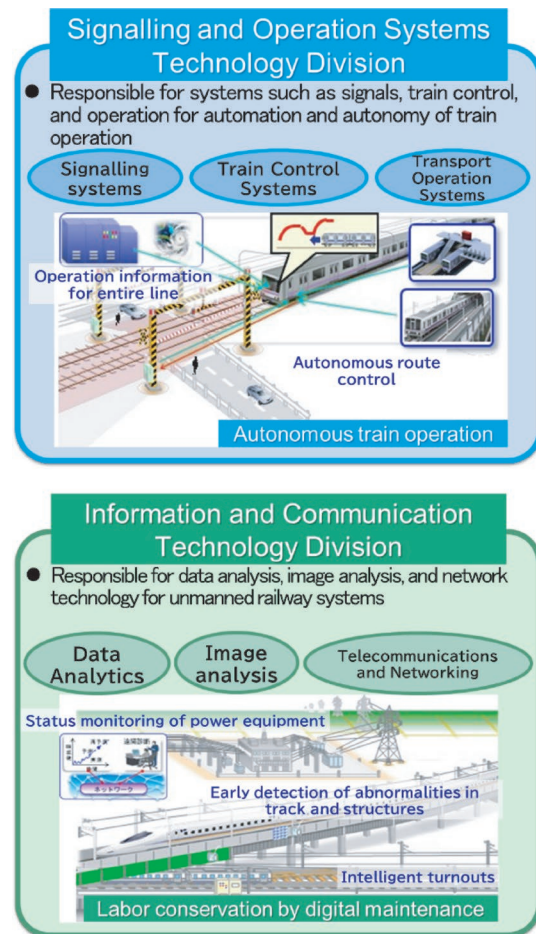


Fig. 1 Signalling and Operations Technology Division and Information and Communication Technology Division

tures that are common to each field, and system construction using various sensors such as cameras and LiDAR. The Division also contributes to equipment conservation and improved convenience through research and development of methods for understanding and evaluating characteristics under railway environments such as 5G/

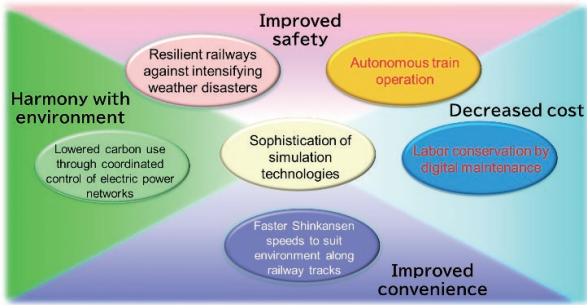


Fig. 2 Research and development for the future of railways (RESEARCH 2025)

Beyond 5G, and applying public communication lines, including the latest wireless technology, to railway operation businesses.

Additionally, for research and development that is being conducted for the future of railways that is being advanced as part of RESEARCH 2025, which is the basic five-year plan of the RTRI from FY2020 to FY2024 (Fig. 2), the Signalling and Operations Technology Division and Information and Communication Technology Division have respectively been promoting research and development intensively in the areas of autonomous train operation and labor conservation through digital maintenance.

In this paper, we describe our research and development efforts for the future of railways, and our priority research and development efforts in the field of signal communication.

2. Research and development efforts for the future of railways

2.1 Autonomous train operation

An autonomous train operation system enables trains to operate autonomously, safely, and flexibly while controlling wayside facilities based on digital information relating to conditions on and along railway tracks, passenger flow, disaster prevention, maintenance, and electricity. We are working on the following five developments as the main technologies for constructing this system [2] (Fig. 3).

- (1) Detection of abnormalities on and along railway tracks using images and radar
- (2) Algorithm that judges whether or not trains can be operated by integrating information on the status of trains on and along railway tracks and status of vehicles

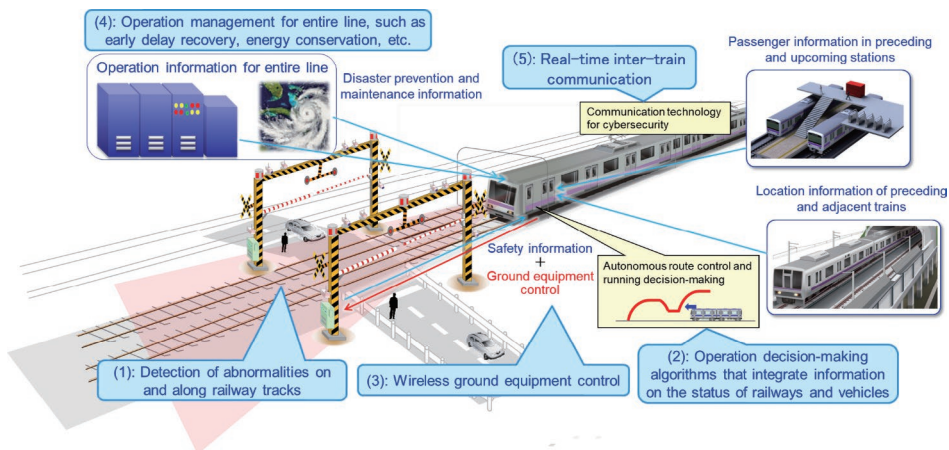


Fig. 3 Autonomous train operation

- (3) Autonomous control of ground equipment from the train using wireless technology
- (4) Wide-area operation management algorithm for prevention of the spread of delay and early delay recovery, energy conservation, etc.
- (5) Real-time inter-train communication that considers cybersecurity

The establishment of these technologies would enable the realization of a low-cost automated driving system for general railway lines and highly automated driving with less ground equipment.

Here, we introduce a risk judgment method that utilizes a railway dynamic map as an example of the above-mentioned technology (2). The collection and sharing of various types of information that is required for operation decisions on each train, as well as risk judgment and decision to resume operation is needed in autonomous train operation. We are developing the railway dynamic map as a basis of information for risk judgment and decision to resume operation on the train. The railway dynamic map is managed hierarchically by mapping information detected by various abnormality detection systems onto a base map or track map. Each train searches for abnormalities on its running route in the railway dynamic map based on its current position (Fig. 4). We seek to achieve the avoidance of hazards during the running and automation of the decision to resume operation by implementing such a technology. Additionally, it is thought that the railway dynamic map can be used not only for autonomous train operations in the future but also as a deci-

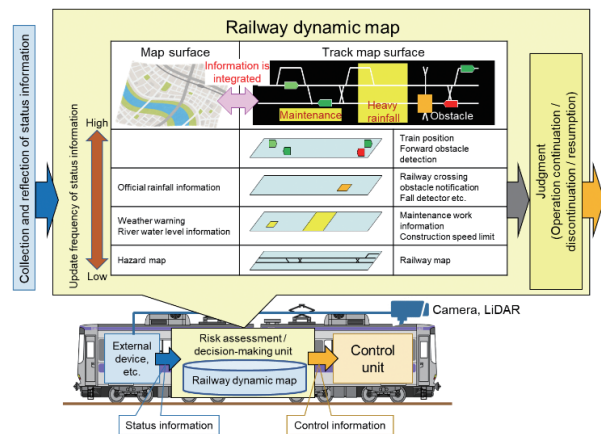


Fig. 4 Automation of risk and operation resumption judgment using railway dynamic map

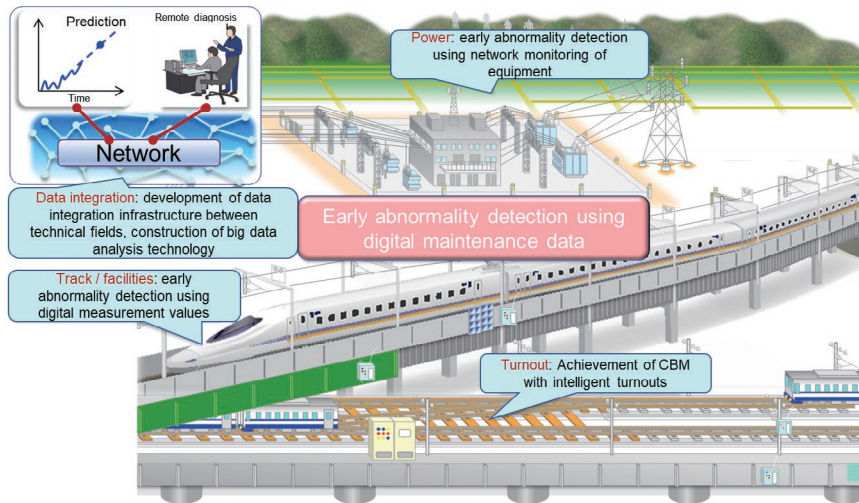


Fig. 5 Labor conservation by digital maintenance

sion-making support tool for current dispatchers.

2.2 Labor conservation by digital maintenance

During non-emergency periods, the progress of deformation is estimated by monitoring equipment from the vehicle, and repair plans are formulated based on inspections and diagnoses from these estimations. Meanwhile, in the event of an abnormality, the equipment abnormality is detected at an early stage, the spread of damage is prevented, the location of the occurrence is identified, and recovery support such as estimating the cause is provided. Such maintenance of railway equipment is called digital maintenance [3]. We are working on the following five developments in order to promote labor conservation through digital maintenance (Fig. 5).

- (1) Abnormality detection technologies for track structures using onboard measurements
- (2) Abnormality detection technologies for overhead contact wire equipment using onboard measurements
- (3) Abnormality detection technologies through network monitoring of power equipment
- (4) Control status monitoring technologies using intelligent turnouts
- (5) Centralized management of maintenance data using common data platform

We will promote research and development while setting “on-board measurements,” “networks,” and “automation of prediction and judgment” as the key technologies, and we aim to contribute to manpower-conserving, unmanned, and labor-conserving operations.

Here, we introduce the concept of (5) mentioned above. Sharing the maintenance data of equipment in each field requires centrally managing the maintenance data in a unified data format and location representation. To that end, we are conducting research and development of an “integrated analysis platform” [4]. This platform consists of a mirror server that stores a copy of the target data stored in the data server of each field in the original data format and location representation, unified-format data server that accumulates the data in a unified data format and location representation, and devices that have the function of converting data formats and location representations (Fig. 6). A general user requests processing such as data analysis from an application server through an interface device called a Web server. This prevents data modification or deletion due to erroneous operation and enables data analysis using various tools

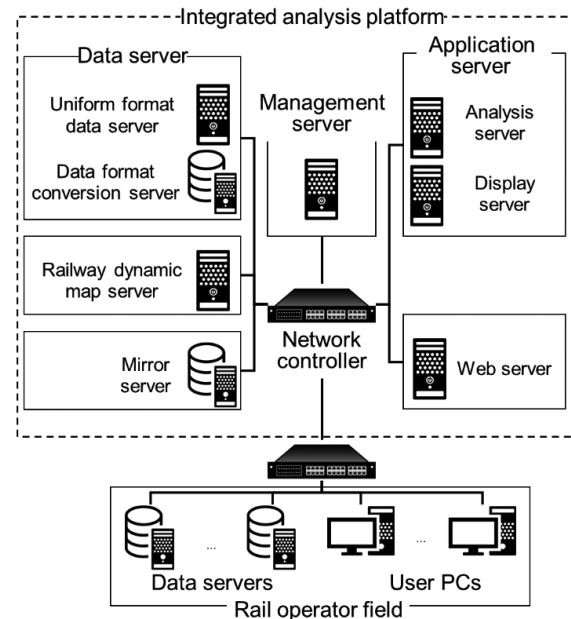


Fig. 6 Configuration of integrated analysis platform

on a high-performance application server, regardless of the user terminal performance.

3. Priority areas of research and development

3.1 Cost reduction through integration of railway-specific technologies and ICT

We are also conducting research and development with the aim of lowering the cost of railway operation with reduced equipment cost and labor conservation in maintenance by utilizing and integrating digital technologies with the specific technologies related to railway operation and safety control that we have accumulated to date.

As published in this volume, we are also prioritizing research and management of other aspects, such as a method for adding a fail-safe function, which is a railway-specific safety technology that is not considered in general-purpose cameras and image processing units; a

method for ensuring safety when applying inexpensive general-purpose computer boards to railway signaling systems [5]; and a method for predicting the lifespan of signal electronic equipment by sensing the usage environment in order to achieve condition based maintenance (CBM) as a labor-conserving measure for maintenance [6].

3.2 Development of practical system using cameras, etc.

We are not only engaged in research and development that focuses on data analysis, such as labor conservation through digital maintenance as mentioned above, but also on research and development of practical systems for monitoring and inspection using sensors such as cameras and LiDAR.

We have engaged in development such as that of a system that detects the blinking of an obstruction warning signal using the image of a camera in front of the train [7]; a system that uses cameras on the side of the vehicle in order to notify drivers of approaching people in real-time [8]; and a management support system for signaling equipment using handy camera images in front of the train [9]. Additionally, although still in the research stage, we are also working on a method to detect obstacles in front of trains through the fusion of sensors from a camera and LiDAR [10]. Through these developments, we aim to contribute to ensuring safety when manpower-conserving, unmanned, and labor-conserving operations are promoted.

3.3 Application of new public communication technologies to railway operation

Initiatives in which the Signalling and Operations Technology Division and Information and Communication Technology Division have collaborated include the application of new public communication technologies such as 5G to railway operations. Here, we introduce research and development on communications-based train control systems.

The communications-based train control system can reduce ground equipment such as track circuits, but it requires a transmission device to propagate control information. Additionally, the overall system does not necessarily reduce equipment depending on the line conditions, such as an increase in the functions of onboard equipment. Therefore, we have conducted research on the introduction procedure and security assurance for applying public communication technologies in order to further reduce the equipment needed [11].

4. Conclusion

The spread of COVID-19 has placed the railway business in a very difficult situation. However, we would like to continue contributing to the sustainable development of railways by actively utilizing digital technologies and quickly providing railway operators with research and development results that contribute to improving railway productivity, such as unmanned, manpower-conserving, and la-

bor-conserving operations. Collaboration with railway operators, universities, research institutes, and associated companies is essential for the innovation of railway systems through digital technologies, and we hope for your continued support and advice in our efforts.

References

- [1] Railway Technical Research Institute, News Release, "About reorganization," https://www.rtri.or.jp/press/vln4b30000000fem-att/220401_0001.pdf (Reference on 1st April, 2022) (in Japanese).
- [2] Kawasaki, K., "Trend on Research and Development Activities Relating to Signalling and Telecommunication Systems in Railway Fields," *Quarterly Report of RTRI*, Vol. 63, No. 3, pp. 155-158, 2022.
- [3] Railway Technical Research Institute, "Master Plan – Research and Development for Creating the Future of Railways – RESEARCH 2025(2020-2024)," https://www.rtri.or.jp/assets/edga9q00000003x7-att/RESEARCH2025RTRI_E.pdf, p. 9 (Reference on 1st April, 2022).
- [4] Ryuo, S., Kawamura, Y., Hada, A., Kurita, I., "Development of an Integrated Analysis Platform for Cross-sectional Railway Maintenance Data," *RTRI Report*, Vol. 36, No. 8, pp. 51-56, 2022 (in Japanese).
- [5] Gion, A., Ichikawa, T., Mukojima, H., Nagamine, N., Fukuda, M., Itagaki, T., "Configuration and Safety Confirmation Method of Image Processing System Applicable to Signalling Devices," *RTRI Report*, Vol. 36, No. 8, pp. 5-10, 2022 (in Japanese).
- [6] Fujita, H., Tsubaki, K., Takasaki, K., Oko, N., "Lifetime Estimation of Signalling Electronic Equipment Based on Sensing Information of Usage Environment," *RTRI Report*, Vol. 36, No. 8, pp. 37-44, 2022 (in Japanese).
- [7] Mukojima, H., Nagamine, N., Nomura, T., Ichikawa, T., "Blinking Detection for Obstruction Warning Signal using Front Camera," *Quarterly Report of RTRI*, Vol. 62, No. 2, pp. 118-123, 2021.
- [8] Goda, W., Nagamine, N., Mukojima, H., "Station Platform Safety Check Method for Driver Using Side Camera on Rolling Stock," *RTRI Report*, Vol. 35, No. 10, pp. 23-28, 2021 (in Japanese).
- [9] Mukojima, H., Nagamine, N., "Development of Signal Facilities Management Support System Using Camcorder Video on Train Cab," *RTRI Report*, Vol. 36, No. 8, pp. 45-50, 2022 (in Japanese).
- [10] Kageyama, R., Nagamine, N., Mukojima, H., "Train Frontal Obstacle Detection Method with Camera - LiDAR Fusion," *Quarterly Report of RTRI*, Vol. 63, No. 3, pp. 181-186, 2022.
- [11] Kitano, T., Gion, A., "Methods of Applying Public Communication Network to Communication-Based Train Control Systems," *Proc. of 58th Symposium on Railway Cybernetics*, 2021 (in Japanese).

Authors



Hideki ARAI, Ph.D.
Director, Head of Signalling and Operation Systems Technology Division
Research Areas: Signalling System, Safety, Lightning Protection



Mitsuyoshi FUKUDA
Director, Head of Information and Communication Technology Division
Research Areas: Signalling System, Safety Engineering

Recent Research on Railway-specific Dynamic Issues

Fumiaki UEHAN
Railway Dynamics Division

Railway system is composed of many sub-systems such as overhead contact lines, vehicles, tracks and structures, which interact with each other and show complex dynamic behaviors. We are working on the elucidation of and countermeasures for railway-specific phenomena caused by the interaction of sub-systems, such as damage due to natural disasters, train running safety, and deterioration of structures, using our own simulation and experiment/measurement technologies. This report introduces examples of recent research in the field of railway dynamics, related to improvement of resilience against natural disasters, digitalization of structure maintenance, hybridization of OCL/pantograph simulation, and weight reduction of train car bodies.

Key words: bridge seismic isolation, strong local wind, image measurement, onboard measurement, high-speed test facility for pantograph/OCL system, structural optimization

1. Introduction

A railway is a system composed of overhead contact wires, vehicles, tracks, civil engineering structures, and other components, each of which has a complex mechanism. As such, there is a strong need to clarify and develop measures against complex railway-specific phenomena such as damage caused by natural disasters caused by the interaction of these factors, ride comfort and running performance of trains, deterioration and damage to equipment, and noise and vibration. In this paper, we introduce research and development examples that approach railway-specific phenomena as dynamic problems using the Railway Technical Research Institute (RTRI)'s proprietary numerical simulation technology, as well as experimental, measurement, and evaluation technologies. First, we introduce the improvement of running safety by seismic isolation of bridge bearings and the clarification of vehicle behavior against strong local winds as an example of resilience against natural disasters; and structural vibration measurement using a video camera and deflection measurement method by onboard measurement as an example of digitalization of structure maintenance. Next, we sequentially introduce current collection system hybrid simulations using high-speed test facility for pantograph/OCL system and weight reduction of vehicle steel bodies by structural optimization, which is expected to contribute to decarbonization by improving transport energy efficiency as well as improving the performance of railway vehicles, as examples of research that makes comprehensive use of our proprietary experimental equipment and control/simulation technology.

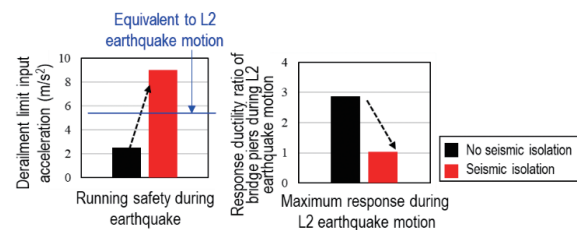
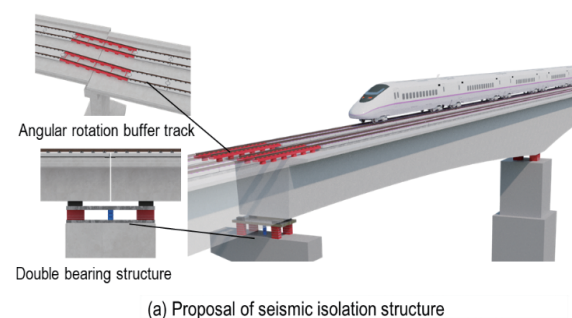
2. Resilience against natural disasters

2.1 Improved running safety by seismic isolation of bridge bearings

When seismic isolation bearings such as sliding bearings and laminated rubber bearings are applied to bridge bearings, the resulting longer period of structures and energy absorption of the seismic isolation bearings reduce damage to structures during large-scale earthquakes and improve recovery. However, these bearings undergo significant deformation in the direction perpendicular to the bridge axis, and there are concerns that running safety may decrease during an earthquake, so securing this safety is an issue. As a result,

seismic isolation bearings have not been actively adopted for railway bridges.

Consequently, we sought to improve recovery and running safety during earthquakes by making the bridge bearings seismically isolated by conducting a dynamic interaction analysis [1] of trains and structures during an earthquake. We used parameters such as the characteristics of structures and bearings, train speed, and type and scale of seismic motion in order to conduct a large number of analyses on tens of thousands of cases in order to find the conditions for simultaneously improving recovery and running safety during earthquakes through seismic isolation. Results showed that bridge piers had a natural period of at least 1.0 seconds, and the seismic isolation bearings were set so that the dominant period on the girders became at least 2.0 seconds in the event of a large-scale earthquake. This was shown to improve both recovery performance and running safety during an earthquake. Furthermore, in order to maximize the seismic isolation effect, we devised a structure that can suppress angular folding and joint stagger at the ends of bridges (Fig. 1(a)).



(b) Effect of seismic isolation (in case of pier natural period of 1.5 seconds)

Fig. 1 Improvement of running safety during earthquakes by seismic isolation of bearings

We showed that the application of these structures to a five-span continuous girder bridge (bridge length of 400 m) resulted in the trains not derailing even with L2 seismic motion, as shown in the analysis result in Fig. 1(b), thereby improving running safety; and that the pier response was reduced by 50% or higher, thereby reducing damage and improving recovery.

2.2 Effect of strong local winds on vehicle behavior

There has been increasing demand in recent years for the investigation of vehicle running safety against events that have not been considered to date, such as strong local winds influenced by surrounding buildings and structures such as building winds and effects of blinking tunnel sections on high-speed trains, as the awareness of strong wind disasters among railway operators has increased. Although these do not immediately threaten the running safety of vehicles, they are nevertheless important issues to achieve both running safety and transportation stability.

Therefore, we conducted a wind tunnel test using a 1:40 scale model and measured the wind speed distribution on the track and aerodynamic force acting on the vehicle under conditions affected by building wind (Fig. 2), investigating the rate and area where the wind speed increases and its effect on the aerodynamic force acting on the vehicle. Additionally, prior to the wind tunnel test, we used airflow analysis software to investigate the wind velocity field around the building (Fig. 3), and we used it to investigate the settings of the wind tunnel test conditions and verify the validity of the analysis results after the wind tunnel test.

As a result of these tests and analyses, we confirmed that the rate of increase in wind speed tends to increase the between buildings and around the outside of buildings, and that the results of wind field analysis using airflow analysis software were generally appropriate. However, we confirmed that there was a need to extend wind tunnel test conditions (e.g., building layout conditions, wind speed measurement range) and repeat the test, and that there is room for improvement in the accuracy of airflow analysis. In the future, we will work on these issues, where we plan to organize the relationship between building conditions (e.g., building size, layout) and wind speed fluctuations in order to be able to identify areas that require attention and where running safety reductions are expected, and to determine the appropriateness of the installation position of anemometers for driving restrictions.

3. Digitalization of structure maintenance

3.1 Structural vibration measurement using video camera

We developed a multi-point vibration measurement system for structures using a video camera [2] as a means of quantitatively inspecting railway structures based on objective numerical information (Fig. 4(a)). This system finds the magnitude and direction of displacement at any point in the image by treating surface patterns as a pattern of luminance information based on the digital image information of the object to be measured and by searching for the position between two images before and after moving. As an example, we show measurement results when a cable-stayed bridge (span 135m×2) with a running train was photographed from a position about 200 m away (Fig. 4(b)). The vibration behavior of the entire structure can be determined by computing the displacement vectors of many points on the bridge in real-time, and the maximum deflection was also measured with an error of about 5% against the nearby



Fig. 2 Wind tunnel test

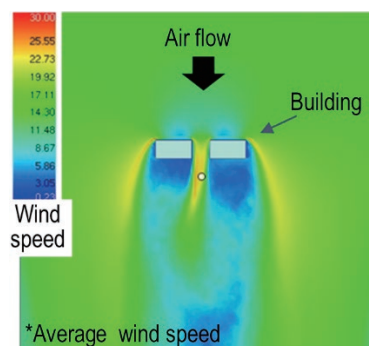
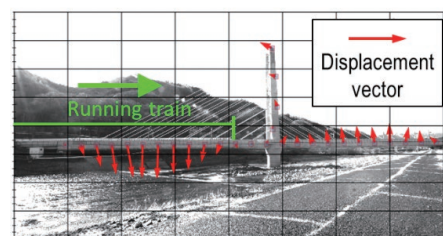


Fig. 3 Example of wind field evaluation result



(a) Measurement system



(b) Example of displacement measurement results for cable-stayed bridge

Fig. 4 Multi-point vibration measurement system using video camera

laser measurement result [3].

Next, we show an example of application to the inspection of bridge bearings. We targeted a steel bridge with a span of 8.5 m where the girder vibration was increased due to the deformation of the bearings, and attempted to detect deformation of the bearings using video photography. The vibration of the two bearings of the same shape on the same abutment was synchronously measured from a position about 15 m away from the bearing (Fig. 5(a)) when a train passed. Results showed that the occurrence of an abnormality in which the vertical displacement of the deformed bearing increased by approximately 0.2 mm (approximately twice as large) as that of the undeformed bearing (Fig. 5(b)).

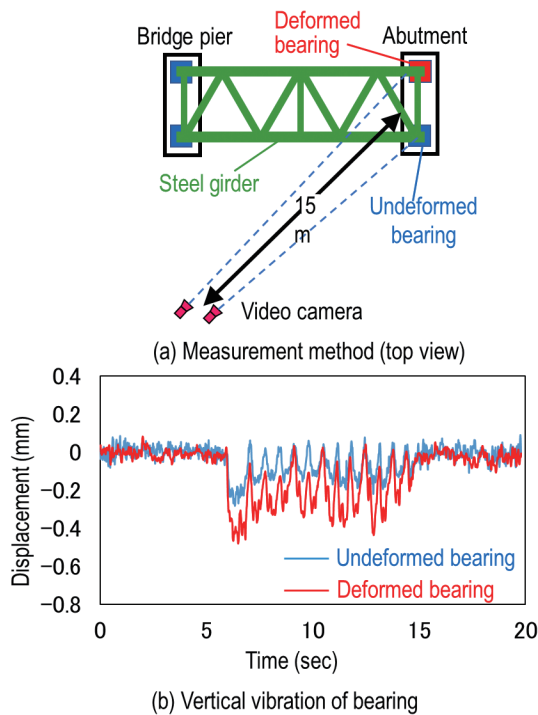


Fig. 5 Bearing deformation detection test results

We are currently studying effective image capturing methods according to the measurement object, and we are trying to expand the inspection object.

3.2 Deflection measurement method using onboard measurements

We have been developing a method to evaluate bridge deflection, which is a representative performance index of bridges, from track displacement that is obtained from running trains in order to further reduce costs and improve efficiency of maintenance of structures. Here, the maximum deflection of a bridge over which a train passed is estimated from the difference between track displacements measured at two locations of the head and tail cars of the running train. Theoretical examination clarified that the maximum difference in track displacement between the head and tail cars, shown in Fig. 6, is proportional to the maximum deflection of the bridge, and we proposed a unique estimation method using a conversion factor. Upon applying the track displacement measurement data of the head and tail cars obtained on the actual track, we confirmed that the proposed method could estimate the maximum deflection of the bridge with an error of about 10% (Fig. 7). However, this method has limitations such as the need for track displacement values at two locations, and the applicable range being train speeds of 100 km/h or less. Currently, we are expanding the method in order to utilize general track inspection cars and to extend the method to high-speed railways.

4. Current collection system hybrid simulation using a high-speed test facility for pantograph/OCL systems

We sought to conduct stationary performance evaluations of pantographs that considered the dynamic interaction between overhead wires and pantographs by developing a current collection system hybrid simulation (HS) using the high-speed test facility for panto-

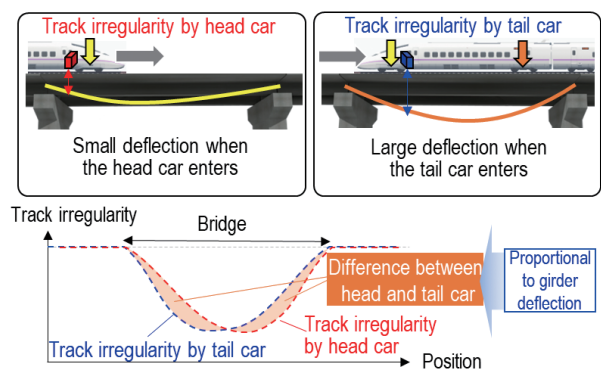


Fig. 6 Difference in track displacement when head car and tail car pass over bridge

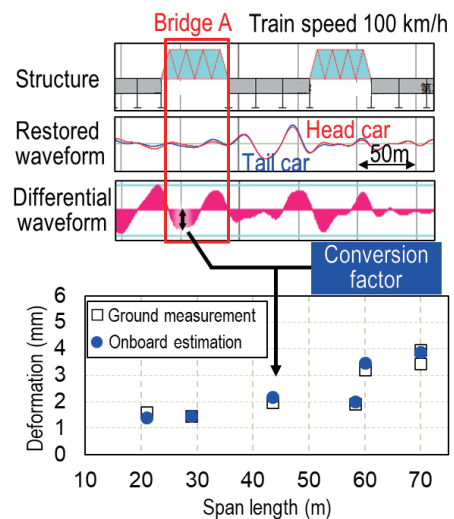


Fig. 7 Comparison between onboard estimated deflection and ground measured deflection

graph/OCL systems. The current collection system HS is an efficient technique that enables a stationary virtual running test of a pantograph by combining a pantograph vibration test and real-time simulation of overhead wire motion. In the past, RTRI developed a current collection system HS (henceforth, referred to as “high-frequency compatible HS”) that used a vibrator with relatively high frequency response characteristics (henceforth, referred to as “vibrator”) [4]. As shown in Fig. 8, in the current collection system HS, a vibrating device such as a vibrator applies a force (contact force) that vibrates the pantograph head in the vertical direction to the overhead wire model, the motion of the overhead wire model is calculated in real-time, and the vibrating device vibrates the hull using the obtained trolley wire displacement. The above-mentioned high-frequency compatible HS can reproduce the vibration of overhead wires up to 20 Hz. This frequency corresponds to the frequency at which the pantograph passes through the hanger at a train speed of 360 km/h (henceforth, referred to as “hanger period”), so the high-frequency compatible HS can reproduce the phenomenon caused by the hanger period. However, it was not able to express the sliding movement of overhead wires and pantographs and the deflection of overhead wires.

Meanwhile, at the RTRI, we successfully completed the large-scale test facility that is the high-speed test facility for pantograph/OCL systems in 2021[5]. As shown in Fig. 9, the high-speed test facility for pantograph/OCL systems can vibrate the rotating disk in the horizontal as well as vertical directions while the rotating disk is at-

tached to a trolley wire at the bottom and rotated at a maximum peripheral speed of 500 km/h. Furthermore, pantographs can be energized and the temperature and humidity in the test room can be changed, making it possible to conduct comprehensive pantograph tests.

Therefore, we newly developed a new collection system HS that used the high-speed test facility for pantograph/OCL system (henceforth, “general performance evaluation HS”) in order to resolve the issues of the high-frequency compatible HS [6]. Table 1 shows a performance comparison between the high frequency HS and general performance evaluation HS. The mass of the moving part of the vibrator is larger in the general performance evaluation HS than when compared to the high frequency HS, so the frequency range of overhead wire vibration that can be expressed is limited to up to 2 Hz, but the temperature rise of contact strips due to energization and the effects of environmental temperature and humidity as well as the effects of sliding movement due to running and the devi-

ation of overhead contact wires can be considered.

Figure 10 shows the results of the general performance evaluation HS test conducted at a running speed of 300 km/h. The upper row shows the overhead wire deviation, and the lower row shows the collector head vertical displacement, and the results of the general performance evaluation HS and overhead wire/pantograph system simulation are compared. Both results are in general agreement, so the general performance evaluation HS can be used to evaluate the amount of contact wire uplift at the supporting point when the pantograph passes.

5. Weight reduction of vehicle steel body through structural optimization

Recent railway vehicles are becoming increasingly sophisticated in various aspects such as running performance, convenience, and safety. At the same time, vehicle weight is increasing due to additional equipment and collision safety design, so there is a need to reduce the weight of the vehicle structure. Structural optimization is a weight reduction design method, but it is not yet common in the design of railway vehicles. Therefore, we sought to establish a weight reduction design method by structural optimization of railway vehicles. To that end, we developed a structural optimization method that can derive a manufacturable lightweight structure that expanded the functions of vehicle structures with frame structures so that the strength and rigidity can be ensured, and furthermore, so that constraints that are suitable for frame structures can be set.

Shape optimization and topology optimization are methods for finding a structure that satisfies given design requirements based on a certain prototype structure [7]. Shape optimization using the external shape as a design variable and topology optimization using the internal structure as a design variable are methods that conduct structural optimization by combining FEM analysis, sensitivity analysis, and optimization method. Many design variables can be set for these, so the degree of freedom of optimization is high, but given the convergence, appropriate optimization computation algorithms such as the optimality criteria method need to be applied. In the proposed method, the load transfer path is identified by topology optimization, and the initial shape for shape optimization is determined based on this. Next, a detailed evaluation is conducted by shape optimization in order to derive a final lightweight shape (Fig. 11). Additionally, since the optimized shape must be a manufacturable shape, it is possible to define conditions such as the condition that the cross-sectional shape be constant, the condition that there are no out-of-plane shape changes, and the condition that the mold can be removed by bending.

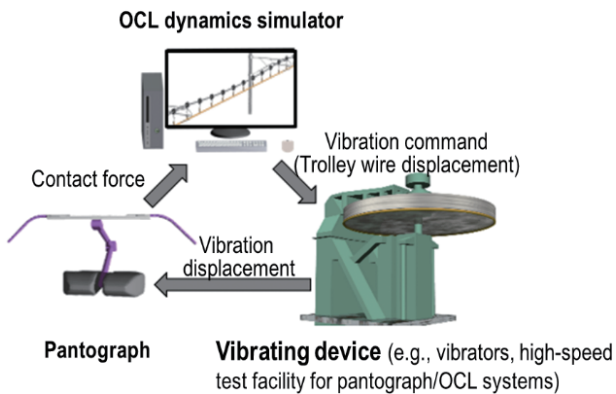


Fig. 8 Configuration of current collection system hybrid simulation

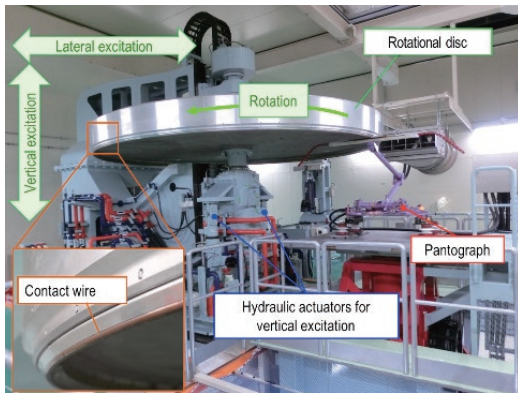


Fig. 9 High-speed test facility for pantograph/OCL system

Table 1 Comparison of functions between high-frequency compatible HS and general performance evaluation HS

	High frequency compatible HS	General performance evaluation HS
OCL Vibration	Up to ~20 Hz	Up to ~2 Hz
OCL stagger	Unavailable	Available
Slide with pantograph	Unavailable	Available
Electric current	Unavailable	Available
Environmental temperature control	Unavailable	Available
Humidity control	Unavailable	Available

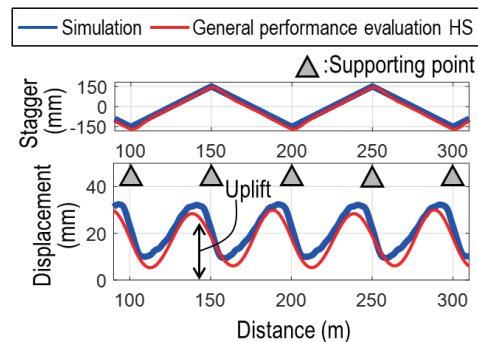


Fig. 10 Current collection system HS test results at running speed of 300 km/h

Structural optimization was conducted for a commuter vehicle, and a lightweight body structure was derived. The optimization conditions included objective function set as the mass of the design region, constraint condition set as the rigidity retention, maximum stress set as below the proof stress, and the constraint condition given so that the obtained shape can be manufactured. The load case involved application of the loads to each member obtained from the stress analysis of the entire vehicle simulating the structural load test. Structural optimization was conducted by setting the shape constraints for each member, and a lightweight shape was obtained. Figure 12 shows the main components. The side posts and rafters had a unique cross-sectional shape that had not been previously seen, but the shape restrictions resulted in structures that could be manufactured and practically used. In the existing vehicle, the lateral beam of the underframe generally has no openings and is reinforced with reinforcing materials, but the structural optimization results yielded a shape with many openings in the lateral side near the center in the longitudinal direction. The weight of the overall structure was reduced by approximately 7% by applying a lightweight structure to each member, such as the posts and belts (Fig. 13).

6. Conclusions

This paper introduced an overview of recent research related to

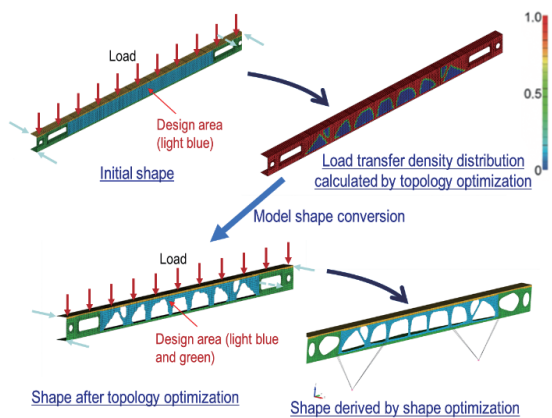


Fig. 11 Flowchart of structural optimization

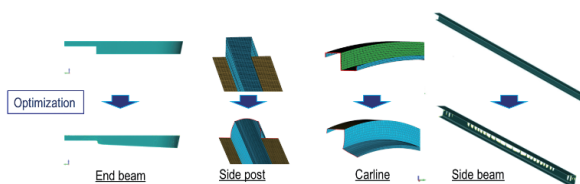


Fig. 12 Lightweight structure by structural optimization

Author



Fumiaki UEHAN, Ph.D.
 Director, Head of Railway Dynamics
 Division
 Research Areas: Structural Mechanics,
 Measurement Engineering

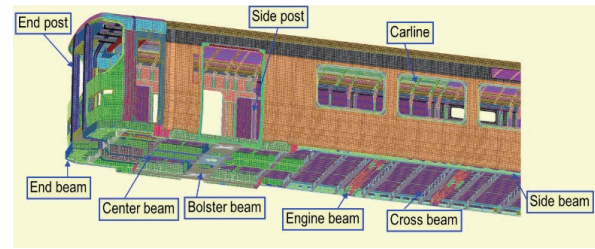


Fig. 13 Vehicle structure to which lightweight structure is applied

dynamic problems from railway-specific phenomena. These cases were approached as dynamic problems using RTRI's proprietary numerical simulation technology as well as experimental, measurement, and evaluation technologies, in an effort towards the safety of railways and the innovation of railway systems. Many of these are currently at the basic research stage, and we intend to apply them to actual problems in order to further verify the technologies and put them into practical use. Therefore, we hope for the continued guidance and cooperation of railway operators and other concerned parties. Part of the study presented in this paper was subsidized by the Ministry of Land, Infrastructure, Transport and Tourism.

References

- [1] Wakui, H., Matsumoto, N., Tanabe, M., "A Study on Dynamic Interaction Analysis for Railway Vehicles and Structures," *Quarterly Report of RTRI*, Vol. 35, No. 2, pp. 96-104, 1994.
- [2] Uehan, F., Ikeda, M., Matsuoka, K., "Development of Railway Bridge Inspection Method Using Video Camera and UAV," *RTRI REPORT*, Vol. 35, No. 9, pp. 41-46, 2021 (in Japanese).
- [3] Uehan, F., "Development of the U-Doppler Non-contact Vibration Measuring System for Diagnosis of Railway Structures," *Quarterly Report of RTRI*, Vol. 49, No. 3, pp. 178-183, 2008.
- [4] Kobayashi, S., Yamashita, Y., Usuda, T., Stoten, D. P., "Hybrid Simulation Testing of a Pantograph-Catenary System Using a Dynamically Substructured System Framework and a MDOF Catenary Model," *Quarterly Report of RTRI*, Vol. 61, No. 2, pp. 127-132, 2020.
- [5] Koyama, T., "Development of High-speed Test Facility for Pantograph/OCL Systems," *Quarterly Report of RTRI*, Vol. 63, No. 2, pp. 128-132, 2022.
- [6] Kobayashi, S., Koyama, T., Harada, S., "Hybrid Simulation Based on High-Speed Test Facility for Pantograph/OCL Systems," *RTRI REPORT*, Vol. 35, No. 12, pp. 47-52, 2021 (in Japanese).
- [7] Nishiwaki, S., Izui, K., Kikuchi, N., *Topology Optimization*, MARUZEN, pp. 1-17, 2013 (in Japanese).

Recent Studies on Railway Aerodynamics

Sanetoshi SAITO

Environmental Engineering Division

This paper presents an outline of recent studies on railway aerodynamics conducted in the Railway Technical Research Institute. Train aerodynamic effects increase significantly with the speed of trains, and cause various issues for railways. Since these issues closely affect train safety, convenience, and ride comfort, it is important to investigate these aerodynamic characteristics. Typical studies in this field, such as those on the effects of cross winds, aerodynamic devices of train vehicle and the effect of flow fields around trains in open sections and tunnels, are introduced in this paper.

Key words: aerodynamics, cross wind, aerodynamic brakes, snow accretion, ballast scattering, train draft, tunnel pressure fluctuation

1. Introduction

Railways involve a diverse range of aerodynamic phenomena which cause many problems that are not limited just to high-speed railways. Those relating to vehicles include overturning of vehicles due to strong wind, air resistance, vibration of the vehicle due to fluctuating aerodynamic force, pantograph lift force fluctuation, and snow accretion on the bogie. These are all important events that directly affect vehicle running stability and ride comfort. Meanwhile, running vehicles also incur various ground side effects. For example, phenomena that affect structures (e.g., sound barriers) and various facilities adjacent to tracks, maintenance workers, and passengers on platforms, such as pressure fluctuations, train drafts, and ballast scattering when trains pass. Additionally, problems such as aerodynamic sound and tunnel micro-pressure waves that affect the wayside environment can also be said to be caused by aerodynamic phenomena. Furthermore, thermal environment problems such as hot gas movement in tunnel fires and ventilation in main tunnels and underground stations are also affected by flows associated with running trains.

In this paper, of the railway aerodynamic phenomena that cause the above-mentioned problems we focus on and introduce recent research and development conducted by the Railway Technical Research Institute (RTRI) in the areas that follow. For vehicle related issues this paper concentrates on cross winds, snow accretion on bogies, and aerodynamic brakes among those relating to the vehicle; while for ground related issues this paper will cover ballast scattering, train draft, and tunnel pressure fluctuations.

2. Aerodynamic phenomena relating to vehicles

2.1 Vehicle aerodynamic characteristics against cross winds

Various measures such as the installation of wind fences, changes in vehicle specifications, and driving restrictions have been implemented in order to ensure the safety of vehicles during strong winds. The characteristics of strong winds, kinematic characteristics of vehicles, and the aerodynamic characteristics of vehicles against strong winds need to be understood in order to evaluate the effect of these measures. At RTRI, we conduct comprehensive research and development on each characteristic, and in this paper, we introduce examples of research and development on aerodynamic characteristics.

Wind tunnel tests and numerical simulations have been extensively performed to study the aerodynamic forces acting in strong winds. Wind tunnel tests involve the simulation of not only flat ground, but also ground structures such as bridges and embankments. Furthermore, a turbulent boundary layer that simulates the average wind speed and turbulence intensities of natural wind is used for the air flows that act on a model vehicle [1-4]. Recently, wind tunnel tests have been conducted on model vehicles that simulate several vehicle cross-sectional shapes in order to investigate the relationship between the aerodynamic force and cross-sectional shape of the vehicle. Furthermore, evaluations and studies have been conducted of the effects of ground structures and the effects of wind fences, such as with double-track viaducts with windbreak fences (Fig. 1).

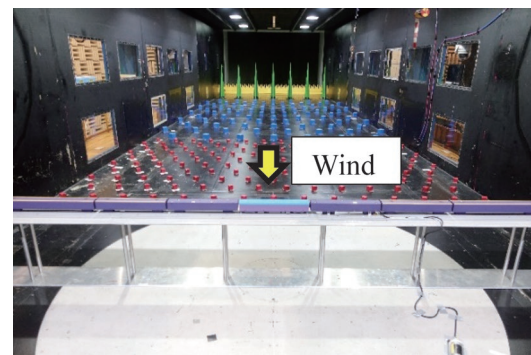


Fig. 1 Wind tunnel test for cross winds

We systematically investigated, using numerical simulations, the effects of ground structures and wind direction angles on the flow field that causes the generation of aerodynamic force acting on the vehicle by combining a vehicle with a simplified shape and ground structure and conducting computations under uniform flow conditions. Based on the results of these calculations, we clarified the factors that change the aerodynamic force due to ground structures from the viewpoint of the flow field [5].

2.2 Aerodynamic brakes

Ensuring safety performance is the most important issue in increasing the speed of the Shinkansen. One of the most important

items in this issue is the braking performance in an emergency, such as in an earthquake. Emergency braking methods include disc brakes which mechanically stop the rotation of the wheel by friction force in addition to an electric brake that is used for normal deceleration. Disc brake performance is not only limited because of the increase in the amount of heat absorbed as speed increases, but also by the adhesion force between wheels and rails, as is the case with electric brakes. Therefore, we are working on the development of an aerodynamic braking device for railway vehicles that increases the aerodynamic drag acting on the running vehicle in order to obtain a braking force (hereinafter referred to as “aerodynamic brake”), which will serve as a device to complement the braking performance in the high-speed range [6, 7].

The developed aerodynamic brake is a system in which thin and small aerodynamic brakes are distributed over the entire vehicle on the roof of the vehicle body in order to ensure both the interior space and passenger capacity and sufficient deceleration performance at high speeds (Fig. 2). The aerodynamic braking device uses the difference in aerodynamic force applied to a set of two resistance plates in order to operate with the running wind, and are a small, light-weight device with a thickness of 65 mm and mass of 36 kg (Fig. 2).

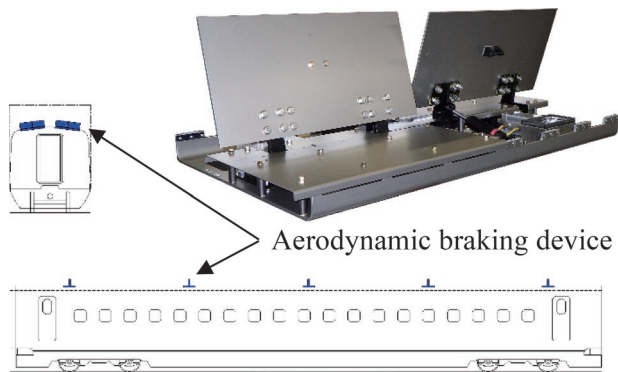


Fig. 2 Distributed-type aerodynamic braking device

We used wind tunnel tests with the manufactured prototype to confirm performance such as braking force and operating time, but also that the retracted state of the resistance plate did not adversely affect the wayside noise. Furthermore, we combined wind tunnel tests and numerical simulations in order to investigate the layout method when multiple units are mounted, where we showed that arranging them alternately in the left and right direction was effective. We also conducted various tests in order to verify the strength and durability of the device, resistance to low temperatures, scattering prevention performance when foreign objects such as birds collide with them, damage because of collected dirt and deterioration on each part of the device due to long-term outdoor use, and the effects of the heat cycle due to solar radiation; results confirmed that none of these issues presented a problem.

2.3 Measures against snow accretion on bogie

When a vehicle runs in a snowy area, the snow on the track rises up and adheres to the underfloor of the vehicle and bogie, accumulating there. When these snow clumps fall because of rising temperatures, running vibrations, or shocks when passing through turnouts, track ballast is scattered, and damage may occur to vehicles, equipment, and trackside houses. Furthermore, if the snow

clumps get caught in the gap between the rails of the turnout, this may prevent trains from changing track. Therefore, we are working on the development of measures to suppress snow accretion on the bogie using running wind. Specifically, we sought to suppress the amount of snow accumulating on the end cover plate of the bogie by investigating an aerodynamic device for controlling the flow inside the bogie through model experiments and numerical simulations [8, 9]. In order to reproduce snow accretion conditions, we developed an experimental device that runs a 1:11 scale model train (3.5-car train) at a maximum speed of 100 km/h and conducted experiments using walnut shell powder particles which have a motion similar to that of snow, as simulated snow in order to determine the conditions of snow accretion on the bogie and to determine the aerodynamic device specifications (Fig. 3).



Fig. 3 Vehicle model running experiment using artificial snow

3. Aerodynamic phenomena on ground

3.1 Ballast scattering

The ballast scattering phenomenon is a safety problem in a ballasted track of a high-speed railway. The main causes of this phenomenon are falling ice from vehicles during winter snowfall and train draft under the vehicle, as described in the previous section. Scattered ballast may reach not only the track but also the station platform and wayside, which is an important safety issue. Ballasted tracks such as with the Shinkansen include measures against scattering such as the installation of ballast screens or ballast nets to cover the ballast surface, and ballast fixation by spraying synthetic resin may sometimes be implemented [10].

There is a need when installing these scattering countermeasures to prevent the countermeasures themselves from being blown away by strong winds, such as train drafts and typhoons. Research using wind tunnels has been conducted for the evaluation of aerodynamic force for these countermeasures and ballast [11, 12]. However, elucidating the phenomenon by wind tunnel tests requires reproducing the situation in which the ballast and countermeasure samples are actually scattered. Therefore, we developed a wind tunnel test method that allows the scattering of objects using full-scale ballast and countermeasure samples (Fig. 4), and we conducted basic experiments in order to clarify the scattering phenomenon.

3.2 Train draft

When a train is running, the surrounding air is dragged by the train, which then generates wind (train draft). The train draft on a platform when a train passes is directly linked to passenger safety.

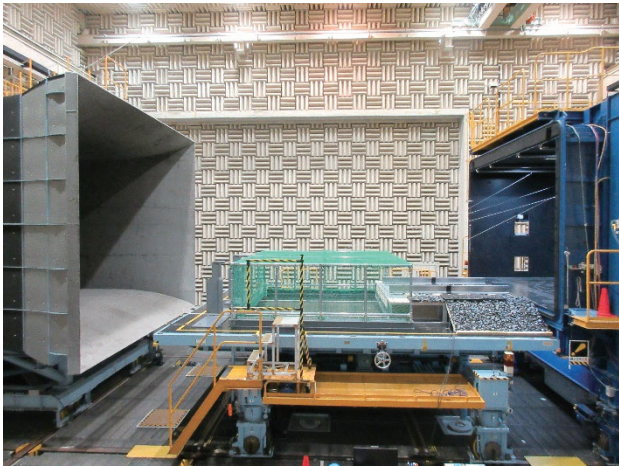


Fig. 4 Wind tunnel experiment where the scattering of objects is possible

Therefore, research has been conducted to understand the characteristics of train draft, mainly by measuring wind speed on Shinkansen platforms, in order to study dimensions of the refuge and safety fences on platforms [13, 14, 15]. Furthermore, the characteristics of the train draft generated in the closed space that is the tunnel are different from those in an open section, and there are influenced not only by the train passing but also by the pressure waves generated inside the tunnel. Train drafts in tunnels affect maintenance workers and facilities in tunnels, so they are a very important issue in terms of safety, as is the case with open sections. For train drafts in tunnels, on-site measurements [12, 13], research on prediction methods [16, 17], and research on the effects of workers [18] have been conducted.

The flow field around the train is very complex in both open sections and tunnel sections. In particular, the wake area immediately after the passing of the train tail car has a large impact on the fluctuating aerodynamic force that causes the train tail car to sway, and since the maximum value of the train draft also occurs in the wake position, clarifying this phenomenon is very important. Currently, we are conducting research on elucidating wake phenomena in high-speed trains through experiments using model launchers and numerical simulations, and we investigated the pressure distribution on the train surface and the basic characteristics of the train draft in open sections (Fig. 5).

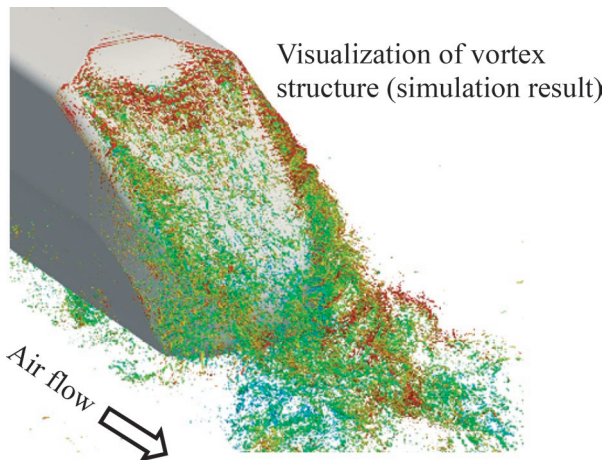


Fig. 5 Numerical simulation of flow around tail car

3.3 Tunnel pressure fluctuation

When the train nose enters and exits a tunnel, a compression wave (or expansion wave in the case of the tail) is formed in the tunnel. These compression and expansion waves propagate in the tunnel at almost the speed of sound, and they are reflected at the portal of the tunnel and the end of the train running in the tunnel. Therefore, multiple pressure waves travel back and forth in a tunnel when a train runs through it. Pressure rises when a compression wave passes and drops when an expansion wave passes. Therefore, pressure fluctuations act on the tunnel equipment and lining, as well as on running trains, and predicting the magnitude of these fluctuations is important for strength design of the tunnel equipment and vehicle structure. Similar to the prediction of train drafts in the tunnel as described in Section 3.2, research on prediction methods of tunnel pressure fluctuation has been conducted using numerical simulations [16, 17].

Currently, we study the strength of tunnel entrance hoods, which are structures that are associated with tunnels, and snow shelters that connect adjacent tunnels, by conducting research to evaluate the pressure fluctuations that act on both structures. There are examples of previous research on these issues [19, 20, 21], but in order to respond to the increased speed of Shinkansen trains in recent years, these studies aim to improve prediction accuracy by developing numerical simulations that consider the influence of the shape of the train head car and conducting model experiments to evaluate in detail the effects of openings in entrance hoods and slits in snow shelters (Fig. 6).

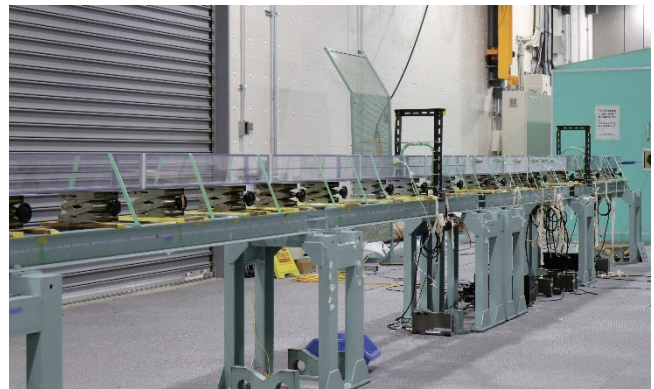


Fig. 6 Model experiment on snow shelter

4. Conclusions

There is a diverse range of aerodynamic phenomena in railways, of which only a part of research examples has been introduced in this paper. As train speeds rise, all these phenomena will become more prominent and will thus become increasingly important issues. Resolving these issues requires research which effectively combines model experiments, numerical simulations, and theoretical analyses. However, ultimately, on-site measures are extremely important. Furthermore, various considerations such as workability, cost, and whether or not there are adverse effects on others are needed for the practical application of countermeasures. In the future, we would like to proceed with research and development which can then be translated into practical application of effective countermeasure technologies while continuing discussions with all involved parties. As always, we hope for your continued support and cooperation.

References

- [1] Suzuki, M., Tanemoto, K. et al., "Method of Simulating the Atmospheric Boundary Layer in Wind Tunnel Tests on Aerodynamic Characteristics of Train/Vehicles under Cross Winds," *RTRI Report*, Vol. 17, No. 11, pp. 47-52, 2003 (in Japanese).
- [2] Tanemoto, K., Suzuki, M. et al., "Results of Wind Tunnel Tests for Aerodynamic Coefficients of Railway Vehicles," *RTRI Report*, Vol. 27, No. 1, pp. 47-50, 2013 (in Japanese).
- [3] Otobe, T., Tatematsu, T. et al., "Evaluation of the Aerodynamic Force on a Railway Vehicle in Half-bank Half-cut Line Sections," *RTRI Report*, Vol. 32, No. 11, pp. 5-10, 2018 (in Japanese).
- [4] Otobe, T., Suzuki, M. et al., "Wind Protection Effect by the Wall for a Vehicle with Strong Wind," *RTRI Report*, Vol. 31, No. 9, pp. 5-10, 2017 (in Japanese).
- [5] Noguchi, U., Suzuki, M., and Kikuchi, K., "Large-eddy Simulation on the Aerodynamics of Simplified Train under Crosswind," *RTRI Report*, Vol. 35, No. 6, pp. 29-34, 2021 (in Japanese).
- [6] Takami, H., "Development of Aerodynamic Brake for High-speed Railway," *RTRI Report*, Vol. 34, No. 3, pp. 5-10, 2020 (in Japanese).
- [7] Takami, H., "Development of Small-Sized Aerodynamic Brake for High-Speed Railway," *Transactions of the JSME (B)*, Vol. 79, No. 803, pp. 1254-1263, 2013 (in Japanese).
- [8] Murotani, K., Nakade, K., and Kamata, Y., "Development of Simulator to Accurately Reproduce Snow Accretion Phenomenon for Railway Vehicles Traveling in Snowy Areas," *RTRI Report*, Vol. 36, No. 7, pp. 59-68, 2022 (in Japanese).
- [9] Takami, H., Araki, Y. et al., "Countermeasures against Snow Accretion Around Shinkansen Bogies Using Running Wind," *RTRI Report*, Vol. 36, No. 9, pp. 5-10, 2022 (in Japanese).
- [10] Yoshida, M., Uchida, M. et al., "Countermeasures for Ballast-Flying Phenomena Caused by High-Speed Trains," *RTRI Report*, Vol. 6, No. 6, pp. 27-36, 1992 (in Japanese).
- [11] Nakano, T., Sakuma, Y., and Inoue, T., "Risk assessment of flying of rubber screens installed on railway ballast," *STECH2021*, 2021.
- [12] Nakano, T., Sakuma, Y. et al., "Assessing Aerodynamic Force of Flat Plate Object Installed on Railway Track by Wind Tunnel Test," *RTRI Report*, Vol. 35, No. 6, pp. 35-40, 2021 (in Japanese).
- [13] Tsuchiya, J. and Hirota, K., "Field Tests of Train Draft," *Railway Technical Research Pre-report*, No. 81-68, 1981 (in Japanese).
- [14] Horie, A. and Sugiyama, T., "Field Tests of Train Draft on Tohoku Shinkansen," *Railway Technical Research Pre-report*, No. A-86-155, 1986 (in Japanese).
- [15] Tanemoto, K. and Kajiyama, H., "Train Draft and Pressure Variation on a Platform," *RTRI Report*, Vol. 17, No. 11, pp. 53-56, 2003 (in Japanese).
- [16] Yamamoto, A., "Pressure Variation, Aerodynamic Drag and Tunnel Ventilation in Shin-Kan-Sen type Tunnel," *Railway Technical Research Report*, No. 871, 1973 (in Japanese).
- [17] Kajiyama, H., Iida, M., and Maeda, T., "Numerical Calculation of Air Flow in Underground Railway," *RTRI Report*, Vol. 7, No. 7, pp. 51-58, 1993 (in Japanese).
- [18] Endo, H., Omino, K. et al., "Estimation of the Effects of Train Draft on Maintenance Workers," *RTRI Report*, Vol. 23, No. 9, pp. 29-34, 2009 (in Japanese).
- [19] Ozawa, S. and Maeda, T., "Tunnel Entrance Hood at the Southern Portal of Fukushima Tunnel on Tohoku Shinkansen," *Railway Technical Research Pre-report*, No. A-87-52, 1987 (in Japanese).
- [20] Fukuda, T., Saito, S. et al., "Micro-pressure wave emitted from slits of a shelter linking neighboring tunnels," *Fluid Engineering Conference*, 1117, 2013 (in Japanese).
- [21] Fukuda, T., Saito, S. et al., "Countermeasure against the micro-pressure wave by a shelter linking neighboring tunnels," *Proceedings of the 15th International Symposium on Aerodynamics, Ventilation & Fire in Tunnels*, pp. 539-552, 2013.

Author



Sanetoshi SAITO, Ph.D.
Director, Head of Environmental Engineering
Division
Research Areas: Aerodynamic, Tunnel Fire
Dynamics

Configuration and Safety Confirmation Method of Image Processing System Applicable to Signalling Systems

Akihiro GION

Telecommunications and Networking Laboratory, Information and Communication Technology Division

Takeshi ICHIKAWA

Hiroki MUKOJIMA

Image Analysis Laboratory, Information and Communication Technology Division (Former)

Nozomi NAGAMINE

Image Analysis Laboratory, Information and Communication Technology Division

Mitsuyoshi FUKUDA

Information and Communication Technology Division

Tomonori ITAGAKI

Kyosan Electric Mfg. Co., Ltd

In recent years, image processing has been applied to the visual inspection of rolling stock and railroad tracks. It is also expected to be used for detecting abnormal situations on level crossings and platforms, however safety assurance is an issue for signal security applications. This paper reports on a method for composing an image processing system using general-purpose processing equipment that can be applied to signalling equipment and a method for confirming safety.

Key words: camera, image processing, safety, abnormality detection

1. Introduction

Recently there have been advances in the performance of image processing, image sensors with higher resolution and affordable single-board computers. As a result, advanced image processing algorithms have become available at relatively low cost, and are used in various fields. In railways, the use of image sensors for visual inspections of rolling stocks and tracks is also being promoted [1]. As level crossing collisions and platform accidents account for more than half of all railway operating accidents, the image processing-based obstacle detection applications are expected, but safety assurance is required when applied to safety-related use. Therefore, the authors have developed an image processing-based obstacle detection system applicable to safety-related systems. This paper reports on the developed configuration method of the image processing system and the safety verification method.

2. Overview of image processing systems and its issues

2.1 Overview of image processing systems

Generally, “image processing systems” are systems that process image data captured by an image sensor such as a camera, and record or determine changes or features of objects extracted from the image data. In this paper, however, the term “image processing system” is defined as a system including a control unit that outputs control signals based on the image processing unit. Figure 1 shows the configuration of the system discussed in this paper.

2.2 Overview of image processing systems

Safety-related systems are based on the fail-safe concept of

shifting to the safe side in the event of device failures or abnormalities. For example, signalling equipment, such as electronic interlockings, ensure safety against device failures by using special-purpose control hardware called fail-safe units (FS unit) in their processing. Figure 2 shows the light barriers-based obstacle detection equipment [2], which is an example of an obstacle detection application. As shown in the figure, this equipment consists of a light-emitting unit (LEU), a light-receiving unit (LRU), and a processing unit (PU). The PU checks whether the LRU is receiving light according to the verification pattern, and feedback control is conducted. The system detects failures of the LEU or LRU, blockages caused by obstructions, and reduced light intensity due to fog, etc., as diagnostic mismatches, to ensure safety.

The image processing system differs from conventional signalling systems in sensing and image processing configurations. For sensing, only a camera, which corresponds to the LRU part, is used, and the problem is that a closed loop cannot be configured. The computing performance of existing FS unit is insufficient for image

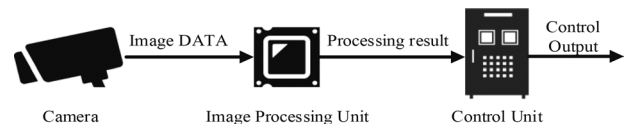


Fig. 1 Configuration of image processing systems

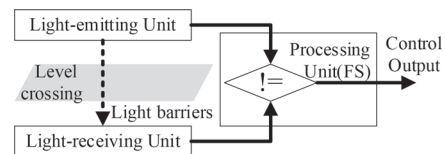


Fig. 2 Configuration of light barriers-based obstacle detection equipment

processing, and the challenge is to archive fault detection and safety control with general-purpose processor-based configurations.

3. Safety analysis of image processing systems

A safety analysis was conducted on an image processing system for the purpose of detecting anomalies on railway tracks. The system under consideration here is the one shown in Fig. 1, in which the image processing is for detecting anomalies on railway tracks, and the control output is the abnormal detection output. The analysis was conducted using the approach of defining the system with specific assumptions, extracting risks, and then generalizing the system.

3.1 Assumptions and safety analysis for image processing systems

3.1.1 Assumptions

This section describes the assumptions for each element regarding the components of the system.

(1) Camera

An infrared camera (Vision Sensing:VIM-640) is assumed to be used, and its structure is shown in Fig. 3.

(2) Image processing unit

A high-performance general-purpose processor (Intel Core i7 6600U) is used to process images at 10 frames per second (100 ms).

(3) Control unit

FS unit is used to inspect camera and image processing unit failures and ensure the safety of control output.

(4) Communication path

The communication path between the camera and the image processing unit is Ethernet, and GigE Vision, a protocol for trans-

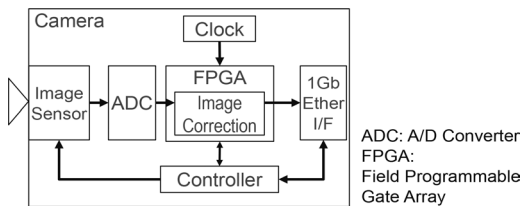


Fig. 3 Internal configuration of an infrared camera

mitting the captured images and controlling the camera, is used. The interface between the image processing unit and the control unit shall be that of the FS unit.

(5) Others

The detection performance of the algorithm shall be considered separately from the safety analysis, and the study shall exclude the detection of the hazardous side due to defects in the algorithm, environmental conditions, etc.

3.1.2 Fault Tree Analysis / Failure Mode and Effects Analysis

Fault Tree Analysis (FTA) and Failure Mode and Effects Analysis (FMEA) were performed on the image processing system described in the previous section. The excerpts from the FTA are shown in Fig. 4, and some of the FMEA results for the elements in Fig. 1 and 3 are shown in Table 1. The top event among the hazardous events in the image processing system was defined as ‘the control unit does not provide a control output in a failure’.

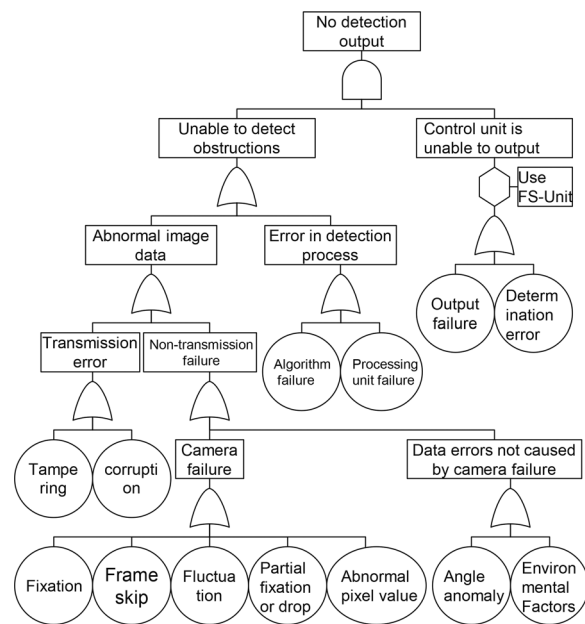


Fig. 4 FTA for imaging systems (excerpt)

Table 1 Example of FMEA for imaging systems (excerpt)

Device/Element	Function block	Failure mode	Effect	Description	
Camera	Image sensor	Sensor burnout	(1) Abnormal pixel value	Whiteout, contrast decrease, etc.	
	ADC	Fixed output failure	(2) Image fixation	Image data becomes the same data in every frame.	
	FPGA	Clock generation	Clock stop	(2) Image fixation	Image data becomes the same data in every frame.
			Clock fluctuation	(3) Frame skipping	Time interval of captured data is not enough.
			(4) Frame rate error	Timing of captured image data is out of sync.	
	Correction processing	Correction Error	(1) Abnormal pixel value	Whiteout, contrast decrease, etc.	
			(5) Partial fixation or drop	Part of image data is missing or identical every frame.	
Communication path		Noise induction	(6) Data alteration	Corruption of image data.	
		Cable breakage	(7) Missing data	Missing data in transmission in units of image data.	
Image processing unit	Image processing	Image processing	(8) Detection error	Detection processing is incorrect.	

3.2 Summary of extracted events

The events extracted by FTA/FMEA were summarized for the camera, image processing unit, control unit and communication path, respectively.

3.2.1 Camera

The following events are assumed to occur due to internal camera failures or environmental factors: (1) abnormal pixel values, (2) image fixation, (3) frame skipping, (4) frame rate error, and (5) partial image missing or sticking. Feedback diagnosis such as that of existing obstacle detection systems is difficult to be applied to cameras, so that comparison of multiple cameras cannot be directly matched due to the difference in angle of view. Therefore, when the camera is a single configuration, a method for detecting camera failures by other equipment is required.

3.2.2 Image processing unit

An event of (8) detection error due to a failure of the general-purpose image processing unit or an algorithmic problem is assumed. In existing FS units for signalling systems, there is a configuration in which a general-purpose processor is duplicated and the results of synchronous processing are compared and verified. However, since the image processing unit operates asynchronously and there are fluctuations in pixel value updates due to the use of probability statistics, the obstacle determination is not the same. Therefore, the application to image processing requires a verification method that supports asynchronous operation.

3.2.3 Control unit

Since the control unit uses a FS unit, there are no hazardous events that can occur in the control unit itself. However, there must be no omissions in the method for inspecting failures in the camera and the image processing unit and it must be feasible in the FS unit.

3.2.4 Communication path

On the communication path, (6) data alteration and (7) missing data are assumed to occur. In Ethernet, CRC32 verification is performed, but the control unit cannot ascertain the correctness of the verification.

4. Proposal configuration method

This chapter proposes a method for configuring an image processing system to deal with the hazardous events and issues identified in the safety analysis in Chapter 3.

4.1 System configuration

The proposed image processing system consists of a single camera, an image processing unit with a duplex general-purpose processing hardware, and a control unit with an FS unit. The control unit provides control output based on the obstacle determination of the image processing unit. The control unit also inspects the camera and the image processing unit and provides control output when a failure is detected to ensure safety of the image processing system.

4.2 Safety verification method

The safety verification method of the proposed image processing systems consists of verification of diagnostic data embedded in image data, verification of test patterns, and verification of digest data.

4.2.1 Diagnostic data

Diagnostic data, which consists of frame counts, clock counts and image CRC, is embedded in the image data as shown in Fig. 5. From the Ethernet bit error rate of 10^{-10} and the image data length of 4,915,200 bits, the probability of more than one error being included is 1.21×10^{-7} . The hourly probability of n consecutive CRC matches is $2,250 \times 2^{4-m} \times n[h]$ for a CRC bit length m . From this, in consideration of transmission errors and fixed misrecognition, the bit length of the image CRC $m = 16$ and the number of times $n = 3$ until the determination of an image fixation.

(1) Image CRC

The image CRC is the CRC16 values of the $N(0,0)$ to $N(636,479)$ pixel values of the image data and is calculated by the camera FPGA. As shown in Fig. 6, the values are recalculated by the image processing unit and the control unit confirms that the values in the diagnostic data and the recalculated values match.

(2) Frame count and clock count

The frame sequence number, which is counted internally in the camera, is stored as the frame count, and the interval before and after the frame is stored as the clock count. As shown in Fig. 7, the frame count is added in the image processing unit and the control unit performs verification in consideration of missing data.

4.2.2 Test pattern

To diagnose the correctness of the CRC calculation of the camera and image processing unit, test image data is prepared in the camera as a test pattern and inserted as image data at regular intervals or whenever requested by the control unit. The image processing unit recalculates CRC values in the same way as an image data, and the control unit verifies them against the correct CRC values of the test pattern.

4.2.3 Digest data

As a method for diagnosing the health of image processing units that operate asynchronously, the Hamming distance between digest data of detection results is evaluated. First, as shown in Fig. 8(a), after being divided by block size K for the binarized detection results with/without detection in pixel units by image process-

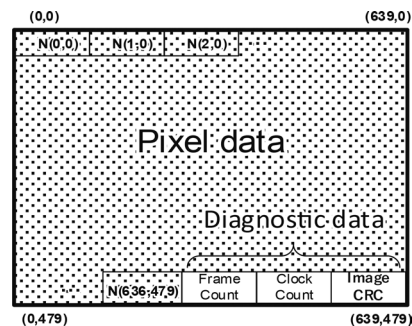


Fig. 5 Storing diagnostic data in image data

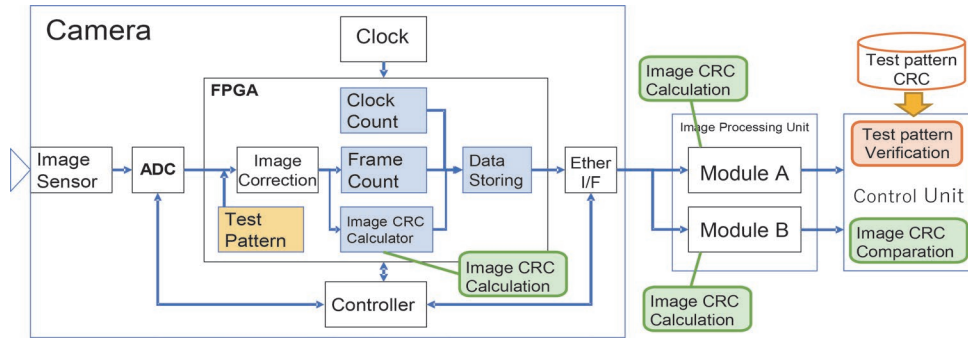


Fig. 6 Image processing system configuration and verification process with image CRC

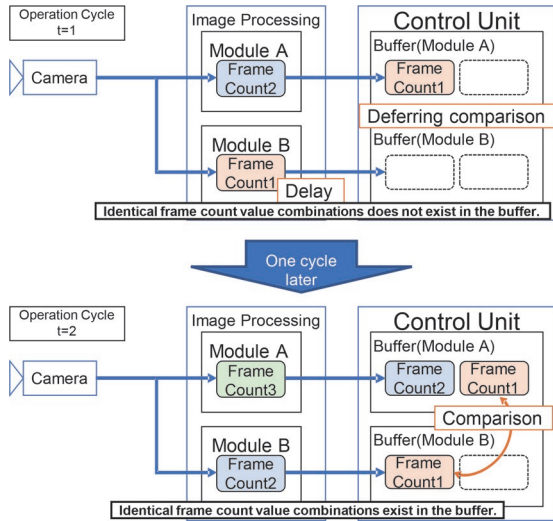


Fig. 7 Verification of count values in delay/drop

ing, the detection results are digested by calculating the presence or absence of detection within each block. Then, they are serialized in raster scan order as shown in Fig. 8(b). The Hamming distance is then calculated for the A/B system data as shown in Fig. 8(c), and both systems are determined to be healthy when it is below a predetermined threshold value.

4.3 Safety assurance

Safety assurance methods for the identified camera system failure modes are shown below.

4.3.1 Abnormal pixel value

Abnormalities in pixel values are detected by calculating image qualities such as white level and contrast in the image processing algorithm of the image processing unit. On the other hand, a failure of the image processing unit is detected by comparison the output of the A with B systems of the FS-CPU in the control unit. The image processing unit detects abnormal pixel values, and the control unit detects inter-system mismatches to ensure safety.

4.3.2 Image fixation

Image fixation can be determined by monitoring the fluctuations of the image CRC in the diagnostic data by the FS-CPU in the control unit and detecting that the value is unchanged. Normally,

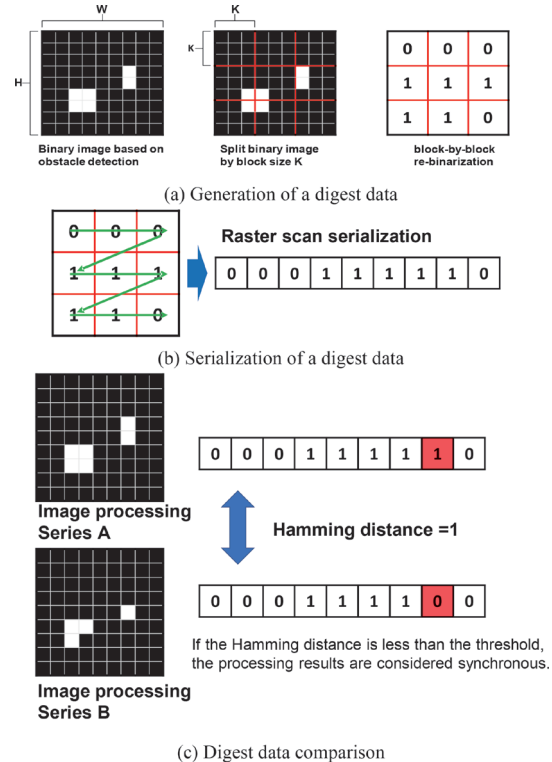


Fig. 8 Digest data generation and comparison

even when a stationary object is imaged, minute fluctuations occur in the pixel values pixel by pixel due to random noise generated in the image sensor. Therefore, the image CRC is expected to change every frame. The probability of three consecutive events with the same CRC in different images is $1.27 \times 10^{-10}/[h]$, which is sufficiently low to have a small impact on the detection delay since 10 frames are acquired every second.

4.3.3 Frame skipping

Frame skipping can be determined by monitoring the increment of the frame count in the diagnostic data by the FS-CPU of the control unit.

4.3.4 Frame rate error

A frame rate error can be determined by monitoring the clock count value in the diagnostic data and the cycle counter value assigned by the image processing unit in the FS-CPU of the control

unit. As a frame rate error is an event where the frame interval deviates from 100 ms, the health of both the frame rate and the time-keeping function can be monitored by checking the timekeeping of the camera and the image processing unit respectively, as shown in Fig. 7.

4.3.5 Partial fixation or drop

Partial fixation or drop of images are assumed to be failures in the area of the camera where the correction process is carried out. Since the soundness of the self-diagnosis by the camera cannot be guaranteed, a test pattern and image CRC are used as a method for external diagnosis by the FS-CPU of the control unit. The test pattern is inserted into the correction process of the camera and the camera and image processing unit calculate the image CRC respectively. If a part of the image is missing or stuck, the test pattern is destroyed and an image CRC different from the correct data is given. Hence, the control unit can detect a missing or stuck image because the control unit can compare it with the correct data.

4.3.6 Data alteration

Data alteration is detected by the FS-CPU of the control unit monitoring the image CRCs. The FS-CPU monitors the match between the image CRC assigned by the camera and recalculated by the A and B systems of the image processing unit. It also monitors the health of the image CRC generation functions of both the camera and the image processor by checking the image CRC of test patterns inserted periodically.

4.3.7 Missing data

Missing data is an event similar to frame skipping, but in this paper, it refers to a mismatch in the reception state between the A and B systems. The FS-CPU is configured to retain two cycles of output from each system of the image processing unit, search for data with the same frame count among them and compare and check them to ensure availability against missing data. This ensures availability against missing data.

4.3.8 Detection error

A detection error is an event in which an obstacle is not detected due to a fault in the image processing unit. However, the FS-CPU of the control unit can determine the fault by testing the Hamming distance of the digest data generated by the image processing unit A/B systems. Latent faults cannot be detected simply by comparing the presence or absence of an abnormality as a detection result. However, the digest of the processing data makes it possible to monitor that the input to each system and the learning are approximately the same, so that latent faults can be detected.

4.4 Key advantages of the proposal method

The advantages of the proposed image processing system configuration and safety verification method are twofold. The first is that existing FS units can be applied as a means of ensuring safety. Image processing has been difficult to incorporate into FS units because of the large amount of processing and the huge amount of information handled. However, in the proposed method, the role of the FS unit specializes in fault detection and safety control of general-purpose sensors and processing devices to separate processing

and verification, making it possible to apply the system. The monitoring methods include matching the outputs of general-purpose units, comparing them with correct data or calculating the Hamming distance, etc. The data size can be compressed to CRCs and digest data to enable comparison and matching on the FS-CPU.

Another advantage is the ability to compare and match processes that are asynchronous and have different internal states. Fluctuations caused by the use of probability statistics in image processing algorithms and differences in transmission states make it possible to match processes where the image processing units are not strictly identical. This method can be applied to more advanced image processing algorithms and is expected to improve availability, as it enables the detection and separation of abnormal systems through redundancy of triple systems or more.

5. Prototyping and evaluation

A prototype level crossing abnormality detection device applying the proposed countermeasures was built and tested to evaluate the safety technology. The configuration of the level crossing abnormality detection device is shown in Fig. 9.

By combining image processing using a general-purpose device with diagnosis and control by the FS unit, it was confirmed that image processing in 100 msec cycles could be diagnosed. In addition, in-factory tests were carried out to confirm that the fail-safe control unit can detect and safely control abnormalities and failures when the extracted failure modes are generated in the prototype equipment for the failure diagnosis function. The test items, test methods and test results are shown in Table 2. For each of the test items (1) to (6), it was confirmed that there were no safety problems with regard to failures or abnormalities in each unit, since the fail-

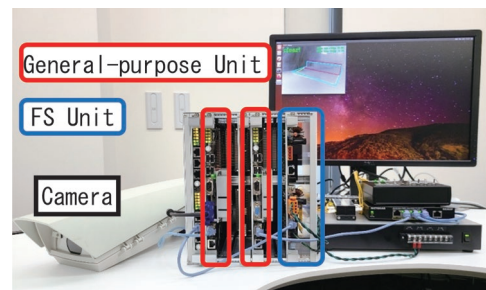


Fig. 9 Configuration of the prototype

Table 2 Test cases, methods and results

Test case	Test method	Result
(1) Image CRC	Modified CRC value	Good
(2) Clock count	Set an anomaly count value (single)	Good
	Set an anomaly count value (both)	Good
(3) Test pattern	Modified CRC value	Good
	No transition to normal image	Good
	No test pattern insertion	Good
(4) Digest data	Detects deviations in Hamming distance	Good
(5) Alternating signal	Alternating stop by camera	Good
	Alternating stop by image processing unit	Good
(6) Others	Unplug the Ethernet cable.	Good
	Stop one system from operating	Good

ures and the abnormalities could be detected and fixed on the safe side as intended.

6. Conclusion

In order to introduce an image processing-based determination system into a safety-related application, the system was defined as a generalized functional block, and the hazardous events of the system were extracted and the issues were organized through safety analysis. As countermeasure methods for the identified hazardous issues, proposals were made to add and verify diagnostic data to image data, soundness checking of image CRC using test patterns, and soundness checking of image processing using digest data. A prototype system for verification of an image processing-based level crossing obstacle detection system was built and tested. Failure tests

were conducted and it was confirmed that there were no safety problems.

Since a configuration method for applying the image processing-based system to signalling applications has been established, we will promote the practical application of a system for monitoring abnormalities on railroad tracks based on the configuration method and diagnostic method of the prototype system.

References

- [1] Anami, T., "Status of initiatives for Smart-maintenance," *JR EAST Technical Review*, No. 39, pp. 5-10, 2021.
- [2] Suzuki, I., "Various types of Level crossing obstacle detection equipment," *Railway & electrical engineering*, Vol. 2, No. 9, pp. 23-28, 1991 (in Japanese).

Authors



Akihiro GION
Senior Researcher, Telecommunications and Networking Laboratory, Information and Communication Technology Division
Research Areas: Signalling Systems



Nozomi NAGAMINE, Ph.D.
Laboratory Head, Image Analysis Laboratory, Information and Communication Technology Division
Research Areas: Computer Vision, Image Processing, Signalling Systems



Takeshi ICHIKAWA
Assistant Senior Researcher, Image Analysis Laboratory, Information and Communication Technology Division (Former)
Research Areas: Signalling Systems



Mitsuyoshi FUKUDA
Director, Head of Information and Communication Technology Division
Research Areas: Signalling System, Safety Engineering



Hiroki MUKOJIMA
Researcher, Image Analysis Laboratory, Information and Communication Technology Division (Former)
Research Areas: Computer Vision, Image Processing



Tomonori ITAGAKI
Manager, Kyosan Electric Mfg. Co., Ltd
Research Areas: Signalling Systems

Lifetime Estimation of Electronic Signalling Equipment Based on Sensing Data from Usage Environment

Hiroyuki FUJITA

Signalling Systems Laboratory, Signalling and Operation Systems Technology Division

Kentaro TSUBAKI

Signalling Systems Laboratory, Signalling and Operation Systems Technology Division (Former)

Ken TAKASAKI

Signalling Systems Laboratory, Signalling and Operation Systems Technology Division

Naoyuki OKO

Signalling Systems Laboratory, Signalling and Operation Systems Technology Division (Former)

In recent years, technological development to shift from conventional time-based maintenance (TBM) to condition-based maintenance (CBM) has been progressing. In response to this trend, various efforts are being made for signalling equipment along railway tracks. However, there are issues to be solved when applying CBM to electronic signalling equipment of which indications of deterioration is difficult to be detected. Focusing on the environment in which electronic signalling equipment is installed, this paper describes the results of examining new methods for lifetime estimation of equipment based on sensing data from the usage environment.

Key words: *lifetime, electronic signalling equipment, usage environment, CBM, acceleration test, temperature*

1. Introduction

Railway signalling systems have been widely installed along railway lines to ensure safe and stable train operation. Recent years have seen the introduction of electronic devices in railway signalling systems, to replace relays, in order to reduce the size and improve the performance of these systems. However, it is often difficult to grasp how these devices deteriorate, and in turn difficult to determine the correct intervals to replace them.

In a previous study, the authors proposed a lifetime evaluation method for electronic signalling equipment installed in sheltered wayside environments or in equipment boxes [1]. As a result, it was possible to identify the shortest failure point of the target equipment under fixed environmental conditions set in advance, and to predict the equipment lifetime. However, it is necessary to consider the difference in installation conditions of target equipment and the future environmental changes of electronic equipment along railway lines, so it is necessary to provide some leeway in the operating environment conditions. As a result, an excessive margin is set, which may underestimate the lifetime.

In addition, the maintenance of railway facilities is shifting from conventional time-based maintenance (TBM) to condition-based maintenance (CBM). Various efforts are being made to shift to CBM for signalling equipment installed along railway lines.

Therefore, the authors of this paper aimed to improve the accuracy of lifetime estimation and apply it to CBM for wayside electronic equipment whose environment is likely to change depending on surrounding conditions. Furthermore, the authors constructed a new method for estimating the lifetime of equipment by capturing changes in the usage environment. This paper summarizes issues related to maintenance methods for electronic signalling equipment, describes the concept of a newly developed method for estimating lifetime based on sensing the usage environment, and verifies results

based on case studies.

2. Maintenance methods for electronic signalling equipment

2.1 Current status of maintenance and expectations for CBM

Traditionally, railway equipment maintenance has been dominated by TBM, in which inspections and maintenance work are performed at regular intervals. TBM has the advantage that a maintenance plan can be easily constructed. On the other hand, TBM has some challenges, such as the inability to respond to sudden failures and the need to update equipment while securing a large margin in the long term. In order to solve these TBM related problems, the shift to CBM has been accelerating in recent years. The shift to CBM is expected to help identify signs of failure, reduce the need for regular manual inspections, and enable efficient equipment upgrades. Examples of current CBM initiatives in Japan include the monitoring of track and rolling stock equipment. There are high expectations for CBM as an innovative technology in the maintenance of railway facilities.

2.2 Application of CBM to electronic signalling equipment

A prerequisite for implementing CBM is understanding indications of failure in target equipment. Monitoring of track equipment and some rolling stock equipment can be said to be a good example of CBM because it is possible to directly sense deterioration indicators which lead to failures and to continuously monitor changes. On the other hand, there are many objects such as electronic signalling equipment whose deterioration itself or indications of deterioration are difficult to detect, and the application of CBM to this type of equipment has become an issue.

The authors therefore decided to develop a new method for predicting electronic signalling equipment life by capturing changes in the environment in which the equipment is installed. This method finds an estimated lifetime at the point with the shortest lifetime under preset usage environmental conditions, and monitors the usage environment during operation to correct the initial estimated lifetime. As a result, it is possible to indirectly estimate the state of deterioration in actual conditions, therefore, the authors believe that it can be applied as a means of realizing CBM even for objects where monitoring the state of deterioration directly is difficult.

In order to realize a lifetime estimation method based on usage environment sensing, it is important to have a mechanism in which the authors understand the usage environment of equipment to be evaluated, and the authors estimate the lifetime of the equipment using the prediction of future environmental changes. The former is a usage environment sensing method, and the latter is a lifetime estimation method which reflects sensing data. Chapters 4 and 5 describe the concept of each method. As a first step, Chapter 3 describes the lifetime estimation method under fixed environmental conditions set in advance.

3. Lifetime estimation method under fixed environmental conditions

3.1 Concept

Electronic equipment is normally composed of multiple substrates and electronic components, where ICs and capacitors are soldered on a printed circuit board. Therefore, failures which disrupt the operation of an entire piece of electronic equipment can be broadly divided into electronic component failures, printed circuit board failures and solder joint failures. From the results of past examinations of products collected from wayside signalling equipment, no rust nor cracks were found on the printed circuit boards, but cracks were found in solder joints. Therefore, the influence of stress factors on solder joints was considered relatively greater than that on printed circuit boards. Thus, the authors excluded printed circuit board failures from targets for lifetime estimation [1].

Table 1 shows the results of extracting the environmental stress factors which affect the useful life of wayside electronic equipment. Furthermore, among the stress factors shown in Table 1, those which are dominant factors in lifetime expectancy were selected based on field surveys. The selected results are temperature and humidity such as constant temperature, temperature change, and humidity. Therefore, as shown in Fig. 1, it was decided to use a dual approach to evaluate the lifetime of wayside electronic equipment: estimating the lifetime of electronic components (electronic component evaluation) and estimating the lifetime of solder joints (solder joints evaluation). Section 3.2 below describes a lifetime estimation method for electronic components [2].

3.2 Lifetime estimation method for electronic components (electronic component evaluation)

In electronic component evaluation, components which affect the main function of electronic equipment are extracted and the reliability test results of the extracted components are obtained from manufacturers. From the survey results of stress factors in the usage environment, failure mechanisms are identified. Secondly, by applying the reliability test results to the usage environment conditions using acceleration model formulas according to failure mechanisms,

Table 1 Results of extracting the environmental stress factors which affect the useful life of wayside electronic equipment

No.	Factor classification 1	Factor classification 2	Selected results ^{*1}	
1	Thermal factors	Steady-state temperature	Y	Depending on installation environment
2		Temperature change	Y	Depending on installation environment
3	Electrical factors	Electromagnetic wave/ surge	N	Random failure
4	Surrounding environmental factors	Atmosphere	N	Lower than standard value
5		Moisture/ humidity	Y	Depending on installation environment
6	Mechanical factors	Vibration, shock, acceleration	N	Lower than standard value
7		Bending, fatigue, sliding	N	None

*1 Y: affected, N: no effect

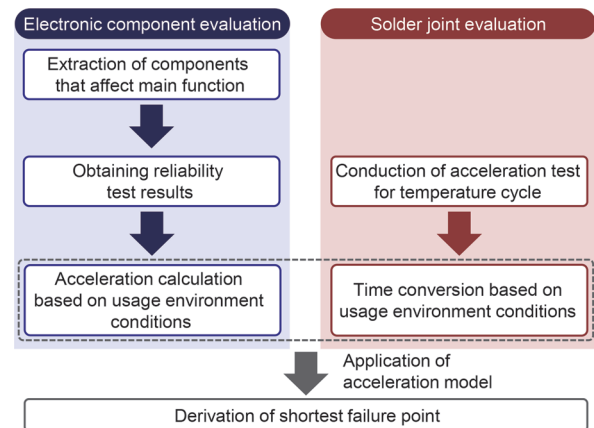


Fig. 1 Outline of lifetime estimation method for wayside electronic equipment

a cumulative failure probability is estimated. Finally, by calculating the number of years needed to reach a specific cumulative failure probability, the lifetime of each electronic component can be estimated for that usage environment.

3.2.1 Extraction of electronic components affecting overall function

The authors analyzed the degree of influence on overall function of electronic equipment when a specific electronic component failed. The degree of influence was defined according to a five-point scale: level 0: no effect, level 1: unstable operation, level 2: partial function stop, level 3: unit stop, level 4: device function stop. Extracting electronic components on level 2 or above, the authors selected, among the extracted components, the parts which are generally considered to have a limited lifetime, such as aluminum electrolytic capacitors or parts which generate a large amount of heat when switched on.

3.2.2 Acquisition of reliability test data

The authors acquired the manufacturers' reliability test data (number of samples, accelerated environmental conditions, test

4.2.1 Verification method

A piece of train detection equipment for railway level crossings installed in a wayside cabinet with a shielding plate which prevents direct sunlight is used as a test piece, and the temperature of the target point inside the equipment is treated as the true value. Here, the target points were the lifetime-determining components estimated under the usage environment conditions set in advance, and were selected as three components in total: two aluminum electrolytic capacitors and one photocoupler. As shown in Fig. 3, the authors carried out a test to estimate the temperature at the point where the useful life is determined based on the temperature inside the cabinet and the surface temperature of the target equipment. A thermocouple (T-type, manufactured by Hioki) was used as the temperature sensor, recording at 10-minute intervals, and a verification period of at least two weeks was secured considering weather comprehensiveness. For the verification, the average temperature for each day was calculated from the recorded data and compared. The reason for using the daily average temperature is described later in Section 5.1.

4.2.2 Temperature estimation results

Figure 4 shows the distribution of the difference from the measured temperature at the components where the useful life is determined, the average temperature in the cabinet on a daily basis, and the temperature difference from the surface temperature of the target equipment. In addition, the distribution of the difference from the space temperature in the ventilated case for meteorological instruments installed near the cabinet is also shown in Fig. 4. From Fig. 4, it can be seen that the temperature difference from the components where the useful life is determined has the smallest distribution range when the equipment surface temperature is used as the stan-

dard, and the distribution expands in the order of the space temperature inside the cabinet and the space temperature inside the ventilated case. Here, using Fig. 4, if each temperature sensor value is used as a reference, the temperature at the location where the useful life is determined can be estimated as “temperature sensor value + most frequent temperature difference \pm distribution range.” This means that the smaller the distribution range, the more accurately the target temperature can be estimated. Therefore, if the equipment surface with the smallest distribution range is used as a reference, the temperature of the photocoupler, for example, is going to be estimated as “the temperature sensor value on the equipment surface + the most frequent temperature difference of $9.8^{\circ}\text{C} \pm$ the distribution range of 0.8°C (cumulative frequency of 99%).” Table 2 shows the estimated temperature range at the components where the useful life is determined based on each temperature sensor value.

4.3 Accuracy of temperature and lifetime estimation for sensing points

Section 4.2 described the accuracy of estimating the temperature at the point where the useful life was determined, using the temperature sensors installed in each piece of equipment. In previous research, the authors examined a method for estimating temperatures inside cabinets using observation data of the Japan Meteorological Agency. The results show when the distance between a target cabinet and an observatory is less than 10 km, the average daily temperature can be estimated within $\pm 5^{\circ}\text{C}$ (including 99% cumulative frequency) [4].

In this section, the authors consider the effect of temperature estimation accuracy on lifetime estimation values. When estimating the useful life, the authors used aluminum electrolytic capacitors, for which temperature is the main factor of environmental stress, as an example. Here, the measurement accuracy of thermocouples (T type) used as the temperature sensors is $\pm 1^{\circ}\text{C}$, so the authors decided to consider it as a single sensor error. In this study, three types of methods were used for comparison: (A) a method in which a sensor is attached to each point where lifetime is determined, (B) a method in which a sensor is attached to each target equipment, and (C) a method using public data from observatories. The temperature estimation accuracy of the method using a sensor includes the error of the sensor alone and the estimation error from the surface temperature of the equipment housing. In other words, (A) when a sensor is attached to each part/location, the temperature estimation accuracy is $\pm 1^{\circ}\text{C}$ because only the error of the sensor is included. Similarly, in the case of (B) each target equipment, the estimation error from the surface temperature of the equipment housing is added to (A), resulting in $\pm 2^{\circ}\text{C}$. In (C) of the sensor-less method the error was treated as $\pm 5^{\circ}\text{C}$. Table 3 shows the relationship between temperature estimation accuracy and useful life estimation accuracy for each method, together with trial calculation conditions. From Table 3, the estimated lifetime expectancy corresponding to the error in temperature estimation accuracy was obtained for the comparative lifetime (true value: 13.6 years) for lifetime estimation accuracy verification. It is self-evident that the smaller the error in temperature estimation accuracy, the smaller the lifetime estimation error.

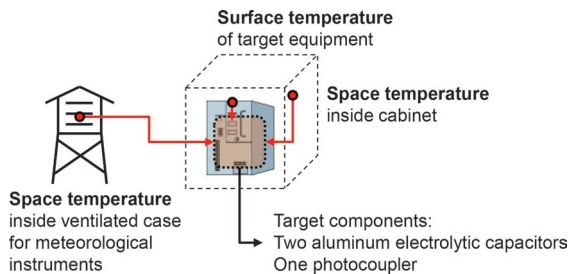


Fig. 3 Target points of measured temperature for verification test

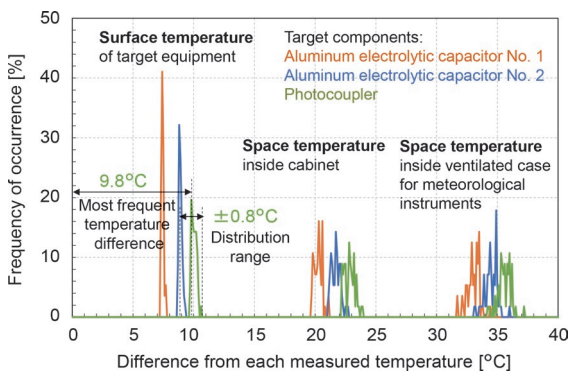


Fig. 4 Relationship between frequency of occurrence and difference from each measured temperature (daily average temperature basis)

5. Lifetime estimation method based on sensing data

The lifetime estimation method under fixed environmental conditions presented in Chapter 3 is useful for indoor electronic equipment, which is less prone to environmental fluctuations. In

Table 2 Estimated temperature range of components where the useful life is determined based on each temperature sensor value

Reference	Target components ^{*1}	Most frequent temperature difference [°C]	Distribution range [°C] (cumulative frequency of 99%)
Surface of target equipment	AEC No. 1	7.4	± 0.3
	AEC No. 2	8.8	± 0.5
	PC	9.8	± 0.8
Space inside cabinet	AEC No. 1	20.3	± 0.8
	AEC No. 2	21.7	± 1.0
	PC	22.8	± 1.1
Space inside ventilated case for meteorological instruments	AEC No. 1	33.5	± 1.8
	AEC No. 2	34.9	± 1.8
	PC	35.3	± 1.9

*1 AEC: Aluminum electrolytic capacitor, PC: Photocoupler

Table 3 Relationship between temperature estimation accuracy and useful life estimation accuracy for each method

Method	Sensing points	Temperature estimation accuracy [°C]	Lifetime estimation accuracy [year] ^{*1}
(A)	Each point where lifetime is determined	< ± 1	12.7 – 14.6 (-1.0 – 1.0)
(B)	Each target equipment	< ± 2	11.8 – 15.6 (-1.9 – 2.0)
(C)	Using public data from observatories	< ± 5	9.6 – 19.3 (-4.0 – 5.7)

*1 () indicates the difference with comparative life of 13.6 years
 Calculation condition: Aluminum electrolytic capacitor
 (reliability test: 105°C, 2000 hour, 22 samples, 0 failures)
 Cumulative failure probability: 1%. Component self-heating: 20°C
 Observatory data: Japan Meteorological Agency (Fuchu)

addition, it is considered that lifetime estimation under fixed conditions is also sufficiently useful for electronic equipment along railway lines by setting environmental conditions with a certain amount of margin. However, setting an excessive margin for environmental fluctuations may significantly shorten the useful lifetime estimation results, and it is difficult to make estimations which follow changes in the environment inside cabinets. Therefore, it is necessary to construct a method which senses the environmental variables of the selected acceleration model and uses the information as input values for lifetime estimation calculations. This chapter describes the concept and outline of a lifetime estimation method which extends the lifetime estimation method under fixed environmental conditions described in Chapter 3 and enables sensing data to be reflected [4].

5.1 Concept

An acceleration model is used to convert the reliability test data to the usage environment. At this time, in order to represent changes in the usage environment over time, the acceleration model is discretized with respect to time and integrated to estimate useful life. In discretization L_1 is the lifetime under the usage environment, L_0 is the test time, p is the discrete time interval, n is the total number of discretized times, and AF_i is the acceleration factor at each discretized time. The mathematical model is shown in (4).

$$L_1 = \sum_{i=1}^n \frac{1}{p} \cdot L_0 \cdot AF_i \quad (4)$$

In addition, applying the discretized acceleration model expressed by (4) to the typical acceleration models for aluminum electrolytic capacitors and photocouplers shown by (1) and (2) yields (5) and (6). Here, T_{li} is the operating temperature at each discretized time, and J_{li} is the operating current density at each discretized time.

$$L_1 = \sum_{i=1}^n \frac{1}{p} \cdot L_0 \cdot 2^{\left(\frac{T_0 - T_{li}}{10}\right)} \quad (5)$$

$$L_1 = \sum_{i=1}^n \frac{1}{p} \cdot L_0 \cdot \left(\frac{J_0}{J_{li}}\right)^n \cdot \exp\left[\frac{E_a}{k} \cdot \left(\frac{1}{T_{li}} - \frac{1}{T_0}\right)\right] \quad (6)$$

Both (5) and (6) show the contribution of the integrated temperature. On the other hand, in (6), if the current density considered as operating stress, is unlikely to change due to the circuit configuration, it is treated as a constant. The set value p of the time interval in the discretized acceleration model must be considered for each acceleration model. For example, in the case of a model in which integrated temperature makes a contribution, as in (5) and (6), it is important to capture the temperature peak because acceleration progresses on the high temperature side. In addition, in the case of an acceleration model which is affected by temperature cycles, the difference between the daily maximum and minimum temperatures makes a contribution, thus the time interval should be at least one day. Therefore, it was decided to set the time interval to one day for electronic signalling equipment.

5.2 Overview

The lifetime estimation method based on sensing data, which is composed of the discretized acceleration model described in Section 5.1 as the core part, consists of three algorithms for actual lifetime calculation, future estimation, and anomaly detection based on sensing data. This section provides an overview of each.

5.2.1 Actual lifetime calculation

The actual lifetime calculation algorithm uses the discretized acceleration model to convert the degree of deterioration progression in the usage environment into the reliability test time. At this time, each set value p of the time interval is associated with the test time. For example, Fig. 5 shows an image of actual lifetime calculation when 1,000 hours at 105°C is shown as reliability test data for an aluminum electrolytic capacitor. When used at 75°C for 100 days, the acceleration factor per day is 8 times according to (5), which translates to 3 hours of test time per day. In other words, 100 days usage environment is equivalent to 300 hours of test time, and it can be expressed as deterioration which has progressed by 30%.

When considering an arbitrary cumulative failure probability, since the acceleration factor does not change, the authors use (3) described in Section 3.2 and the shape parameters of the Weibull distribution to adjust the reference test time. In the above example, assuming 22 samples, 0 failures, and a shape parameter of 4, it takes 1,000 hours at a cumulative failure probability of 10% and 556 hours at a cumulative failure probability of 0.1%.

5.2.2 Future estimation

The future estimation algorithm estimates future sensing data and estimates the time to reach useful life (deterioration pace) by applying the actual value calculation algorithm shown in subsection 5.2.1 based on the estimation results of the sensing data. Tempera-

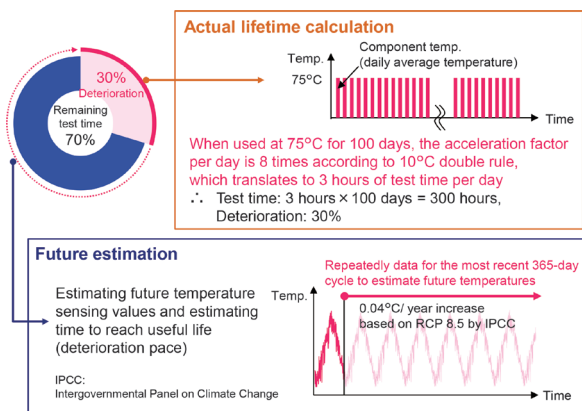


Fig. 5 Overview of actual lifetime calculation and future estimation when 1,000 hours at 105°C is shown as reliability test data for aluminum capacitor

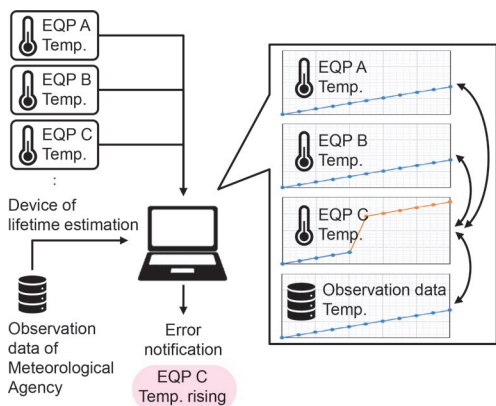


Fig. 6 Image of anomaly detection using sensing data in the adjacent cabinet and the observation station data

ture varies greatly throughout the year at many points in Japan. Therefore, as shown in the lower part of Fig. 5, the authors accumulated daily temperature sensing values for one year and repeatedly applied them as data for the most recent 365-day cycle to estimate future temperatures.

In addition, considering global warming, the worst-case scenarios for greenhouse gas emissions described in the Fifth Assessment Report of the United Nations Intergovernmental Panel on Climate Change (IPCC) are assumed. Based on this scenario (Representative Concentration Pathways, RCP 8.5), the temperature increase over the next 100 years is estimated to be 4°C (0.04°C/year) [5].

5.2.3 Anomaly detection

The anomaly detection algorithm detects anomalous changes in the usage environment from sensing data and notifies the management terminal and so on. In addition to year-round fluctuations, the sensing temperature is affected by abnormal heating of the target equipment, replacement of other equipment in the same cabinet, changes in the number of other equipment, and changes in the surrounding environment. Temporary temperature changes such as opening and closing the cabinet's door do not greatly affect the useful lifetime of the target equipment, however permanent changes cannot be ignored. Therefore, anomaly detection is required to accu-

rately identify constant temperature environmental changes, excluding changes in sensing values due to climate change. Single sensing data requires time until detection.

Therefore, the authors decided to detect anomalies by comparing the sensing data in the adjacent cabinet or the observation data of the Japan Meteorological Agency. Figure 6 shows an image of anomaly detection. In both cases, the average temperature for each day is compared with the sensing data in the adjacent cabinet and the observation station data for the target sensing data. For example, a temperature difference threshold value for abnormality detection is determined from the mutual difference, and if the determined threshold value is continuously exceeded, it is regarded as abnormal. This method enables rapid detection of constant changes other than climate change.

6. Case study

The authors created a tool which implements the lifetime estimation method based on the sensing data shown in Chapter 5, and carried out a case study on future estimation, using aluminum electrolytic capacitors mounted inside wayside electronic equipment as an example. Table 4 shows the conditions of the case study. Observatory data from the Japan Meteorological Agency (started January 1, 2001, Fuchu) was used as the temperature sensing value for each day, and the component temperature was determined by adding a heat generation of 25°C. A trial calculation was also made of the life expectancy range assuming a sensor error of $\pm 1^\circ\text{C}$. Figure 7 shows the results of lifetime estimation up to a cumulative failure probability of 10% (B10 life) assuming that observatory data are true values.

In the upper part of Fig. 7, the red line shows the actual temperatures obtained up to this point in time, and the green line shows the future temperature estimation values which were repeatedly applied as data for the most recent 365-day cycle, taking into account a temperature rise of 0.04°C/year. The lower part of Fig. 7 shows the change in the time to reach the end of life (degradation pace), with the horizontal axis representing the elapsed time and the vertical axis representing the remaining useful lifetime. The green line shows the result of lifetime estimation based on temperature. As a result, the life expectancy is 9.8 years out of a remaining life of 10 years, and the estimation error is within half a year. On the other

Table 4 Conditions of the case study

Conditions	Content/ value	Remarks
Target component	Aluminum Electrolytic Capacitor	
Tested time	2,000 hours	
Tested temperature	105°C	
Tested sample	22 samples	0 failure
Usage environment temperature	Observatory data from the Japan Meteorological Agency (Fuchu)	Started January 1, 2001
Component self-heating	25°C	
Estimating future temperatures	Repeating data for the most recent 365-day cycle	+0.04°C/ year
Discrete time interval	Daily	Daily average temperature
Acceleration model	10°C double rule	Attached Eq. (5)
Confidence level	90%	
Shape parameter	4	
Cumulative failure probability	10%	

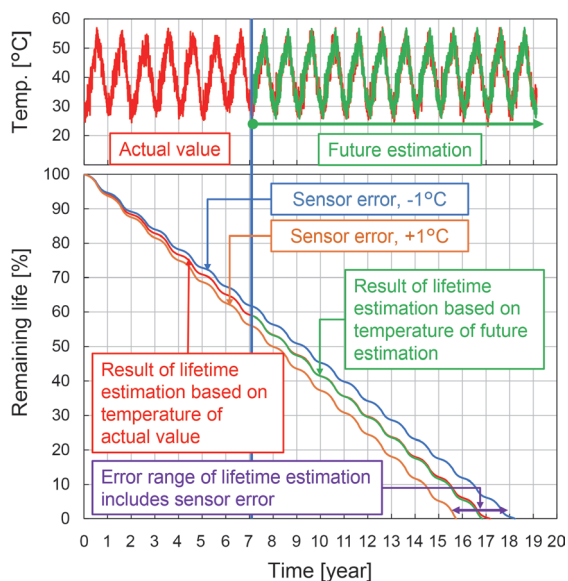


Fig. 7 Result of lifetime estimation up to cumulative failure probability of 10% in case study of aluminum capacitor (10 years before the end of life, assuming that observatory data are true values)

hand, under the conventional fixed environmental conditions, a margin of $\pm 5^{\circ}\text{C}$ was provided, thus if a trial calculation was made under the same conditions, the life expectancy would be 4.9 years, which is shorter than the remaining life of 10 years. It was shown that an improvement was achieved. A similar case study was also carried out using observatory data from other periods (both 1981 and 1991, starting on January 1, Fuchu), and the margin of error was about half a year at 10 years before the end of life. This result suggests that when formulating a replacement plan, it is possible to select annual replacement points 10 years before the end of useful life. However, considering the sensor error and the temperature estimation error of the target location, the error range of lifetime estimation expands, therefore it is necessary to consider the sensor configuration according to required life estimation accuracy.

7. Conclusions

This paper described the issues related to maintenance methods

Authors



Hiroyuki FUJITA
Senior Researcher, Signalling Systems Laboratory, Signalling and Operation Systems Technology Division
Research Areas: Signalling Systems, Automatic Train Protection, Reliability



Kentaro TSUBAKI
Researcher, Signalling Systems Laboratory, Signalling and Operation Systems Technology Division (Former)
Research Areas: Signalling Systems, Reliability



Ken TAKASAKI
Researcher, Signalling Systems Laboratory, Signalling and Operation Systems Technology Division
Research Areas: Signalling Systems, Reliability



Naoyuki OKO
Researcher, Signalling Systems Laboratory, Signalling and Operation Systems Technology Division (Former)
Research Areas: Signalling Systems, Reliability

for electronic signalling equipment, and also described the concept of the new lifetime estimation method based on usage environment sensing and verification results for this method through case studies.

In the useful lifetime estimation method based on usage environment sensing, temperature was assumed to be the main factor of environmental stress on the useful life of electronic signalling equipment, and accuracy of temperature based estimations to determine useful life was derived from the temperature measurement results for each target piece of equipment. In addition, this paper presented the concepts of actual lifetime value calculation, future prediction, and anomaly detection based on sensing data for the lifetime estimation method built around a discretized acceleration model.

The result of a case study on future estimation in particular, showed that the method achieved prediction errors of less than half a year for equipment with 10 remaining years of lifetime expectancy. By using this estimation method, it is possible to improve lifetime estimation accuracy, and it is thought that railway operators can use it to formulate timelier replacement plans. In addition, the authors believe that the lifetime estimation method is applicable as a means of achieving CBM for electronic signalling equipment because it can estimate the actual deterioration state based on the equipment's usage environment.

References

- [1] Kunisaki, A., Fujita, H., Nomura, T., Ishii, T., "Lifetime Evaluation Method for Electronic Equipment of Wayside Signalling Systems," *QR of RTRI*, Vol. 62, No. 2, pp. 110-117, May 2021.
- [2] Fujita, H., Niwa, J., Arai, H., "Development of Lifetime Evaluation Method for Electronic Interlocking Equipment in Consideration of Usage Environment," *RTRI Report*, Vol. 32, No. 5, pp. 23-28, 2018 (in Japanese).
- [3] Matsuoka, T., "Reliability Test for Quality Assurance of the Electronic Component," *Journal of the Adhesion Society of Japan*, Vol. 50, No. 10, pp. 318-325, 2014 (in Japanese).
- [4] Fujita, H., Tsubaki, K., Takasaki, T., Oko, N., "Lifetime Estimation of Signalling Electronic Equipment Based on Sensing Information of Usage Environment," *RTRI Report*, Vol. 36, No. 8, pp. 37-44, 2022 (in Japanese).
- [5] *Climate Change 2013: The Physical Science Basis*, Fifth Assessment Report of the IPCC, 2013.

Verification of the Applicability of Fifth Generation Mobile Communication Systems to Railway Operations

Kazuki NAKAMURA

Telecommunications and Networking Laboratory, Information and Communication Technology Division

Takayasu KITANO

Train Control Systems Laboratory, Signalling and Operation Systems Technology Division

Kunihiro KAWASAKI

Research and Development Promotion Division

Taishi OOMI

Kenzaburo FUJISHIMA

Shun ICHIKAWA

Hitachi, Ltd.

The 5th generation mobile communication system (5G), provided by mobile network operators (MNOs), is expected to dramatically improve three characteristics, namely, “enhanced Mobile Broadband (eMBB),” “Ultra-Reliable and Low Latency Communications (URLLC),” and “massive Machine Type Communication (mMTC),” compared to conventional mobile communication systems. The introduction of 5G services in railways is expected to lead to the introduction of new applications that could not be realized with conventional ground-to-train communication systems. Therefore, this paper outlines our current research on the introduction of public 5G services provided by MNOs to railway operations and the results obtained so far.

Key words: 5th generation mobile communication system, public network, train operation, Local 5G, FRMCS

1. Introduction

Mobile communication systems are indispensable for railways, such as train radio systems that provide communication between running trains and the ground, and communication-based train control systems, which have been widely introduced in recent years. Currently, most mobile communication systems used in railway operators are built on private networks that are designed, built, and managed by railway operators themselves.

In Japan, Mobile Network Operators (MNOs) began providing 5th generation mobile communication system (5G) services in stages from 2020, and wireless communications are expected to improve significantly compared with their past performance. 5G has features such as the ability to transmit more information in real time, a feature which is expected to improve the functionality of current applications and introduce new applications for train operations. In addition, railway mobile communication systems, which are currently built mainly on private networks, are expected to improve network availability and train operation efficiency through a hybrid configuration of private and public networks which utilize public 5G services provided by MNOs. Furthermore, it is expected that replacing private networks with public networks may reduce human resources and equipment costs required for installation and maintenance of the system.

However, no method has been established at present to utilize public services provided by MNOs that share transmission paths with general users for applications such as wireless train control and automatic operation, which are expected to be introduced in the future, to achieve safer and more stable train operations. Therefore, the authors evaluate the transmission quality, such as throughputs and latency, of 5G in the railway environment where there are many unknowns, and verified specific applications [1]. The purpose of this study is to establish a method for railway operators to apply public

5G services to their railway operations.

In this paper, after introducing an overview of 5G and its application to railways in Japan and overseas, we report on the evaluation results of transmission quality conducted using Local 5G on a test line in the Railway Technical Research Institute (RTRI).

2. Overview of 5G and service deployment in Japan

2.1 Overview of 5G

Mobile communication systems serviced by MNOs have provided services based on new specifications about every 10 years, starting with the car phone service launched in 1979. Today, information transmission, such as video and text, has become an important service, as represented by smartphones and tablets with displays.

With 5G, the purpose of the information to be transmitted has shifted from the conventional “transmission of information accessed by people” to “transmission of information that can be used by people and things”. This means that the basic concept is to connect all kinds of things to the network.

Therefore, 5G not only features “enhanced Mobile Broadband : eMBB,” which has been the focus of functional improvements in mobile communication systems with each generation update, but also introduces two new features, namely, “Ultra-Reliable and Low Latency Communications : URLLC” and “massive Machine Type Communication : mMTC” [2]. For example, regarding the eMBB feature, it is planned to achieve 20 Gbps data transmission, which is approximately 100 times faster than the 3.9-generation mobile communications system (LTE) currently in use. As for the URLLC features, the latency is expected to be about 1 ms, which is about 1/10 of that of LTE. Furthermore, in mMTC features, the number of devices that can be connected at the same time, which was only a few

in LTE, is expected to increase to 1 million devices/km², so that it is envisaged that everything around us will be connected to the network. It should be noted that not all three of these features can be satisfied simultaneously, and specialization in one of them will limit the other two features.

In Japan, frequencies in the 3.7 GHz, 4.5 GHz and 28 GHz bands have been allocated for 5G services. These frequency bands are differentiated by referring to the 3.7 GHz and 4.5 GHz bands collectively as Sub 6 and the 28 GHz band as millimeter-wave (millimeter-wave generally means to frequencies above 30 GHz, where the wavelength is on the order of mm, but in 5G deployment the 28 GHz band is called millimeter-wave). Sub 6 and millimeter-wave differ in terms of the propagation characteristics of the radio wave and the bandwidth that can be used, and therefore the service areas and performance provided are different, so when used on railways, it is necessary to make a choice according to the application to be applied.

In addition, apart from services provided by MNOs, ‘Local 5G’ has also been institutionalized as a new scheme for local companies and municipalities to build and use their own private networks flexibly on a spot basis within their own buildings and sites [3].

In Japan, frequencies used by Local 5G are allocated the adjacent frequencies to those used by MNOs (4.5 GHz and 28 GHz bands). Therefore, the same hardware and equipment used by MNOs providing public network services can be used. This is expected to reduce the costs spent on equipment compared with conventional dedicated radio systems.

2.2 5G service deployment in Japan

In Japan, 5G commercial services have been offered by MNOs since the spring of 2020. Although there are differences among

MNOs, service areas are being expanded while also converting frequencies previously used for 4G/LTE. The fastest MNO has achieved a population coverage rate (the percentage of areas within a 500 m square where communication is possible in 50% or more of the areas) of more than 90% as of March 2022. In addition, service development targeting the railway industry is also underway, with the aim of providing 5G service coverage on platforms, inside stations, and on trains running between stations on major railway lines. Furthermore, the “Infrastructure Development Plan for a Digital Garden City Nation” announced by the Ministry of Internal Affairs and Communications [4] calls for a population coverage rate (the ratio of the population in a 500 m square area with 5G communication capability divided by the total population) of 95% by the end of FY2023 and 97% by the end of FY2025.

3. R&D trends for 5G application in railways

3.1 Expected scenarios for 5G application in railways

Table 1 shows possible scenarios in which 5G is expected to be applied in the railway environment. Applications that take advantage of the eMBB features include real-time transmission to the ground of information from, for example, security cameras installed on trains, vehicle status information data, and onboard sensing data, as well as the provision of high-quality video content for passengers from the ground to onboard trains. In addition, while each application has conventionally used a separate dedicated private radio communication system, the use of a common radio communication system for multiple applications is expected to reduce the number of radio devices (Fig. 1).

Table 1 Characteristics of 5G and situations where it is expected to be used in railways

Characteristics of 5G	Target specifications	Expected application in railway system
enhanced Mobile Broadband (eMBB)	Data Rate 20 Gbps(DL) 10 Gbps(UL)	• High resolution video images (Operational use / Passenger service use)
Ultra-Reliable and Low Latency Communications (URLLC)	Latency 1 ms	• Train Control (including Automatic Control) • Remote Control of Maintenance cars
massive Machine Type Communication (mMTC)	Connection density 10 ⁶ /km ²	• Surveillance of wayside condition • Surveillance of wayside equipment

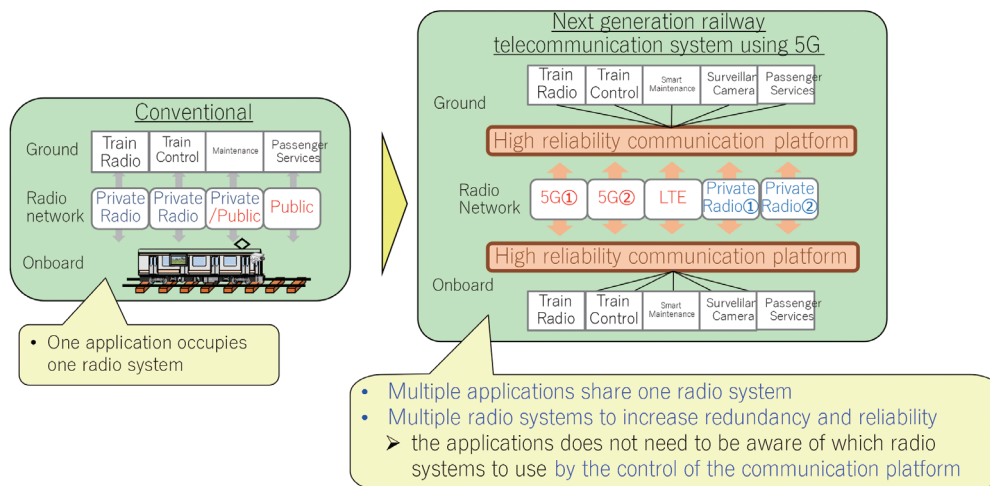


Fig. 1 Image of the radio system configuration for ground-to-train communication systems

The URLLC feature is expected to be used for communication-based train control systems, increasing train interval density in automatic train operation, and remote operation of maintenance vehicles in combination with transmission of high-precision images using eMBB features.

The mMTC feature is expected to be used for simultaneous collection of various sensor data expected to be installed in railway facilities where Condition Based Maintenance (CBM) is currently being introduced, and for provision of information to a large number of passengers.

Furthermore, attention is also being focused on network slicing technology, which enables the providing of services that virtually specialize in the performance of any of the above-mentioned three features, or services with guaranteed bandwidth similar to dedicated networks. Although network slicing has been established as a technology, it is currently unknown in what form MNOs will provide services using this function to users. Therefore, since it will depend on the needs of the user (railway operators) and the business development policy of MNOs, future trends need to be carefully watched.

3.2 R&D trends towards the introduction of 5G in railways

3.2.1 Trends in Japan

In order to apply 5G in railways, various railway operators are conducting demonstration experiments in collaboration with MNOs [5-7]. Most of the demonstration experiments use the features of eMBB and evaluate the transmission of high-quality video during movement. In these demonstration experiments, successful transmission of 4K and 8K quality video in the Sub 6 and millimeter-wave frequency bands has been reported between the inside of a high-speed Shinkansen train and a ground station temporarily installed along the railway line. These experiments are considered to have demonstrated the possibility of transmitting to the ground high quality video from security cameras inside the train and from forward monitoring cameras, which are expected to play an important role in future automated driving.

3.2.2 Trends overseas

Overseas, especially in Europe, train radio systems have been standardized using the GSM-R (Global System for Mobile communications - Railway) mobile communications system, which is based on second-generation mobile communications system technology with additional railway-specific functions. This system has been used in many countries, mainly on cross-border inter-connect-

ed lines. However, more than 20 years have already passed since its introduction and the service is scheduled to be discontinued by 2030. Therefore, a new train communication system that seamlessly utilizes multiple communication systems including 5G is being studied in the FRMCS (Future Railway Mobile Communication System) project of the International Union of Railways (UIC) [8]. The project is also working with the European Telecommunications Standards Institute (ETSI) and the 3rd Generation Partnership Project (3GPP), which standardizes mobile communication systems, to integrate railway specific functions in the 5G specifications.

In the FRMCS, the system configuration is considered to satisfy the required transmission quality by combining multiple wireless communication systems, rather than using only 5G as shown in Fig. 1 (Fig. 2) [9]. Furthermore, the FRMCS summarizes the latency and reliability performance requirements for each scenario (Table 2), which is also published as a Technical Specification (TS) by the 3GPP [10]. These scenarios and quality requirements are also considered to be useful for the study of 5G application in Japan. Furthermore, in Europe, the 5GRail project [11] started at the end of 2020 to demonstrate various FRMCS specifications, and efforts are being made to realize the project using experimental lines established in Germany and France.

In Europe, it was decided to extend the frequency band used by conventional GSM-R with a view to be applying 5G, and to allocate a new 1,900 MHz band exclusively for railways. It is therefore planned to use both private networks using these frequencies and public networks, depending on the classification of the transmitted data.

Thus, although the FRMCS is a project mainly targeted for introduction of 5G in Europe, there is a movement in the UIC and in the Asia-Pacific region to study a next-generation railway mobile communications system based on FRMCS. Therefore, we will continue to watch developments regarding spillover effects on Japan, and if necessary, we will plan to carry out research and development with a view to make some proposals from Japan.

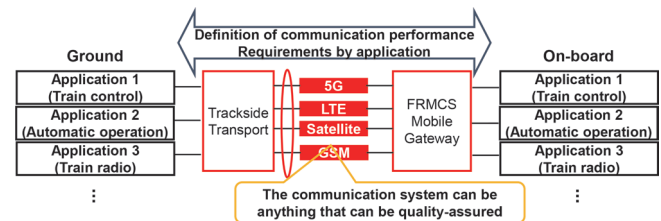


Fig. 2 Proposed configuration of the next generation communication system in the FRMCS

Table 2 Examples of Performance requirements for rail scenarios in 3GPP Technical Specification [10]

Scenario	End-to-end latency	Reliability	Speed limit	User experienced data rate	Examples of Railway applications
Voice Communication for operational purposes	≤100 ms	99.9%	≤500 km/h	100 kbps-300 kbps	● Train Radio
Critical Video Communication for observation purposes	≤100 ms	99.9%	≤500 km/h	10 Mbps	● CCTV in Train
Very Critical Video Communication with direct impact on train safety	≤100 ms	99.9%	≤500 km/h	10 Mbps-20 Mbps	● Forward supervision on Train ● Remote control system
	≤10 ms	99.9%	≤40 km/h	10 Mbps-30 Mbps	
Standard Data Communication	≤500 ms	99.9%	≤500 km/h	1 Mbps-10 Mbps	● Monitoring of train condition ● Monitoring of equipment
Critical Data Communication	≤500 ms	99.9999%	≤500 km/h	10 kbps-500 kbps	● Traffic control system
Very Critical Data Communication	≤100 ms	99.9999%	≤500 km/h	100 kbps-1 Mbps	● Train control system ● Automatic driving system

Note: All values in Table 2 are target values and assumes the use of a dedicated network for rail communication.

4. Transmission quality evaluation for the use of 5G in railway operations results of experiments

As described in the previous chapter, regarding the performance evaluation of 5G in railways, some railway operators and MNOs have already collaborated to carry out demonstration tests on video transmission, etc., using the features of eMBB, with a focus on passenger services, etc., and its effectiveness has been demonstrated. On the other hand, the performance evaluation of 5G which is necessary to realize safer and more stable train operation, such as communication-based train control and future automatic operation, is still insufficient. Therefore, the authors decided to carry out a study aimed at applying 5G to the transmission of critical information related to the safe and stable operation of trains. In the study, it is necessary to understand the true performance of 5G without the influence of general users, and it is desirable to verify the system in a variety of transmission environments and conditions. Therefore, as a first step, a Local 5G system, which is a private network using 5G technology, was constructed on the site of the RTRI so that an evaluation could be carried out under arbitrarily set system operation and verification conditions to study the performance and applicability of 5G.

4.1 Overview of the Local 5G system within the RTRI

The Local 5G system installed along the RTRI's test line uses 5G in the 28 GHz band for data transmission and a 2.5 GHz band private BWA (private LTE) system for the network (anchor) for exchanging control signals between base station and terminal, configured in a Non-Stand-Alone (NSA) system.

Local 5G systems institutionalized in Japan are limited in their use to their own land. Therefore, when building the system, two antennas were installed, each with a determined position, type, and direction to enable communication with trains running on the test line, while limiting the service area to the site of the RTRI (Fig. 3).

4.2 Evaluation method

For the evaluation, a quality evaluation system including a high reliability communication platform [12] corresponding to Trackside Transport (ground side) and FRMCS Mobile Gateway (on-board) was constructed (Fig. 4), referring to the network structure considered in the FRMCS shown in Fig. 2. The high reliability communication platform controls the priority of the transmitted data according to the communication quality required by the application on the vehicle side and on the ground side (server side), respectively. Furthermore, when multiple communication systems are available, the

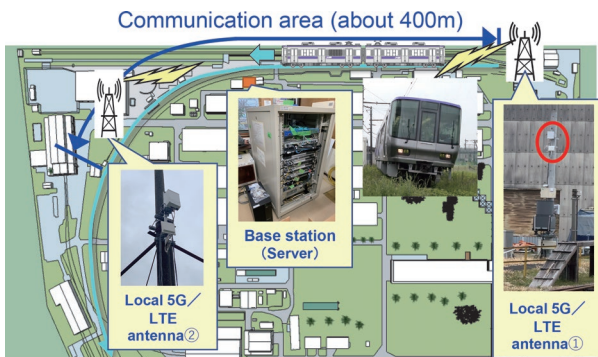


Fig. 3 Local 5G installations in RTRI test line

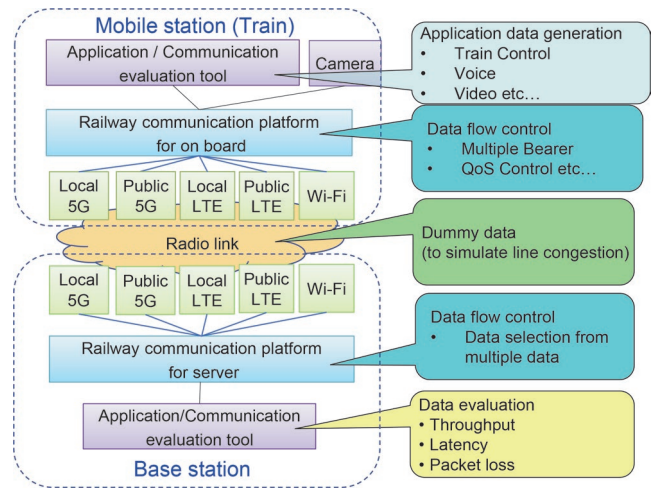


Fig. 4 Structure of the quality evaluation system

communication system to be used is controlled to satisfy the required transmission quality. When receiving data, the system extracts only the necessary data from the data received via multiple communication systems and transfers the data to the appropriate application.

In the quality evaluation system, the 'application simulation/communication evaluation tool' on the transmitting side generates simulated packets on the assumption of some applications, and evaluates the transmission quality using the packets delivered to the 'application simulation/communication evaluation tool' on the receiving side. The evaluation items were throughputs, latency, and packet loss rate. The received power in the wireless part was also recorded at the same time. In addition, the transmission quality was evaluated not only when data simulating the assumed application was transmitted alone, but also when the bandwidth was shared with other users by applying a load with dummy packets.

4.3 Evaluation results

4.3.1 Performance check of Local 5G

First, the performance of the constructed Local 5G and private LTE were tested. The results of measuring the throughputs and the round-trip latency time (round-trip time: RTT) between the running train and the ground are shown in Fig. 5 and 6. As a result, it was confirmed that throughputs close to the specifications (specification value: 530 Mbps) were generally obtained when the base station was occupied by only one terminal, if it was located near the base station antennas as shown in Fig. 5. In addition, a decrease in throughput was observed at handover (Local 5G: around 330 - 360 m, private LTE: around 260 - 290 m before). Also, from Fig. 6, the RTT of Local 5G was about one-third of that of private LTE up to the handover point, and furthermore, the fluctuation of the RTT was small. However, the RTT of Local 5G was more than 40 ms during the handover of Local 5G. This is assumed to be due to a combination of factors, such as a decrease in received signal power from the base station and an increase in the time required in handover due to the NSA system. It has been confirmed that the throughput decreases due to handover when data is transmitted only by Local 5G can be reduced and steady communication can be achieved by simultaneously transmitting data by Local 5G and private LTE using a highly reliable communication platform.

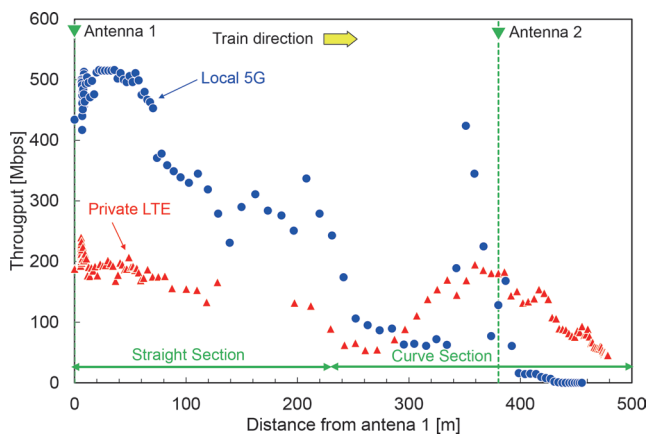


Fig. 5 Example of measured downlink throughput

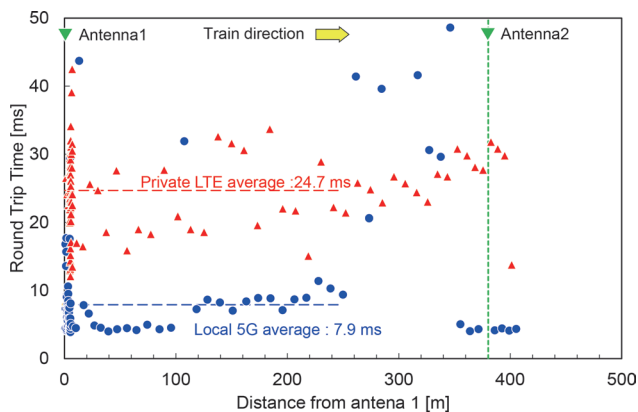


Fig. 6 Example of measured round trip time

4.3.2 Evaluation of transmission quality assuming application

This section reports the results of an evaluation of transmission quality assuming railway applications such as train control, train radio (voice) and surveillance cameras using Local 5G. This evaluation was carried out by generating simulated data for each of the assumed applications and transmitting them using Local 5G. Table 3 shows the assumed applications, the size of the simulated packets generated, the transmission cycle and the required transmission quality. In addition to tests conducted with the train terminal fixed at a point where signals from the base station could be obtained stably, tests were also conducted with the line intentionally loaded with dummy packets (ground to train: 500 Mbps, train to ground: 100 Mbps), assuming a congested line in the public network.

As a result, it was confirmed that data could be transmitted with the required transmission quality (packet loss ratio: PLR less than 10^{-6}) even when the line was congested in the test using packets simulating train control. On the other hand, in tests with packets simulating train radio, the packet loss on Local 5G alone did not satisfy the desired transmission quality. Therefore, an evaluation was carried out using Local 5G and private LTE in parallel using the High Reliability Communication Platform, which is one of the methods considered to be effective for quality improvement. As a result, it was confirmed that the transmission quality improved and that the required transmission quality (PLR less than 10^{-3}) could be satisfied. These results show that for applications such as train control and train radio, the required transmission quality may be satisfied even when using public 5G services by utilizing multiple radio systems on a highly reliable communication platform. Although the

Table 3 Assumed applications and communication requirements for evaluation

#	Application	Date size (Bytes)	Interval (ms)	Transmission rate (kbps)	Target
1	Train control	256	200	10.24	PLR: $<10^{-6}$ RTT: <200 ms
2	Train radio (Voice)	256	20	102.4	PLR: $<10^{-3}$ RTT: <200 ms
3	Video	1232	1	9,856.0	PLR: $<10^{-3}$ RTT: <200 ms

required transmission quality could not be satisfied for the transmission of video images, it has been confirmed that packet loss can be reduced by using Local 5G and private LTE at the same time using a reliable communication platform. Therefore, it is expected that the required transmission quality can be achieved in the future by improving the transmission quality of the system through the deployment of SA schemes and carrier aggregation by bundling multiple frequencies.

4.3.3 Transmission quality evaluation by priority control in the radio sections

This section reports the results of verifying the effectiveness of the priority control function in the radio section. Normally, packet priority control in the radio section is possible in base station equipment by changing a value called QoS Class Identifier (QCI). Since the Local 5G base station equipment used in this study did not implement this function, the function was verified in a private LTE base station equipment. The verification was carried out in areas with high (strong) and low (weak) signals from the base station in a stationary state. In each area, the verification was carried out under simulated and uncongested conditions by transmitting simulated packets. The indicator used for the verification was the RTT to see the effect of latency due to improved congestion. Figure 7 shows the test results. From Fig. 7, it was confirmed that in the uncongested situation, the effect of priority control was not observed regardless of the signal strength, but in the congested situation, the effect of priority control was observed. The effect is particularly significant in situations where the received signal is weak and the network is congested, and in this test environment, the RTT was reduced to less than one-tenth of the original RTT. The results were obtained in LTE, but the function is expected to be implemented in 5G as well. Therefore, it is thought that the provision of such priority control services by telecommunications carriers in the future will give the effect of reducing latency, although the extent of this effect is unknown, and it can be greatly expected to be utilized in railway operation work.

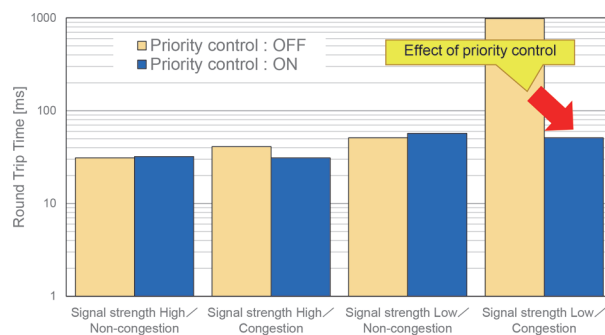


Fig. 7 Effects of priority control (LTE) [1]

5. Conclusion

In the future, we plan to study further the application feasibility evaluation in detail, including verification using Sub 6, the SA and public network, and how to utilize Local 5G in the railway environment, as well as to prepare guidelines outlining the procedures, etc. for railway operators to apply 5G.

References

- [1] Nakamura, K., Kitano, T., Takeuchi, K., Kawasaki, K., Oomi, T., Fujishima, K., Kunifuji, T. and Bekki, K., "Study of applicability of 5G technology to train control systems," presented at the *13th World Congress Railway Research (WCRR2022)*, Birmingham, June 6-10, 2022, IP19-1.
- [2] Ministry of Internal Affairs and Communications, Japan (MIC), "WHITE PAPER Information and Communications in Japan Year 2020," 2020.
- [3] MIC, "Announcement of the Local 5G Implementation Guidelines," *Newsletter of the MIC*, Vol. 30 No. 4, December 2019.
- [4] MIC, "Announcement of Infrastructure Development Plan for a Digital Garden City Nation," *MIC Press Release*, https://www.soumu.go.jp/main_sosiki/joho_tsusin/eng/pressrelease/2022/3/29_03.html, March 29, 2022 (Accessed Mar. 9, 2023).
- [5] NEC, "NEC contributes to high-definition video transmission test utilizing 5G conducted by NTT Communications, NTT DOCOMO and TOBU RAILWAY -Transmission of video to a train running at approximately 90 km/h-," *NEC Press Release*, https://www.nec.com/en/press/201902/global_20190205_01.html, February 5, 2019 (Accessed Mar. 9, 2023).
- [6] NTT DOCOMO, "DOCOMO Achieves World's First 5G Communication Between High-speed Bullet Train and Experimental Base Stations," *NTT Docomo Press Release*, https://www.docomo.ne.jp/english/info/media_center/pr/2019/0930_00.html, September 30, 2019 (Accessed Mar. 9, 2023).
- [7] NTT DOCOMO and JR EAST, "NTT DOCOMO and JR EAST Verify Stable 5G Communication aboard ALFA-X Shinkansen Test Train Running at 360 km/h -Setting the stage for advanced, high-value mobility aboard high-speed trains-," *JR EAST Press Release*, <https://www.jreast.co.jp/e/press/2020/pdf/20210128.pdf>, January 28, 2021 (Accessed Mar. 9, 2023).
- [8] UIC, "Future Railway Mobile Communication System," <https://uic.org/rail-system/frmcs/>, (Accessed Mar. 9, 2023).
- [9] ETSI, "Rail Telecommunications (RT), Future Rail Mobile Communication System (FRMCS), Study on system architecture," *ETSI Technical Report*, TR103 459 V1.2.1, 2020.
- [10] 3GPP, "Mobile Communication System for Railways," *3GPP Technical Specification*, TS 22.289, V17.0.0, 2019.
- [11] 5GRail, <https://5grail.eu/>, (Accessed Mar. 9, 2023).
- [12] Ishino, M., Suzuki, T., Igarashi, Y., Oomi T., Fujishima, K., Nakamura, K. and Kitano, T., "A Study on High-reliability Communication Platform using Public Mobile Networks for Railway Applications," *IEICE Technical Report*, Vol. 122, No. 6, RCS2022-1, pp. 1-6, April 2022 (in Japanese).

Authors



Kazuki NAKAMURA
Senior Chief Researcher, Head of Telecommunications and Networking Laboratory, Information and Communication Technology Division
Research Areas: Wireless Communication System, Electro Magnetic Compatibility



Takayasu KITANO, Ph.D.
Senior Researcher, Train Control Systems Laboratory, Signalling and Operation Systems Technology Division
Research Areas: Communication-Based Train Control System, Wireless Communication System



Kunihiro KAWASAKI
Principal Researcher, Research and Development Promotion Division
Research Areas: Wireless Communication System, Electro Magnetic Compatibility



Taishi OOMI
Senior Engineer, Hitachi, Ltd.
Research Areas: Train Signalling System, Communication-Based Train Control System



Kenzaburo FUJISHIMA
Senior Engineer, Hitachi, Ltd.
Research Areas: Communication-Based Train Control System, Wireless Communication System



Shun ICHIKAWA
Engineer, Hitachi, Ltd.
Research Areas: Communication-Based Train Control System

Analytical Study on the Influence of Friction on Unstable Oscillation of Pantograph

Yuki AMANO Shigeyuki KOBAYASHI
Current Collection Laboratory, Railway Dynamics Division

The sliding of contact strips generates a frictional force acting on traveling pantographs in the horizontal direction. A large coefficient of friction can lead to unstable oscillation of the pantograph. To analyze this oscillation, a 2-degree-of-freedom (2-dof) pantograph model considering frictional force has been proposed. However, this model does not study the stability of the contact strip attached to a pantograph. Therefore, this study proposes a 2-dof contact strip model considering vertical and pitching movements. In addition, excitation tests of an actual contact strip for a Shinkansen train were carried out to identify its dynamic characteristics. We then applied a complex eigenvalue analysis to the contact strip model to analyze its stability.

Key words: pantograph, sliding friction, unstable oscillation, stability analysis

1. Introduction

As shown in Fig. 1, an electric train pantograph uses a linkage mechanism consisting of a parallel guide bar, a coupling rod, an upper frame, and a lower frame to achieve vertical movement of the pantograph head. A sliding member called a contact strip is attached to the upper surface of the pantograph head, and electric power is supplied to the train when the contact strip is in contact with a contact wire. When the train runs, the point of contact between the contact wire and the contact strip moves, generating a frictional force due to the sliding motion. The work done by the generated frictional force is converted into excitation energy by the characteristics of the pantograph itself, so that an unstable oscillation caused by the frictional force may occur. In fact, pitching vibrations have been reported to be caused by frictional force [1].

It is also known empirically that only a part of the area of contact strips in the travel direction side comes into contact with the contact wire due to a rotating moment caused by the frictional force shown in Fig. 2. This phenomenon is called “one-sided contact” of the contact strip. When a member with such non-uniform contact pressure is used for sliding, unstable oscillation due to the coupled translational and rotational motion of the friction member may occur, as in the case of disc brake squeal [2]. Therefore, a detailed study of the pitching motion of contact strips is also necessary, but the previous studies, including models based on the flexible multi body dynamics [3] and models based on the finite element modeling [4], have not examined the pitching motion of contact strips in detail.

Therefore, in this study, we speculated that unstable oscillation is caused by the coupled pitching and vertical vibration of contact

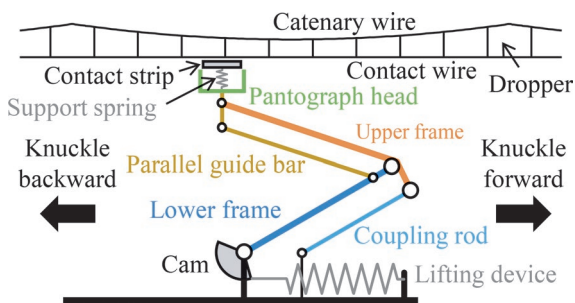


Fig. 1 Conceptual diagram of Shinkansen train single-arm pantograph

strips and constructed analytical models of the contact strip section corresponding to overhead conductor rail cases. The reason for targeting overhead conductor rail running is that the frequency of unstable oscillations prior to occurrence of contact losses is expected to be high, and the response of a catenary is small at such a high frequency. In fact, in a reproduction test of unstable oscillation using High-speed Test Facility for Pantograph/OCL Systems (HiPaC) [5] that can simulate sliding with an actual contact wire, it was confirmed that very high frequency vibration was generated.

Based on the developed analytical model, we proposed a method for evaluating the stability of contact strips. Furthermore, the natural frequencies and mode shapes of contact strips were identified by excitation test using contact strips of an actual pantograph, and the stability of the actual pantograph for overhead conductor rail running was numerically investigated.

2. Analytical studies

According to Ref. [6], the wear rate of contact wires is reported to be higher at extremely low running speeds (approx. 15 km/h or less) close to when the pantograph is stationary (approx. 10 m before and after) in Shinkansen station yards compared with other speed sections. According to Ref. [7], the combination of PHC contact wire [8] and iron-based sintered alloy contact strip [9] used in the northern Kyushu Shinkansen (Hakata to Shin-Yatsushiro) and the northern Tohoku Shinkansen (Hachinohe to Shin-Aomori) shows that the coefficient of friction between these materials increases to about 0.8 at extremely low running speeds (about 15 km/h or less). Since unstable oscillation may occur when the coefficient of friction increases in this manner, this report focuses on unstable oscillation in single-arm Shinkansen train pantographs at extremely

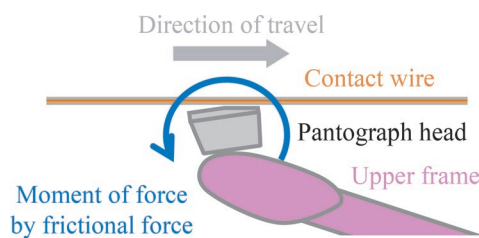


Fig. 2 Conceptual diagram of ‘one-sided contact’ of a contact strip

low running speed.

Figure 3 is a schematic diagram of a contact strip and its support structure (hereinafter referred to collectively as the ‘contact strip section’). The upper side of Fig. 3 shows a plan view, and the lower side shows a cross-sectional view along the center line of the plan view. In the coordinate system $O-XYZ$ in Fig. 3, X -axis and Z -axis are parallel to the rail and sleeper directions, respectively, and the origin of the coordinate system is centered on the X -axis and Z -axis directions of a contact strip. The dynamic characteristics of the pantograph’s linkage mechanism have anisotropy in the rail direction, and the positive and negative axes are distinguished in Figs. 1 and 3 by noting knuckle forward and knuckle backward, respectively. As shown in Fig. 3, the contact strip section under consideration consists of a multiple parallelogram-shaped contact strip arranged in the sleeper direction in the plan view, with the center and both ends supported by a support spring and support beams, respectively. In the range where a stopper does not act, a contact strip can oscillate around the Z -axis (pitching direction) with the joint between the pantograph head and the support beam as the fulcrum. Therefore, in order to investigate the effect of these structures on the stability of pantographs, we constructed an analytical model in which only the contact strip section is extracted. In the following, we describe the modeling of the contact strip section and the equations of motion and eigenvalues of the system obtained from the constructed model.

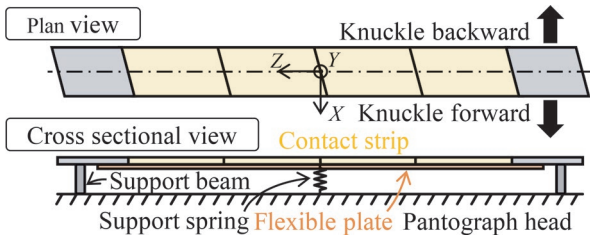


Fig. 3 Schematic diagram of a contact strip and support structure for Shinkansen train

2.1 Analytical model

The vertical motion of the contact strip section is mainly caused by the flexible plate and the support spring, and the pitching motion is mainly caused by the rigid body rotation of the contact strip caused by the clearance of the support. Therefore, considering this form of motion, we constructed an analytical model shown in Fig. 4, which facilitates analytical investigation. Figures. 4(a) and 4(b) show the analytical model and free-body diagram. The model consists of a concentrated mass that imitates a contact strip supported by a massless cantilever beam that imitates a support spring and a support beam. The details of this analytical model are described below.

As mentioned above, only a part of the area on the travel direction side of a contact strip makes contact with the catenary while sliding. When one-sided contact occurs, a pitching rotational moment is generated in contact strips due to the influence of uneven contact pressure acting on the surface of contact strips and a decrease in the contact area with contact wire. Therefore, in the analytical model proposed in this report, a concentrated load is applied to a position displaced by a in the rail direction from the center of the support point of the cantilever beam, as shown in Fig. 4(a), to simply represent the one-sided contact as described above. In Fig. 4(a), m is the equivalent mass of the contact strip; J , the equivalent mo-

ment of inertia of the contact strip; b , the width of the contact strip in the Y direction; l_b , the axial length of the cantilever beam supporting the contact strip; k_y , the equivalent stiffness considering the supporting spring and the longitudinal stiffness of the support beam; EI , the bending stiffness of the cantilever beam; c_y and c_θ , the vertical and rotational viscous damping coefficients of the contact strip; y and θ , the vertical displacement and angular displacement around the center of gravity of the contact strip; y_b and θ_b , the vertical displacement and angular displacement at the joint between the pantograph head and the cantilever beam; and f_c , the contact force between the overhead conductor rail and the contact strip.

Next, the free-body diagram in Fig. 4(b) is described. Here, for the purpose of visibility, the vertical force is shown in warm colors in Fig. 4(b), and M represents the bending moment acting between a contact strip and a cantilever beam. Note that the damping force is omitted in the free-body diagram. Coulomb friction is assumed in the friction model, and a dynamic frictional force proportional to the contact force acts in the horizontal direction. Assuming that the coefficient of friction is μ and that the frictional force acts in positive direction when a train runs in the knuckle forward (positive direction on the X -axis), the positive direction of the frictional force μf_c is the direction shown in Fig. 4(b). When considering the case that a train runs ‘knuckle backward’ (negative direction on the X -axis), the value of the coefficient of friction μ is set to be negative. Since the axial length of the cantilever beam l_b is relatively short, the horizontal displacement of the cantilever beam end is neglected. Introducing this approximation, the horizontal force balance in the free-body diagram allows us to approximate the shear force between a contact strip and a cantilever beam as μf_c , as shown in Fig. 4(b).

The contact between the contact strip and the overhead conductor rail is represented by the penalty method using the contact element shown in Fig. 4(b) (henceforth the contact spring), and the stiffness of the contact spring is set to k_c .

2.2 Derivation of the equations of motion

In this section, we derive the equations of motion for the analytical model described in the previous section. First, the equations of motion for the vertical and rotational directions of a contact strip are as follows from the free-body diagram shown in Fig. 4(b):

$$\begin{cases} m\ddot{y} = -c_y\dot{y} - k_y(y - y_b) - f_c \\ J\ddot{\theta} = -c_\theta\dot{\theta} - f_c a + \mu f_c b - M \end{cases} \quad (1)$$

The inclination of the ends of the beam corresponds to the angular displacement of the contact strip and applying Myosotes’ formula [10] for the cantilevered beam, the following equation is obtained.

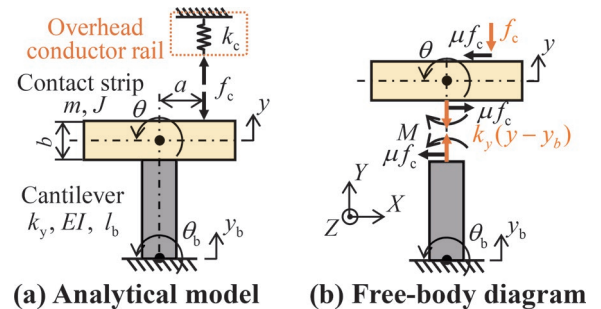


Fig. 4 Analytical model and free-body diagram

$$\theta - \theta_b = \frac{\mu f_c l_b^2}{2EI} + \frac{M l_b}{EI} \quad (2)$$

Furthermore, the contact force f_c between the overhead conductor rail and the contact strip is given by:

$$f_c = k_c(y + a\theta) \quad (3)$$

Substituting (2) and (3) into (1) and eliminating f_c and M yields the final equation of motion.

$$\left. \begin{aligned} \mathbf{M}\ddot{\mathbf{y}} + \mathbf{C}\dot{\mathbf{y}} + \mathbf{K}\mathbf{y} &= \mathbf{0} \\ \mathbf{M} &= \begin{bmatrix} m & 0 \\ 0 & J \end{bmatrix}, \mathbf{C} = \begin{bmatrix} c_y & 0 \\ 0 & c_\theta \end{bmatrix} \\ \mathbf{K} &= \begin{bmatrix} k_y + k_c & ak_c \\ (a - \mu l)k_c & k_\theta + a(a - \mu l)k_c \end{bmatrix} \\ \mathbf{y} &= [y \quad \theta]^T, k_\theta = EI/l_b, l = b + l_b/2 \end{aligned} \right\} \quad (4)$$

For simplicity, y_b and θ_b are neglected in (4). We introduce this approximation since the frequency of the unstable oscillations prior to contact loss is expected to be very high, so that the response of the linkage is very small at such high frequencies. In fact, it can be read from the results of Ref. [11] that the mass and moment of inertia of the linkage and the collector head trajectory have a smaller effect on stability of contact strips. However, since the influence of the linkage cannot be completely ignored, and the possible influence of y_b and θ_b on the stability of the system is a subject for the further study. In mathematical terms of (4), it can be found that this corresponds to neglecting the mass of the disk of the pin-disk model [12]. However, the analytical model proposed in this paper differs from the pin-disk model in that it can represent misalignment of the center of rotation of the sliding members. In addition, when focusing only on the contact strip section, it is sufficient to consider only one direction, since the same equations of motion for knuckle forward and knuckle backward can be expressed by reversing the signs of a and m . Therefore, in the following, only the case $a > 0$ will be treated.

2.3 Analytical investigation of stability

As shown in (4) in section 2.2, the stiffness matrix becomes an asymmetric matrix due to the action of frictional forces. The eigenvalues of the system containing such an asymmetric matrix are complex numbers, the real part of which represents the negative value of the modal damping rate. Therefore, if even one of the complex eigenvalues of the system has a positive real part, the system becomes dynamically unstable. When the real part of a complex eigenvalue is positive, the larger its absolute value, the more unstable the system becomes. Therefore, in this report, the stability of the analytical model is evaluated using the maximum value of the real part of the complex eigenvalues.

For a damped two-degree-of-freedom system (hereinafter referred to as a "damped system") such as the one in (4), it is difficult to derive its eigenvalues analytically. However, the existence of non-negligible damping in actual pantographs is important to consider because the value of damping affects the stability of the system. On the other hand, in the case of an undamped two-degree-of-freedom system in which the damping term in (4) is neglected (hereinafter referred to as "undamped system"), the eigenvalues can be derived analytically. Therefore, in this report, eigenvalues of the undamped and damped systems are obtained analytically and numerically, respectively, and their stability is discussed. Numerical investigation of the damping system is discussed in Section 3.2, and the stability of the undamped system is discussed analytically be-

low.

First, substituting $y = \mathbf{Y}e^{i\lambda t}$ into (4), we obtain the characteristic equation for the eigenvalue λ shown in the following equation.

$$\left. \begin{aligned} A\lambda^4 + B\lambda^2 + C &= 0 \\ A &= mJ \\ B &= mk_\theta + (k_y + k_c)J + a(a - \mu l)mk_c \\ C &= (k_y + k_c)k_\theta + a(a - \mu l)k_yk_c \end{aligned} \right\} \quad (5)$$

The above equation is a complex quadratic equation for λ . If λ^2 is a real number, then λ is a real or pure imaginary number, which means that an oscillatory solution cannot be obtained. On the other hand, if λ^2 is a complex number, then λ is also a complex number and an oscillatory solution can be obtained, and the conditional equation $B^2 - 4AC < 0$ (the conditional equation for the generation of unstable oscillations) is written down for μ to obtain the following equation.

$$\left. \begin{aligned} \mu &> \frac{1}{l} \left(\frac{J}{ma} f + a \right) \quad (a > 0) \\ f &= \frac{\left\{ \sqrt{k_c} - \sqrt{m(\omega_0^2 - \omega_y^2)} \right\}^2}{k_c} \\ \omega_y &= \sqrt{k_y/m}, \omega_0 = \sqrt{k_\theta/J} \end{aligned} \right\} \quad (6)$$

Equation (6) is a conditional expression based on the relation $\omega_0 > \omega_y$. If this relation is not satisfied, oscillatory divergence instability (called flutter instability) does not occur.

The right-hand side of (6) is always positive under the condition $a > 0$. This is thought to correspond to the fact that unstable oscillation is generated in a situation where the machine is moving in a one-sided contact situation. It can also be read that for $a \rightarrow \infty$ and $a \rightarrow 0$, the stable-unstable boundary shown in (6) asymptotically approaches the straight lines $a \rightarrow \mu l$ and $a \rightarrow 0$, respectively.

From f in (6), the right-hand side of (6) is smallest when ω_0 and $\sqrt{(k_y + k_c)/m}$ (hereafter referred to as ω_{ver}) coincide, indicating that even small values of the coefficient of friction can cause instability. On the other hand, Ref. [13] indicates that when only contact springs are used as contact elements, the stiffness k_c of the contact springs should be set to 100~1000 times k_y to prevent the influence of the penalty coefficient on contact force fluctuations below 100 Hz. Thus, we see that ω_0 does not coincide with ω_{ver} and that the instability increases as ω_0 increases and ω_y decreases. If k_c is very large relative to the other parameters, f in (6) can be approximated as 1. In such cases, measures such as increasing the ratio of J to m or decreasing l should be taken.

3. Parameter identification and stability discrimination using actual contact strip

3.1 Parameter identification

In order to numerically evaluate the stability of an actual pantograph, it is necessary to identify various parameters of the analytical model from the actual pantograph. Therefore, a pantograph head detached from the actual pantograph was fixed to a jig and subjected to excitation test, and the acceleration of the contact strip was obtained based on Maxwell's reciprocal theorem [10]. Figure 5 shows the location of the accelerometer and the location of the excitation. Figure 6 shows the gain and phase of the acceleration obtained by excitation at three locations on the straight-line $Z = -18$ mm. Figure 6 shows that three resonance points exist. The vibration pat-

terns at 39.1 Hz and 73.5 Hz are shown in Figs. 7(a) and 7(b). Figure 7 shows that first-order bending and pitching modes occur at 39.1 Hz and 73.5 Hz, respectively. Although not shown in the figure, second and third bending modes occur at 73.8 Hz and 183.5 Hz, respectively, and the effect of the second bending mode is shown in Fig. 7(b).

The bending and pitching modes described above are the modes to be modeled in the vertical and rotational directions in the analytical model. Therefore, an equivalent one-degree-of-freedom system was considered for these modes in terms of energy, and the equivalent parameters in the analytical model were calculated. The equivalent masses of the bending modes are generally the same regardless of the mode order because the mode shapes of the bending modes are mostly sinusoidal. The modal damping ratios for each mode were identified using the technique from Ref. [14]. The natural frequencies and the damping ratios for each bending mode are shown in Table 1, and the damping ratio for the pitching mode is 0.03. Here, f_y is the natural frequency in the vertical direction obtained by dividing ω_y by 2π , the vertical and rotational damping ratios are expressed as ζ_y and ζ_0 , respectively:

$$\zeta_y = \frac{c_y}{2m\omega_y}, \zeta_0 = \frac{c_0}{2J\omega_0} \quad (7)$$

As for the stiffness of the contact spring, it was decided to set it to a value about 1000 times greater than k_y , referring to the studies in Ref. [13]. These parameters are summarized in Table 2. Here, f_0 is the natural frequency in the rotational direction obtained by dividing ω_0 by 2π .

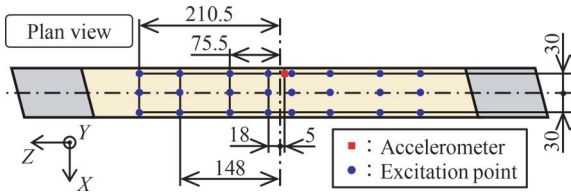


Fig. 5 Placement of accelerometer and excitation point

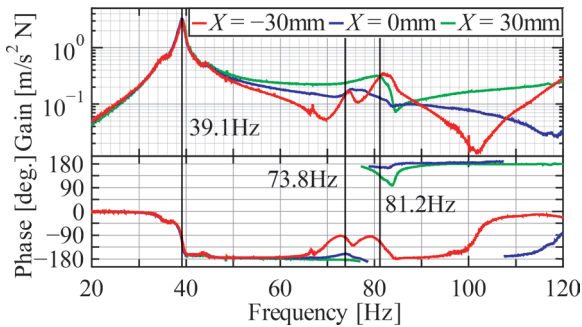


Fig. 6 Comparison of measured acceleration on straight line $Z = -18$ mm

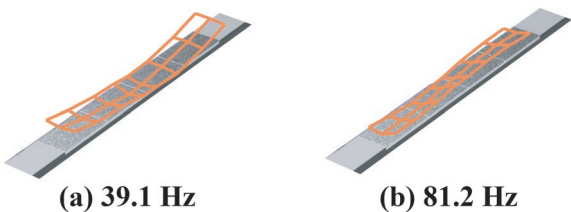


Fig. 7 Mode shapes at each resonance point

Table 1 Mode characteristics of each bending mode

Order	Natural frequency f_y [Hz]	Damping ratio ζ_y [-]
1	39.1	0.01
2	73.8	0.03
3	183.5	0.01

Table 2 Parameters of contact strip section and overhead conductor rail

m [kg]	2.35	b [mm]	10
J [kg · mm ²]	715	l_b [mm]	20
f_0 [Hz]	81.2	k_c [kN/m]	1.00×10^5
ζ_0 [-]	0.03		

3.2 Stability discrimination using analytical models

In this section, the maximum value ${}^R\lambda_{\max}$ of the real part of the eigenvalues indicating stability is calculated numerically for the damping system shown in (4) in section 2.2, using the parameters shown in Table 2.

First, Fig. 8(a) shows the transition of ${}^R\lambda_{\max}$ for the first bending mode as the contact position a and the coefficient of friction μ are varied. Here, the value of ${}^R\lambda_{\max}$ is shown as 0 when ${}^R\lambda_{\max}$ is negative (i.e., the system is stable) for better visibility. In Fig. 8(a), the contact position where the coefficient of friction μ is smallest in the unstable region is indicated by a white dot, and the value of the coefficient of friction μ_{\min} at that position is also shown in the figure. The value of μ_{\min} shown in Fig. 8(a) is 0.71, indicating that instability can occur for realistic parameters, considering the results of Ref. [9]. Similar calculations were performed for the second and third bending modes, and the values of μ_{\min} were found to be 1.65 and 0.79, respectively, indicating that the first-bending mode is most prone to instability. Therefore, a parametric study will be conducted for the first bending mode below.

Figures 8(b) and 8(c) show the transition of the stable-unstable boundary when only the value of l and J are changed for the parameters used in Fig. 8(a), respectively. From both figures, the unstable region shrinks as l decreases and J increases. Figure 8(c) shows that the vertices of the stable-unstable boundary generally pass through the backbone curve $a = \mu l/2$ (the derivation of the backbone curve is omitted) in the undamped system. This indicates that, for damping systems, if the value of the coefficient of friction μ_{\min} is known, the value of a , which is the most unstable, can be estimated. From Figures 8(a)-8(c), the stable-unstable boundary asymptotically approaches $a = 0$ and $a = \mu l$. From these results, the value of μ_{\min} can be used to estimate the rough range of the unstable region. Therefore, in the following, we will use the change in μ_{\min} to determine the trend of stability as the parameter is varied.

Next, Figs 8(d) and 8(e) show the change in μ_{\min} when only the damping ratio and natural frequency in each direction are changed for the parameters used in Fig. 8(a), respectively. Here, in Fig. 8(e), straight line $f_0 = f_y$ is shown as a dashed black line, and the switch between flutter instability and divergence instability is shown as a solid purple line. From Fig. 8(d), it can be read that the stability may deteriorate if appropriate damping is not provided in both the vertical and rotational directions. This is presumably due to the phase difference between vertical and rotational displacements that causes friction-induced unstable oscillation. Figure 8(e) shows that the instability increases with increasing f_0 and decreasing f_y in the region $f_0 > f_y$,

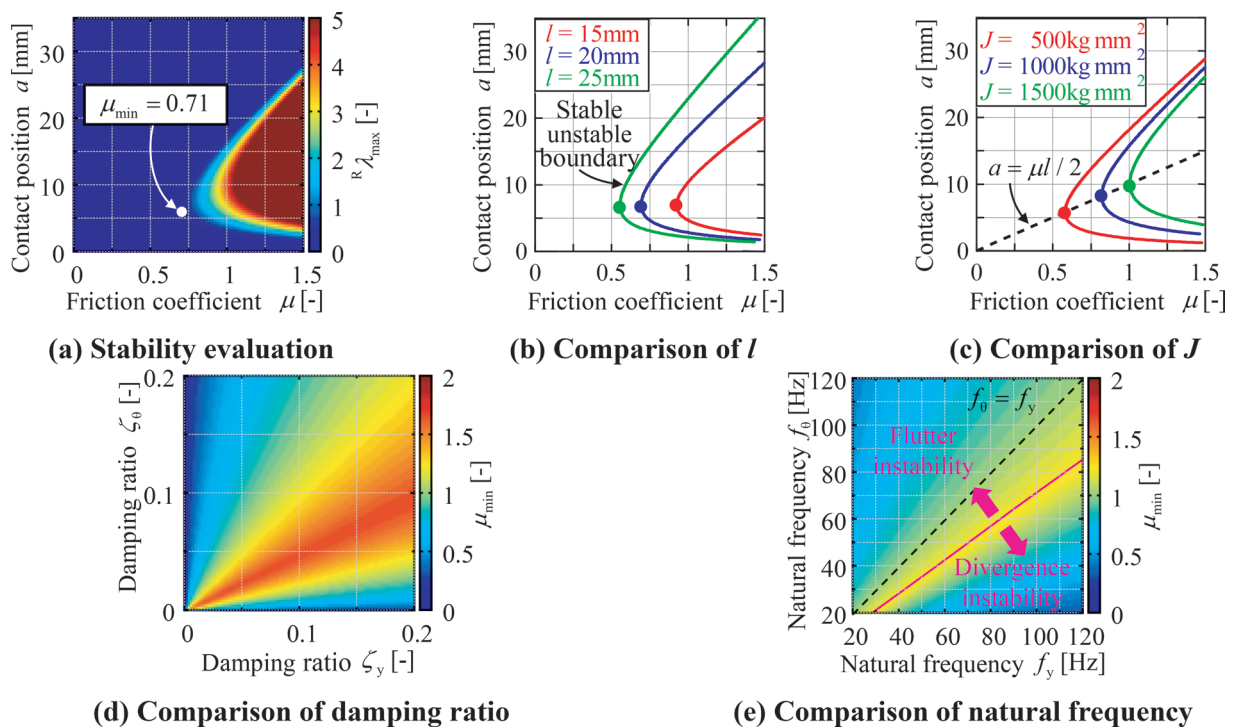


Fig. 8 Stability evaluation of actual contact strip using analytical model

and the flutter instability disappears near the straight line $f_0 = f_y$. This is a trend consistent with the findings from the undamped system. On the other hand, in the region of $f_0 < f_y$, the instability of divergence instability is increasing, so that the stability is not so high.

4. Conclusions

In this report, an analytical model of the contact strip corresponding to an overhead conductor rail running was developed and its stability was examined analytically. As a precondition for the development, it was assumed that unstable oscillation is caused by the coupling of pitching and vertical vibration of the contact strip. Furthermore, the natural frequencies and mode shapes of the contact strip were identified by excitation test using an actual contact strip. Using measurement result, the stability of the actual pantograph was numerically investigated. A summary of this report is given below.

- (1) It was found that stability can be improved by increasing the ratio of the equivalent moment of inertia to the equivalent mass of the contact strip, reducing the thickness of the contact strip or the axial length of the support beam. However, it is difficult to change the parameters described above independently, so that it is necessary to keep in mind their dependence when making design changes.
- (2) Stability discrimination was performed using parameters estimated by identified natural frequencies and mode shapes. The result showed that unstable oscillation can occur with realistic parameters. It was also found that appropriate adjustment of damping is necessary to improve stability.

In the future, we intend to establish a pantograph model with a linkage mechanism added to the contact strip section, upgrade the catenary model, and conduct an experimental study on instability phenomena.

References

- [1] Sakamoto, M., Kaku, H. and Suzuki, Y., "Pitching Measures for ED76-type pantograph," *R&M*, pp. 55-59, May 2012 (in Japanese).
- [2] Brian, F., Ardéshir, G., Nikolaus, H., and Karl, P., "A historical review on dry friction and stick-slip phenomena," *Applied Mechanics Reviews*, Vol. 51, pp. 321-341, May 1998.
- [3] Koyama, T., Nagao, K. and Ikeda, M., "Three-dimensional Simulation of Catenary/Pantograph Dynamic Interaction," *Quarterly Report of RTRI*, Vol. 62, No. 2, May 2021.
- [4] Qian, J. W., Chen, X. G., Zhang, H. W., Ouyang, H. and Zhou, R. Z., "Friction-Induced, Self-Excited Vibration of a Pantograph-Catenary System," *Journal of Vibration and Acoustics*, Vol. 135, No. 5, Oct 2013.
- [5] Koyama, T., "Development of High-speed Test Facility for Pantograph/OCL Systems," *Quarterly Report of RTRI*, Vol. 63, No. 2, May 2022.
- [6] Kubota, Y., "Pantograph Contact Strip for Shinkansen Vehicles and its Lubrication Technology," *Journal of Japanese Society of Tribologists*, Vol. 61, No. 3, pp. 167-172, 2016 (in Japanese).
- [7] Nemoto, K., Kubota, Y., "Effect of sliding speed on friction and wear between copper alloy contact wire and iron-based sintered alloy contact strip," presented at the *26th Jointed Railway Technology Symposium (J-RAIL 2019)*, Tokyo, Japan, December 4-6, 2019, Paper S7-4-2 (in Japanese).
- [8] Harada, S., Shimizu, M., Ikeda, K., Sato, J., Koyano, K. and Chikanari, K., "Development of Simple Catenary Equipment Using PHC Contact Wire for Shinkansen," *Quarterly Report of RTRI*, Vol. 49, No. 2, May 2008.
- [9] Kubo, S., Tsuchiya, H. and Kubota, Y., "Development of Iron-Base Sintered Pantograph Contact Strips for Shinkansen Electric Vehicles," *RTRI Report*, Vol. 20, No. 9, pp. 47-52, Sep. 2006 (in Japanese).

- [10] Den Hartog, J. P., “*Strength of Materials*,” Dover Publications, Inc., New York, pp. 85-90, 180-183, June 1961.
- [11] Kobayashi, S., Usuda, T. and Yamashita, Y., “Stability analysis of pantograph under frictional force,” *Transaction of the Japan Society of Mechanical Engineers*, Vol. 85, No. 878, 2019 (in Japanese).
- [12] Earles, S. W. E. and Lee, C. K. “Instabilities Arising from the Frictional Interaction of a Pin-Disc System Resulting in Noise Generation,” *Transactions of the ASME, Journal of Engineering for Industry*, Vol. 98, No.1, pp. 81-86, 1976.
- [13] Ikeda, M., “‘Gasen-do FE’ statement of methods,” *Vehicle System Dynamics*, Vol. 53, No. 3, pp. 357-369, 2015.
- [14] Brown, D. L., Allemang, R. J., Zimmerman, R. and Mergeay, M., “Parameter Estimation Techniques for Modal Analysis,” *SAE Technical Paper*, No. 790221, 1979.

Authors



Yuki AMANO
 Researcher, Current Collection Laboratory,
 Railway Dynamics Division
 Research Areas: Catenary-Pantograph
 Interaction, Dynamics of Machinery,
 Mechanical Vibration



Shigeyuki KOBAYASHI, Ph.D.
 Senior Researcher, Current Collection
 Laboratory, Railway Dynamics Division
 Research Areas: Catenary-Pantograph
 Interaction, Vibration Control

Structural Performance Evaluation of Existing Bridges Based on Acceleration Monitoring

Munemasa TOKUNAGA

Manabu IKEDA

Structural Mechanics Laboratory, Railway Dynamics Division

The aim of this study is to enable monitoring of structural performance conditions of concrete girders. We first developed a method to restore displacement waveforms using acceleration waveforms from passing trains by utilizing the linear vibration theory. Numerical experiments have shown that the method can estimate the maximum displacement within an error margin of approximately 5%. Furthermore, the equivalent linearized beam theory was extended to estimate reinforcing bar stress waveforms using the displacement waveform. These methods realized the structural performance evaluation of bridges such as riding comfort and fatigue fracture from acceleration measurements.

Key words: acceleration integration, deflection monitoring, structural performance, rebar stress, beam theory

1. Introduction

High-speed railways in Japan have been in operation for more than 50 years, and measures are being taken to deal with future aging deterioration of railway facilities. In addition, the density and speed of train operations are increasing. In order to ensure long-term stable operation in the future, it is necessary to maintain and manage structures by appropriately allocating labor and financial resources. In terms of maintenance management, it is possible to optimize resource allocation by quantifying and ranking the performance of existing bridges. However, structures are maintained qualitatively based on visual inspections while structural performance regarding train running performance and fatigue are not quantitatively evaluated. In order to accurately evaluate structural performance regarding train runnability and fatigue, it is necessary to periodically measure the deflection and stress of reinforcing bars, which is a problem because it is cost and labor intensive.

In the technical field of bridges, many attempts have been made to monitor their structural health using microelectromechanical system (MEMS) accelerometers for condition-based maintenance. For efficient maintenance, many studies have been conducted to evaluate condition changes using acceleration sensors installed on bridges. In these studies, natural frequencies and maximum amplitudes have been used as indices by applying constant monitoring measurement results to machine learning [1]. In structural design, indices such as acceleration and natural frequency may be calculated during the design stage of bridges. However, these indices are not directly linked to quantitative structural performance: the fractures of bridges and running safety of vehicles. Hence, although acceleration is obtained through constant monitoring [2], the actual measurement data cannot be fully utilized because the actual bridge performance is not linked to measurement results. From a bird's-eye view, this indicates a lack of design and maintenance technology that complements the relationship among the obtained pieces of information. In recent years, many Shinkansen bridges have been found to resonate during the passage of trains [3], as a result, phenomena related to structural performance changes during long-term service need to be elucidated.

Figure 1 shows the evaluation flow proposed in this paper. In this paper, in order to realize structural performance evaluation by acceleration monitoring in the maintenance management of existing bridges, Chapter 2 proposes an algorithm that enables integration of acceleration waveforms to obtain deflection waveforms during the

passage of trains. Chapter 3 proposes an algorithm to convert the overall deflection into the stress waveform of internal reinforcing bars. Chapter 4 describes applications of proposed methods to acceleration monitoring data in existing bridges. Finally, a condition-based maintenance by structural performance monitoring is shown.

2. Deflection Waveform Restoration Method by acceleration integral for simply supported bridges

2.1 Method

To restore displacement waveforms from acceleration integration of a simply supported bridge, a method based on parameter identification has been proposed [4]. However, this method has certain disadvantages: it is applicable only when the actual bridge response can be assumed as a linear system, the influence of modeling errors is large, the computational cost is large, and this is unsuitable for processing large amounts of data obtained by constant monitoring. Especially in the case of reinforced concrete (hereinafter referred to as RC) girders, the error of parameter time dependent variation due to bending cracks may not be negligible. This study investigates a method for restoring the displacement waveform using accelerations during the passage of trains based on linear vibration theory. Complicated factors, such as nonlinearities (such as cracks and the influence of train-bridge interaction, are not modeled, to make the method as non-parametric as possible.

Figure 2 shows the calculation flow of the proposed displacement waveform restoration obtained by integrating acceleration. The following conditions are assumed for adopting this method:

- The observation data are the acceleration waveform just below track and at the center of bridge span.
- The known data are the bridge span L_b and the type of passing train (L_t, a, b) treated as a constant value.
- Although the train wheel load p_0 is unknown, it can be treated as a constant in all vehicles.
- Train speed V km/h is known and constant as the train passes through bridge.

The right-hand side of the figure shows that this method restores only a small part of the low-frequency components of acceleration waveforms. Some parameters must be identified for this process. Regarding the external force characteristics, a theoretical

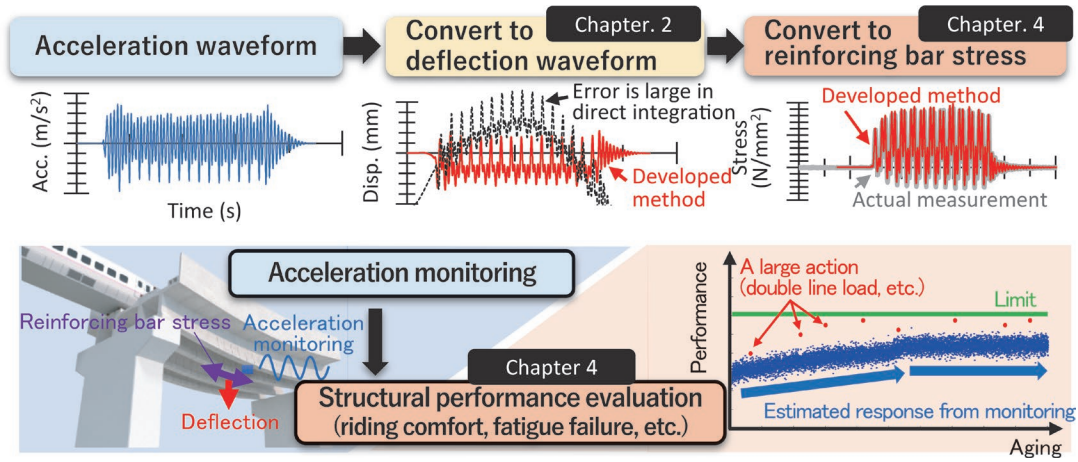


Fig. 1 Concept of investigation in this paper

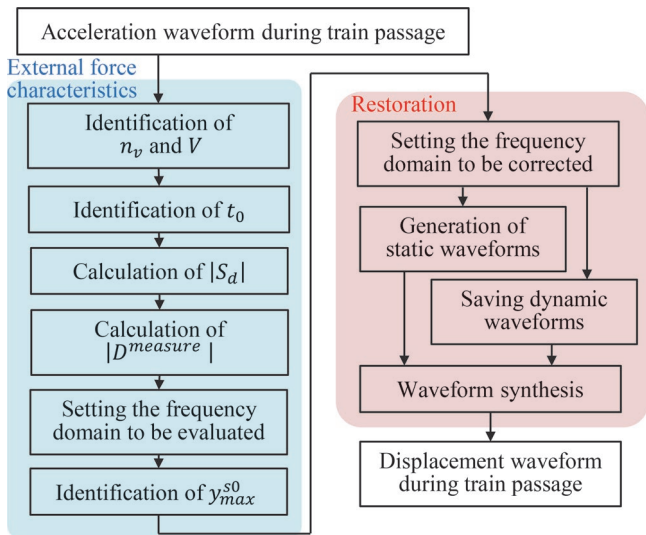


Fig. 2 Calculation flow of the proposed displacement waveform restoration

model is assumed using railway vehicle characteristics. The only parameter identified by the acceleration waveform is the unit static displacement $y_{max}^{s0,idf}$.

The measured acceleration is defined as a^{msr} for the time domain and as A^{msr} for the frequency domain. Based on the linear vibration theory, the frequency domain F_λ of the external modal force due to the train load and the transfer function S_d of the displacement are expressed by (1) and (2).

$$F_\lambda(\omega) = e^{-i\omega t_0} \left(1 + e^{-i\pi\Omega \frac{a}{L_v}} \right) \left(1 + e^{-i\pi\Omega \frac{b}{L_v}} \right) \frac{1 - e^{-i\pi\Omega n_v}}{1 - e^{-i\pi\Omega}} \frac{1 + e^{-i\pi\Omega \frac{L_b}{L_v}}}{1 - \Omega^2 \left(\frac{L_b}{L_v} \right)^2} \frac{1}{\omega_v} \quad (1)$$

$$\left(\Omega = \frac{\omega L_v}{\pi v} \right)$$

$$S_d = (-\Omega_b^2 + 2i\zeta_b\Omega_b + 1)^{-1} \quad (2)$$

Using the measured acceleration, $y_{max}^{s0,idf}$ is identified by (3).

$$y_{max}^{s0,idf} = \frac{1}{\omega_{e_2} - \omega_{e_1}} \int_{\omega_{e_1}}^{\omega_{e_2}} |(i\omega)^{-2} A^{msr} F_\lambda^{-1} S_d^{-1}| d\omega \quad (3)$$

ω_{e_1} and ω_{e_2} are the lower and upper limits, respectively, of the frequency that is the evaluation interval of the average value: $\omega_{e_1} = \max\{1, 0.1 \times 2\pi f_b\}$, $\omega_{e_2} = 0.6 \times 2\pi f_b$, $|S_d|$ of this identification region is approximately 1–1.3; its value does not change easily according to the damping ratio of the bridge, and it is not easily affected by amplification due to the integration of acceleration noise.

The low-frequency noise contained in measured acceleration is amplified through the integral operation, so that it is difficult to restore the data in a manner that can withstand evaluation. The error in the direct integration of acceleration mainly occurs since the noise mixed in the low-frequency region is amplified during time integration.

The proposed method decomposes the measured acceleration of bridge into a quasi-static component and a dynamic component, and modifies only the quasi-static component that is strongly affected by noise using the theoretical solution. Modified displacement D^{mdf} is expressed by (4):

$$D^{mdf} = \begin{cases} y_{max}^{s0,idf} F_\lambda S_d & (0 \leq \omega < \omega_m) \\ (i\omega)^{-2} A^{msr} & (\omega_m \leq \omega) \end{cases} \quad (4)$$

where ω_m is the restoration boundary angular frequency. In order to calculate F_λ , n_v , v , a , b , L_v , t_0 related to the axle arrangement, and ω_b , ζ_b related to the dynamic characteristics should be known in advance. The restored displacement waveform d^{mdf} is obtained by inverse Fourier transforming the D^{mdf} .

2.2 Validation

The proposed method is verified using the acceleration waveform a_ϵ with artificial noise ϵ added to the theoretical solution a_t .

The parameter related to the train is V ($V = 50, 100, \dots, 500$ km/h). The parameter related to the bridge is L_b ($L_b = 10, 20, \dots, 100$ m). The number of vehicles n_v is 12, the axle load p_0 is 120 kN, and the train approach time t_0 is 2 s, which is a fixed value. The following relationships are assumed for the unit length mass \bar{m} and the natural frequency f_b based on L_b . Here, \bar{m} is set as a single-track concrete bridge ($\bar{m}g = 100 + 1.5L_b$ kN/m), and f_b is set as a value assuming a relatively flexible bridge structure ($f_b = 50L_b^{-0.8}$ Hz). The damping ratio ζ_b is set as a fixed value of 2%.

Figure 3 shows an example of the restored displacement waveform in the case of $L_b = 50$ m and $V = 200$ km/h. These are the results

obtained when a relatively large noise is assumed ($\sigma_\epsilon = 0.020 \text{ m/s}^2$) when the number of vehicles n_v , train speed V , and dynamic characteristics f_b and ζ_b of the bridge are known. The figure shows the input acceleration, and the displacement estimation results on the time and frequency axes.

The time history of the displacement in the second part of the figure confirms that the corrected waveform d_t (gray line) and the modified waveform d^{mdf} by the proposed method (red line) match each other. In this way, the proposed method can accurately reproduce not only the maximum value but also the waveform. The fact suggests that the method is effective even when the number of repetitions (such as fatigue problems) is required for evaluation of fatigue in addition to the amplitude. The waveform d^{direct} obtained by direct integration (black dotted line), shifts with the passage of time due to long-period noise, and the correct displacement waveform cannot be obtained.

The third part of the figure shows the time history of the quasi-static displacement waveform of the modified part and the dynamic waveform of the measured part. They are calculated by $y_{max}^{s0,idf} F_\lambda S_d$ and the inverse Fourier transform of $(i\omega)^{-2} A^{msr}$, respectively. The figure shows that the former waveform is close to the static response of the train load and does not cause any long-period drift, whereas the latter waveform contains many dynamic components of the natural vibration mode.

The bottom of the figure shows the theoretically replaced $y_{max}^{s0,idf} F_\lambda S_d$ and the frequency response $(i\omega)^{-2} A^{msr}$ of the displacement obtained by directly integrating the acceleration waveform. $(i\omega)^{-2} A^{msr}$ tends to differ largely from the theoretical value in the region of approximately 1 Hz or less. The value, especially in the region of approximately 0.2 Hz or less, exceeds the theoretical value due to noise amplification. In the identification region of $y_{max}^{s0,idf}$, as shown in Eq. (3) (approximately from 0.4 to 1.2 Hz in Fig. 3), the two are almost the same, indicating that the two are not easily affected by noise in this area.

Figure 4 shows the estimation accuracy of the maximum value of the dynamic displacement y_{max}^{sd} when the noise standard deviation σ_ϵ is 0.001-0.020 m/s^2 . According to the figure, because the dynamic displacement is added to the static displacement $y_{max}^{s,ext}$, $y_{max}^{sd,ext}$ is naturally larger than $y_{max}^{s,ext}$. $y_{max}^{sd,ext}$ also increases at specific train speeds. This is because the train speed V is $3.6f_b L_v/m$ (km/h; m is the resonance order), which is the speed at which resonance occurs (at which the natural frequency of the bridge and the oscillation frequency of the train match). For example, when $L_b = 10 \text{ m}$, $V = 713, 357, \text{ and } 238 \text{ km/h}$ are the first- to third-order resonance velocities. A comparison of $y_{max}^{sd,ext}$ and $y_{max}^{sd,idf}$ confirms that the estimation error tends to increase when the speed is low, the span is long, and the noise is high.

In the region of $\sigma_\epsilon \leq 0.005 \text{ m/s}^2$ and $V \geq 150 \text{ km/h}$ in practice, $y_{max}^{sd,ext}$ and $y_{max}^{sd,idf}$ match, indicating that the dynamic displacement y_{max}^{sd} can be estimated within an estimation error less than 5%.

As the noise increases, the estimation error in the low-speed region tends to increase; however, even at low speeds of 100 km/h or less, when acceleration data with little noise can be obtained, displacement can be estimated with high accuracy. When noise increases, for example, due to installation conditions, the applicable range will be smaller.

These methods are capable of high-speed calculations of less than 1 second, which is about 500 times faster than conventional deflection evaluation methods based on inverse analysis.

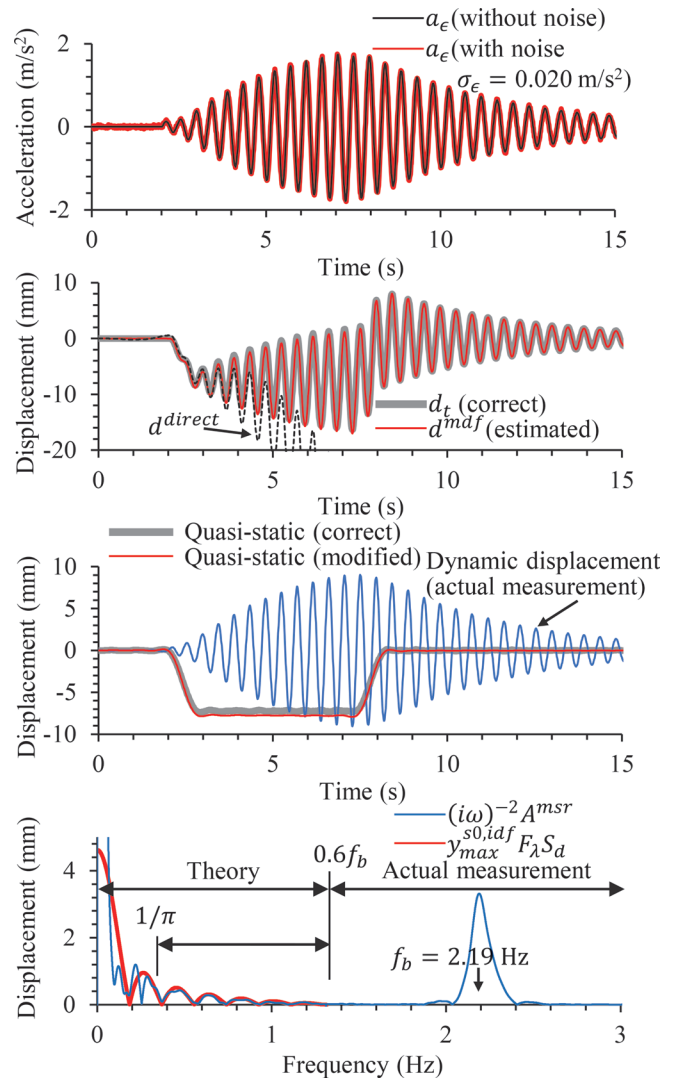


Fig. 3 An example of the restored displacement waveform ($L_b = 50 \text{ m}$, $V = 200 \text{ km/h}$)

3. Estimation method of rebar stress waveform by deflection measurement

3.1 Method

Among the structural performance of bridges, failure of members is caused by yielding of reinforcing bars and crushing of compressed concrete, and fatigue failure is caused by breaking of reinforcing bars. These structural performances are evaluated and checked by stress amplitude. Furthermore, in order to evaluate the fatigue failure of reinforcing bars, it is necessary to consider the number of repetitions, that is, the response history of the stress generated in reinforcing bars.

A concrete member with cracks is considered as a beam whose stiffness changes in the longitudinal direction. In actuality, the tensile stress of lower reinforcing bar behaves non-linearly with respect to the train load due to stress redistribution caused by bond losses. It is assumed that the vibration mode represented by the half-sine wave is dominant in the dynamic response of a beam when the displacement δ at the span center is obtained. Furthermore, if the ratio of the distance from the neutral axis position to lower reinforcing

bar and girder height H is set as β_H , the average strain ϵ_s^{ave} of lower reinforcing bar in the direction of track is given by (5).

$$\epsilon_s^{ave} = \beta_H H (\pi / L_b)^2 \delta \quad (5)$$

The stresses borne by the concrete at cracked cross-sections are redistributed to surrounding reinforcing bars due to cracks and deterioration of adhesion. Here, the ratio of the reinforcing bar strain ϵ_s^{cr} at the crack cross section to the average strain ϵ_s^{ave} of a reinforced concrete (RC) tensile member assuming a uniform member is expressed as β_{cr} . Considering the apparent stress-strain relationship of RC tensile members, β_{cr} is expressed as follows:

$$\beta_{cr} = 1 + k_1 k_2 \frac{A_c}{A_s} \frac{f_t}{E_s \epsilon_s^{ave}} \left(= \frac{\epsilon_s^{cr}}{\epsilon_s^{ave}} \right) \quad (6)$$

Where A_c is the concrete cross-sectional area of the tensile member, A_s is the reinforcing bar cross-sectional area, and f_t is the tensile strength of concrete. k_1 is a coefficient which determines the tensile force sharing of concrete depending on the shape of the bond stress distribution, and k_2 is a coefficient determined from the ratio of the maximum tensile stress generated in concrete between cracks to the tensile strength of concrete. Many researchers have proposed a relational expression of $k_1 k_2$ in the simple tensile condition.

Figure 5 shows the relationship between β_{cr} and $k_1 k_2$ respectively and the average strain ϵ_s^{ave} . The figure indicates that β_{cr} shows a narrow range of values of about 1.05 to 1.20, when assuming a general RC member of A_c/A_s is from 10 to 20, and the average strain ϵ_s^{ave} during general use is 500 to 1000 μ . In other words, the variation in rebar stress due to the adhesion strength of cracked cross section during general use is about 10 to 20% at most. Because k_1 and k_2 decrease with repeated loading, β_{cr} can be assumed to be about 1.2 when not much time has passed after cracking occurred, and 1.1 when bond failure has progressed after sufficient time has passed.

β_H is calculated by $\beta_H = \beta_{H0} + \Delta\beta_{Hn} + \Delta\beta_{Hcr}$, where β_{H0} is the neutral axis position when all cross-sections are valid, ignoring non-structural members before cracks appear, $\Delta\beta_{Hn}$ is the amount of upward movement of the neutral axis position due to the influence of nonstructural members and $\Delta\beta_{Hcr}$ is the amount of upward movement of the neutral axis due to concrete crack.

$\Delta\beta_{Hn}$ is 0.1 for slab track and 0 for ballast track. $\Delta\beta_{Hcr}$ is 0.1 for cracked members and 0 for non-cracked members. β_{H0} is calculated by empirical relationship as $0.7-0.01L_b/H$ for slab girder and $0.9-0.016L_b/H$ for T-type girder. In actual maintenance, when cracks occur in the main girder of RC members, etc., β_H can be estimated from the crack height and reinforcing bar cover. When cracks occur in the main girder of RC members, β_H can be estimated from the crack height and reinforcing bar cover depth in actual maintenance situation.

The stress variation $\Delta\sigma_s^{cr}$ in the crack cross section is expressed by (7).

$$\Delta\sigma_s^{cr} = E_s \beta_{cr} \beta_H (\pi / L_b)^2 H \delta \quad (7)$$

3.2 Validation

To verify the validity of the proposed method for estimating reinforcing bar stress, the authors measured strain responses on an actual RC bridge by protruding reinforcing bars and attaching strain gauges. Deflection responses were measured by a ring-type displacement gauge near the strain measurement point at the same time. The number of measurement cases is about 10. Since the target bridge, of which dimensions $L_b = 8.7$ m, $H = 0.5$ m, consists of a slab girder and ballasted track, β_H was set to 0.63. $\Delta\beta_{Hcr}$ was set to 0.1

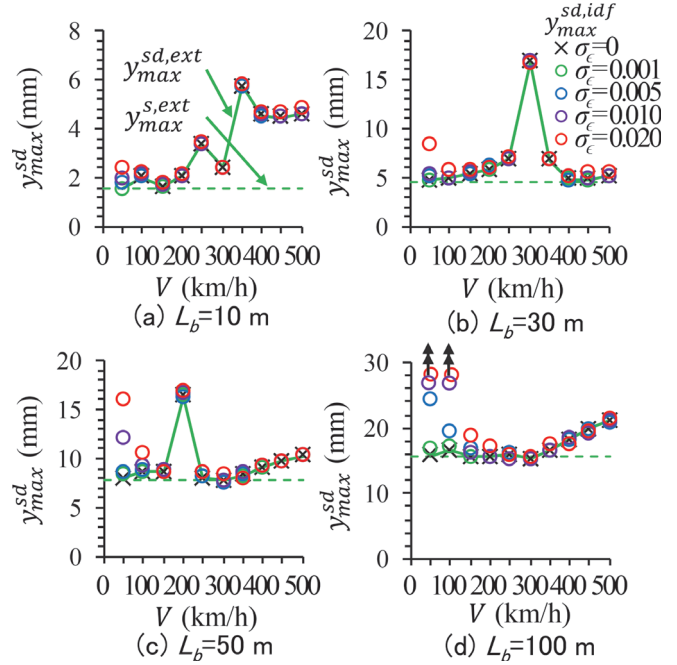


Fig. 4 Estimation accuracy of maximum value of dynamic displacement y_{max}^{sd} ($\sigma_\epsilon = 0.001 - 0.020$ m/s²)

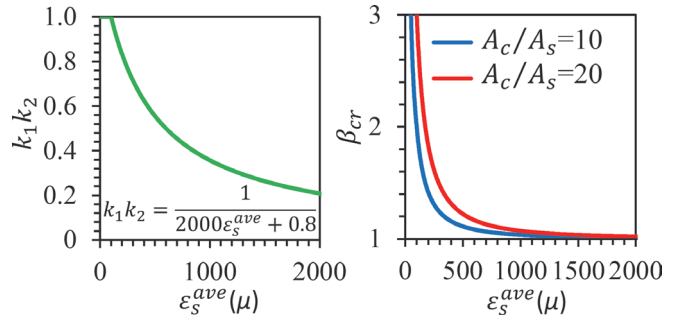


Fig. 5 Relationship between β_{cr} and $k_1 k_2$ and average strain ϵ_s^{ave}

because significant bending cracks were observed.

To verify the validity of the method for estimating reinforcing bar stress, strain responses were measured on an actual RC bridge by protruding reinforcing bars and attaching strain gauges. Deflection responses were measured by a ring-type displacement gauge near the strain measurement point at the same time. The number of measurement cases is about 10. Because the target bridge has $L_b = 8.7$ m, $H = 0.5$ m, of slab girder, and with ballasted track, β_H was set to 0.63 and $\Delta\beta_{Hcr}$ was set to 0.1 because significant bending cracks were observed.

Figure 6 shows the validity of the method for estimating reinforcing bar stress. It can be confirmed from the figure that the measured values and the estimated values are consistent with respect to the relationship between the reinforcing bar stress and the displacement at the center of span. The stress of the internal reinforcing bars is about 20 N/mm² for a displacement of about 3 mm. Then it can be confirmed that the measured stress waveform and the waveform calculated by the method using the displacement waveform multiplied by a scalar are in good agreement.

4. Application of deflection monitoring to actual bridge

4.1 Application target bridge

Figure 7 shows the specifications of the target bridge. The target bridge is a RC simple girder that individually supports the upper and lower lines of an actual Shinkansen line, with a bridge length of 9 m, a span length of 8.7 m, and a ballasted track. The girder height is 0.5 m, which is low relative to the span length, and results in a relatively large dynamic response. Monitoring data of about 13,000 cases on the up-line side obtained by MEMS acceleration sensors were investigated [2].

4.2 Result

Figure 8 shows the relationship between train speed and maximum acceleration, displacement and rebar stress obtained from monitoring data. It can be seen from the figure that maximum acceleration of 3.5 to 6 m/s² was recorded when the train speed V was in the range of 230 to 285 km/h. The maximum displacement is not proportional to the maximum acceleration and is about 3 to 4.5 mm. Because the acceleration and displacement are maximum due to the third resonance velocity at about 220 km/h, the natural frequency during train passage is about 7.3 Hz (about $42L_b^{-0.8}$). Even if the train speed is the same, there is a wide range in responses due to the different load amplitudes and vehicle types. In addition, small responses were observed in acceleration and maximum displacement when the vibration was transmitted when crossing the opposite line.

As described above, the proposed method can be applied to the acceleration data obtained by constant monitoring, and effective data can be analyzed by proposed method. Furthermore, using quantified structural performance can contribute to efficient maintenance management.

5. Conclusion

This study aimed to contribute to the maintenance of concrete girders using quantitative condition monitoring of structural performance such as fatigue failure and train running performance.

- A displacement waveform restoration method using the acceleration waveform during the passage of trains based on linear vibration theory was developed. Numerical experiments showed that the proposed method can estimate the maximum displacement with an accuracy of approximately 5% or less at a general SN ratio when the train speed is 150 km/h or more. The proposed method utilizes measured data around bridge natural frequency, where the effects of the dynamic characteristics of the bridge appear significantly, and replaces only the low-frequency region, which is susceptible to noise integration errors, with a theoretical solution. The proposed method can accurately reproduce not only the maximum value but also the waveform shape.
- In order to obtain a method for estimating rebar stress wave forms using displacement wave forms, an extension of equivalent linearized beam theory was developed to take into account the increase in rebar stress due to concrete bending cracking and the distance between the neutral axis and the rebar. The proposed method can estimate the stress waveform of reinforcing bars without detailed cross-sectional calculations, so that it can provide the stress amplitude and number of repetitions necessary for evaluating fatigue of the reinforcing bars.
- A series of developed methods make it possible to estimate the

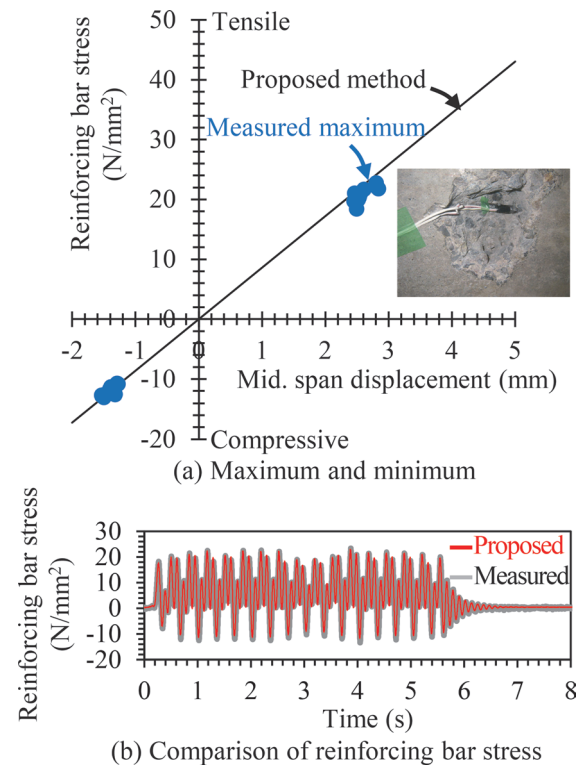


Fig. 6 Validity of method for estimating reinforcing bar stress

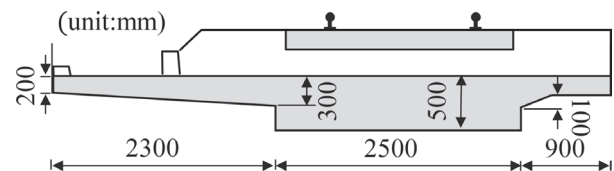


Fig. 7 Specifications of target bridge

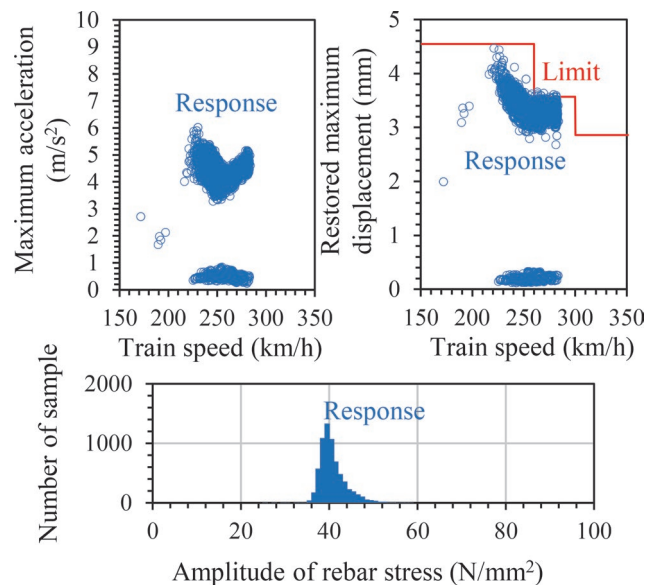


Fig. 8 Relationship between train speed and acceleration, displacement, and rebar stress

deflection of the bridge and the stress of the reinforcing bars on the underside of the girder from simple acceleration measurements. These methods allow high-speed calculations which need less than 1 second to process monitoring data in real time. By combining these methods with simple acceleration monitoring, it is possible to quantitatively monitor structural performance such as fatigue failure and train running performance without labor.

References

- [1] Railway Technical Research Institute, *Design Standards for Railway Structures and Commentary (Concrete Structures)*, Maruzen Co., Ltd., Tokyo, 2004 (in Japanese).
- [2] Ito, Y., Oono, Y., Yoshida, K., Nishiyama, S. and Tanabe, A.,

- “Proposal of simple health index for double reinforced RC slab girder railway bridges,” *Journal of Structural Engineering*, 63A, pp. 876-887, 2017 (in Japanese).
- [3] Tokunaga, M. and Ikeda, M., “Reproduction Analysis of Dynamic Response Increase due to Crack Propagation Caused by Simultaneous Loading of Multiple Lines of Railway PRC Girder,” *Journal of Japan Society of Civil Engineers*, Ser. A2 (Applied Mechanics (AM)), 77(2), I_467-I_476, 2021 (in Japanese).
- [4] Tokunaga, M., Ikeda, M. and Yoshida, K., “Displacement Response Waveform Restoration of Simply Support Bridge during Train Passage Based on Measurement Acceleration Integration,” *Journal of Japan Society of Civil Engineers*, Ser. A1 (Structural Engineering & Earthquake Engineering (SE/EE)), 78(1), 47-60, 2022 (in Japanese).

Authors



Munemasa TOKUNAGA, Ph.D.
Senior Researcher of Structural Mechanics
Laboratory, Railway Dynamics Division
Research Areas: Bridge Mechanics, Seismic
Design, Bridge Vehicle Interaction



Manabu IKEDA, Ph.D.
Senior Chief Researcher, Head of Structural
Mechanics Laboratory, Railway Dynamics
Division
Research Areas: Bridge Design, Steel and
Hybrid Structure

Development of Simulator to Accurately Reproduce Snow Accretion Phenomenon for Railway Vehicles Traveling in Snowy Areas

Kohei MUROTANI Koji NAKADE
Computational Mechanics Laboratory, Railway Dynamics Division

Yasushi KAMATA
Meteorological Disaster Prevention Laboratory, Disaster Prevention Technology Division

When accreted snow drops off train bogies, it can damage railway ground facilities along tracks, train devices, etc. As a countermeasure against such snow accretion damage, we have developed a snow accretion analysis method to understand the snow accretion process. The “snow accretion analysis method” developed in this research consists of an “airflow calculation,” a “trajectory calculation” and a “snow accretion calculation.” In this research, we performed two kinds of snowfall wind tunnels to validate the proposed simulator.

Keyword: snow accretion analysis method, snow accretion for a train bogie, two-way coupling analysis

1. Introduction

Snow accretion damage in the railway field is diverse, including current collection failure due to snow accretion on electric wires and pantographs, damage to ground structures and ballast scattering due to the falling of snow accretion from vehicles (Fig. 1), and transportation damage due to fallen trees and fallen bamboo along the train line. Among these, the falling of snow accretion from vehicles is a serious problem because it causes delays and equipment damage due to unswitched turnouts. High-speed railways mitigate snow accretion on vehicles by smoothing underfloor equipment and reduce snow accretion groundside by removing snow in stations. However, snow accretion occurs on the vehicle bogie, which has a complicated shape and is difficult to cover for maintenance purposes. Lumps of snow may have a hardness close to ice, and if they fall due to vibration as the vehicle is traveling or cause impact when passing a track turnout, the ballast of the track will be scattered and it may damage railway vehicles, ground facilities and houses along the railway line.

In this study, we developed a snow accretion simulator that can reproduce the snow accretion phenomenon on a railway vehicle in order to study what kind of railway vehicle shape can reduce snow accretion. Reproducing snow accretion under a railway vehicle requires reproducing flow with flying snow and complex undercarriage shapes. Therefore, it is not possible to reproduce phenomena accurately with a computational model that has limited conditions or a simple shape. At the same time, simplification of both the shape of elements on which snow accretion occurs (accretion target) and of the airflow analysis should be avoided. This is because it is important to accurately reproduce the shape of snow accretion in order to estimate the position and amount of accreted snow, since airflow alters as snow accretion occurs.

In this study, we developed a snow accretion analysis method based on the airflow around a railway vehicle, motion of the flying snow particles moving within this airflow, and the snow accretion condition to the railway vehicle [1, 2]. In this report, we describe the developed snow accretion analysis method and also describe the results of validating the calculation through comparison with the results of a snow accretion experiment using a snowfall wind tunnel.



Fig. 1 Railway vehicle bogie with snow accretion

2. Experiments for snow accretion simulator development

We at the Shinjo Cryospheric Environment Laboratory of the National Research Institute for Earth Science and Disaster Prevention conducted snow accretion experiments on a cube-shape model and railway vehicle model as basic shapes using artificial dry snow with dendrite crystals, with the aim of obtaining basic data for developing a snow accretion simulator. The details of the snow accretion experiment using the cube-shape model in this section are described in Kamata et al. [1].

2.1 Method for measuring drag coefficient of flying snow

Measuring the drag coefficient of flying snow particles is necessary because flying snow particles move in the air under the drag force of the airflow. Since the shape of flying snow particles is complicated, it is difficult to estimate the drag coefficient from the shape. Therefore, in order to obtain the drag coefficient of flying snow that is floating in the snowfall wind tunnel, we supplied snow under the conditions of -2°C air temperature and 2.5 m/s inflow wind speed, and a sheet laser was irradiated from the ceiling in order to photo-

graph the falling trajectory of the flying snow from the side of the wind tunnel. The drag coefficient was obtained by solving the equation of motion for gravity and drag with the drag coefficient of the flying snow as a parameter, and using the falling angle of the flying snow in the captured image.

2.2 Snow accretion experiment method for a cube-shape model

A snow accretion experiment was conducted using a cube-shape model with a side length of 152 mm as a basic shape. Figure 2 shows the overview and state of the snow accretion experiment of the cube-shape model. A cube-shape model was placed in the center of the wind tunnel, and a snow accretion experiment was conducted under the conditions of -2°C air temperature and 2.5 m/s inflow wind speed. Snow was supplied into the wind tunnel using a ceiling snowfall device that consisted of a sieve and a vibrating motor installed on the ceiling. A snow accretion experiment was conducted on a cube-shape model by supplying snow under a constant inflow wind speed, and the snow accretion shape was measured.

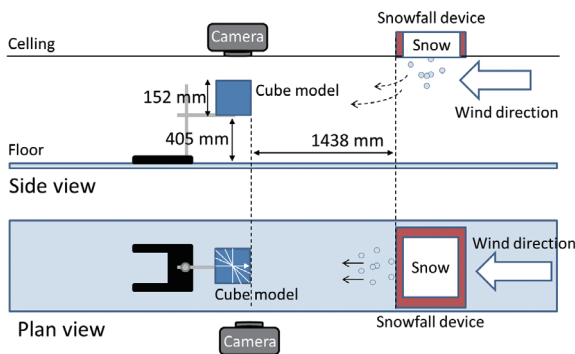


Fig. 2 Snow accretion experiment on cube-shape model

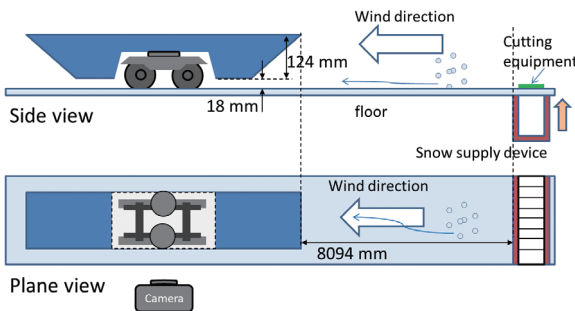


Fig. 3 Snow accretion experiment on railway vehicle model

2.3 Snow accretion experiment method of railway vehicle model

We conducted snow accretion experiments on a stationary railway vehicle model in order to validate the snow accretion calculation algorithm in a complex airflow field such as a railway vehicle bogie. Figure 3 shows the overview and state of the snow accretion experiment of the railway vehicle model. As shown in Fig. 3, a model in which an upper frame is attached to a 1/10 scale train bogie model is called the railway vehicle model. The snow was supplied into the wind tunnel using a snow supply device, which was installed on the floor of the wind tunnel and consisted of a snow storage unit and cutting equipment. In this experiment, the air tempera-

ture was set to -2°C , and snow was supplied into the wind tunnel with the inflow wind speed of 10 m/s. After snow accretion, we measured snow accretion distribution, snow accretion elongation amount, and snow accretion weight around the railway bogie.

3. Snow accretion analysis method

3.1 Snow accretion analysis method by two-way coupling

The snow accretion analysis method developed in this study [2] is a method that conducts a two-way coupling of airflow calculation and snow accretion calculation, as shown in Fig. 4. In this study, we called the calculation for the airflow field “airflow calculation,” the calculation of the drag force from the velocity distribution of the airflow field and finding of the trajectory of the flying snow particles “trajectory calculation,” and the condition of whether snow accretion on the target occurs “snow accretion calculation.” The analysis that couples all of these was called “snow accretion analysis.”

The snow accretion analysis method that was developed in this study was implemented according to the procedure shown in Fig. 4. First, airflow calculation was conducted using the airflow simulator. Next, the trajectory of the flying snow particles was calculated by modeling the snow as a spherical shape and using the velocity distribution of the airflow and the equation of motion for gravity and drag. Afterwards, the snow accretion calculation was done using the particle simulator. The shape of the target changed by the shape of the snow accretion was reflected in the boundary shape of the airflow simulator. In this way, in the snow accretion analysis method of this study, the airflow calculation influences the snow accretion calculation by the trajectory of the flying snow particles, and the snow accretion calculation influences the airflow calculation by changing the boundary shape, resulting in a two-way coupled analysis. Additionally, the effect on the airflow field that is caused by the presence of flying snow particles in the air needs to be considered, but since this was not observed in the snowfall wind tunnel experiment, this effect was not taken into consideration in the present method.

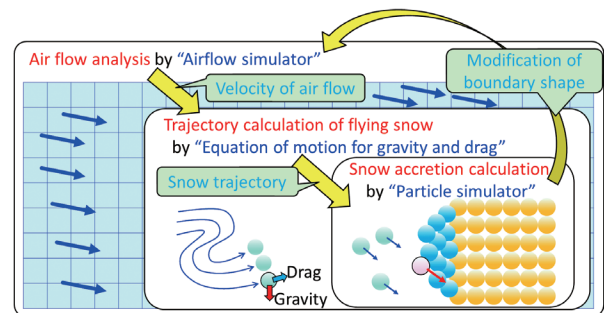


Fig. 4 Overview of snow accretion analysis method

3.2 Airflow calculation

The software used for airflow calculation was an airflow simulator that employs a finite difference method for a nonuniform orthogonal grid developed by the Railway Technical Research Institute (RTRI). The basic equation is the Navier-Stokes equation for incompressible fluids. Turbulent flow analysis is conducted by large eddy simulation, and the coherent structure Smagorinsky model is used as the sub-grid scale model. The velocity and pressure were

coupled using the fractional step method. The third-order Adams-Bashforth method was used for time steps, and the second-order central difference method was used for spatial differences. An inflow wind boundary condition was set on the inflow surface, convective outflow boundary condition was set on the outflow surface, slip velocity boundary condition was applied to the top and side surfaces, and no-slip velocity boundary condition was applied to the surface of the snow accretion target and bottom surface of the computational domain. The representation of the target shape on the orthogonal grid was the voxel method, which discriminates between fluid and solid in computational grid units.

The vertical distribution $u(z)$ of the inflow wind speed was set as follows based on the results measured from the wind tunnel,

$$u(z) = \begin{cases} U \times \left(\frac{z}{0.3}\right)^{1/7} & (z \leq 0.3) \\ U & (z > 0.3) \end{cases} \quad (1)$$

where the inflow wind speed U (m/s) of the wind tunnel, boundary layer thickness 0.3 m, and 1/7 power law from the inflow surface were used, and where z is the height from the wind tunnel floor.

3.3 Trajectory calculation

In this study, we approximate snow as spherical particles and call them snow particles. Snow particles floating in air are called flying snow particles, and the trajectory calculation was conducted for each flying snow particle. The external force acting on the flying snow particles was assumed to be the drag force obtained from the gravity and velocity distribution in the airflow calculation, and collisions between flying snow particles were not considered.

For trajectory calculation, the equation of motion for drag and gravity,

$$\frac{d\vec{U}_{\text{snow}}}{dt} = \frac{3}{4} C_d \frac{\rho_{\text{air}}}{\rho_{\text{snow}}} \frac{1}{d_{\text{snow}}} \vec{U}_r \|\vec{U}_r\| + \vec{g} \quad (2)$$

was used, where \vec{U}_{snow} is the velocity of the flying snow particle, \vec{U}_r is the relative velocity of the flying snow particle with respect to the airflow field, d_{snow} is the diameter of the flying snow particle, ρ_{air} and ρ_{snow} are the density of air and flying snow, C_d is the drag coefficient of the flying snow, and \vec{g} is the gravitational acceleration. For the density of air, the value of 1.3 kg/m³, which is the density at 0°C, was used. The density of the flying snow was set as 100 kg/m³, of the state in which the dendrite crystals generated by the snowfall wind tunnel pile up. The diameter of the flying snow particles was set to 1 mm, which is approximately half the length of the snow crystal dendrite (2 mm). In the snowfall wind tunnel experiment described in Section 2.1, the falling angle of flying snow was 22° at an inflow wind speed of 2.5 m/s. Hence, the drag coefficient of flying snow obtained by solving the equation (2) of motion for gravity and drag was set to 1.04 so that the falling angle of flying snow would be the same.

3.4 Snow accretion calculation

The software used for snow accretion calculation in this study was a particle simulator developed by RTRI. It is important in the snow accretion calculation to determine the snow accretion of flying snow particles. Regarding this point, the analysis of the snow accretion experiment of the cube-shape model by Kamata et al. [2] showed that “if the snow accretion surface direction speed was smaller than a certain value that does not depend on the wind speed,

then snow accretion occurs; and if it is larger, then snow accretion does not occur.”

Therefore, in this study, we incorporated these experimental results and developed a snow accretion calculation algorithm that is composed of two snow accretion conditions shown in Fig. 5. The wall particles in Fig. 5 are the particles that form the shape of the analysis model. Here, the shape of a model such as a railway vehicle is composed of wall particles. A snow accretion particle is a particle whose motion has stopped due to snow accretion of a flying snow particle to a wall particle.

The first snow accretion condition of the snow accretion calculation algorithm is the snow accretion condition based on the space filling rate of the snow accretion particles shown in Fig. 5(a). This snow accretion condition states that snow accretion does not occur unless there are a sufficiently large number of snow accretion particles or wall particles around the flying snow particles.

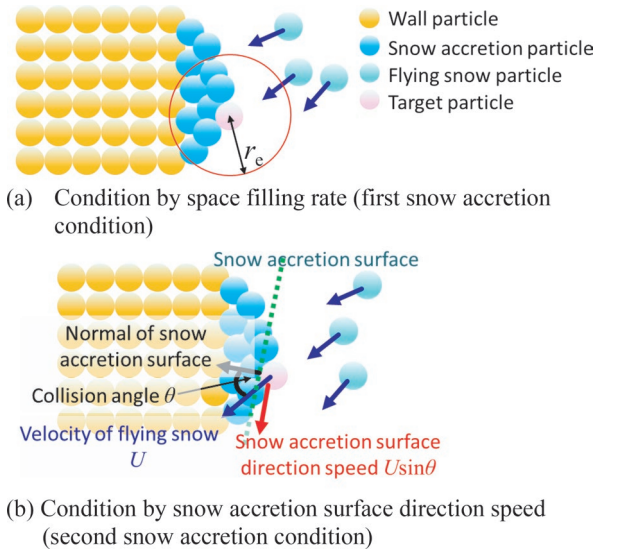


Fig. 5 Two snow accretion conditions

First, let the particle number density of particle i be

$$n_i = \sum_{j \neq i} w(\|\vec{r}_{ij}\|) \quad (3)$$

$$w(\|\vec{r}_{ij}\|) = \begin{cases} \left(\frac{\|\vec{r}_{ij}\|}{r_c} - 1\right)^2 & (0 \leq \|\vec{r}_{ij}\| \leq r_c) \\ 0 & (r_c < \|\vec{r}_{ij}\|) \end{cases} \quad (4)$$

where $w(\cdot)$ is the weighting function, \vec{r}_i is the position of particle i , and \vec{r}_{ij} is the relative position of particles i and j . Additionally, r_c is the influence radius of the weighting function and is defined as $r_c = c_0 \times l_0$ using the particle diameter l_0 and coefficient c_0 , with $c_0 = 3.1$. In the snow accretion condition, the standard particle number density when the particles are arranged in a lattice is n^0 , and if the space filling rate n_i/n^0 of the particles is greater than the snow accretion packing constant α ,

$$\frac{n_i}{n^0} > \alpha \quad (5)$$

then the flying snow particle becomes a snow accretion candidate particle and has satisfied the first snow accretion condition. In this study, $\alpha = 0.65$ because it was only necessary to determine whether the particles adhered to the surface.

The second snow accretion condition is based on the snow accretion surface direction speed shown in Fig. 5(b). First, the normal of the snow accretion target of particle i for which snow accretion condition is conducted is defined as

$$\vec{m}_i = \sum_{j \neq i} \frac{\vec{r}_{ij}^*}{\|\vec{r}_{ij}^*\|^2} w(\|\vec{r}_{ij}^*\|). \quad (6)$$

If the speed of the snow accretion candidate particle is set as the normal direction of the snow accretion target, then the angle between \vec{U}_i and \vec{m}_i becomes

$$\theta_i = \arccos\left(\frac{\vec{U}_i \cdot \vec{m}_i}{\|\vec{U}_i\| \|\vec{m}_i\|}\right) \quad (7)$$

and this angle is called the collision angle θ_i .

If the snow accretion surface direction speed $\|\vec{U}_i\| \sin\theta_i$ is smaller than the β of the snow accretion surface direction speed where the snow accretion does not grow any further,

$$\|\vec{U}_i\| \sin\theta_i < \beta \quad (8)$$

then the flying snow particle has satisfied the second snow accretion condition. In this study, $\beta = 2.0$ m/s, which is close to the value obtained from the snow accretion experiment by Kamata et al. [1].

A flying snow particle becomes a snow accretion particle if it satisfies Eq. (5) for the first snow accretion condition and Eq. (8) for the second snow accretion condition. When the first snow accretion condition is satisfied but not the second, then the flying snow particle will be near the snow accretion surface, but the snow accretion surface direction speed will be large and not result in snow accretion. In this case, it is assumed that the flying snow particle rebounds on the snow accretion surface by inelastic collision. In other cases, the state of the snow particles will not change. The coefficient of restitution for the flying snow particles was set to that of ice, which is 0.8.

4. Validation of snow accretion analysis of a cube-shape model

In this section, we conducted a snow accretion analysis that reproduces the snow accretion experiment using the cube-shape model in the snowfall wind tunnel as shown in Fig. 6 in order to validate the snow accretion analysis method. The physical property values used in the snow accretion analysis conducted in this section are an inflow wind speed of 2.5 m/s, air density of 1.3 kg/m³, and flying snow density of 100 kg/m³. The flying snow particle diameter was set as having a value generated by normal random numbers with an average of 1 mm and standard deviation of 0.2 mm, and the drag coefficient of flying snow was set to a value generated by normal random numbers with an average of 1.04 and standard deviation of 0.2.

The grid used for airflow calculation was a non-equidistant grid with a minimum grid spacing of 4 mm, 275 grids in the x direction, 125 grids in the y direction, and 125 grids in the z direction, with 4,296,875 grid points. In the trajectory calculation, we used flying snow particles with a diameter of 1 mm, which is the physical property value of actual flying snow; however, since the snow accretion calculation is computationally expensive, coarse-graining was conducted in which 4³ 1-mm flying snow particles were moving together. Therefore, contact judgment in the snow accretion calculation was conducted with coarse-grained particles with a diameter of 4 mm. Henceforth, in this section, “coarse-grained particles” are simply referred to as “particles.”

The number of flying snow particles generated in the snow ac-

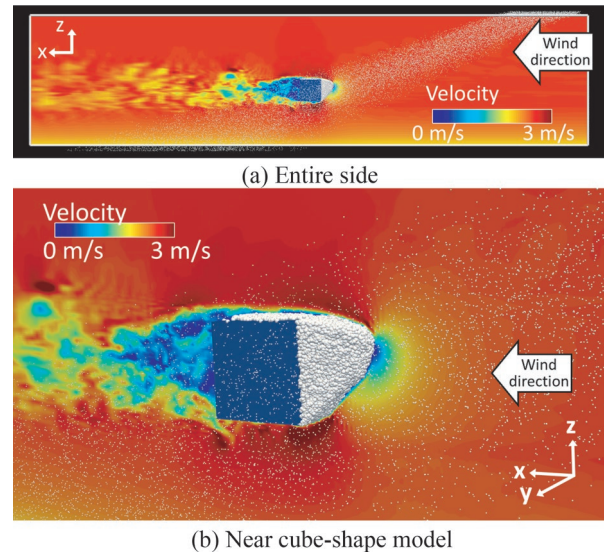


Fig. 6 Snow accretion analysis of a cube-shape model

cretion analysis is purposefully set larger than the amount of flying snow supplied from the snowfall equipment in the snow accretion experiment. This is because although the snow accretion experiment takes 30 minutes to grow the snow accretion, it is difficult to conduct such a long-term analysis in terms of computational cost. Therefore, the maximum number of flying snow particles is generated without breaking the analysis. For this reason, the elapsed time does not match between the snow accretion experiment and snow accretion analysis; as such, some form of correspondence has to be made when comparing results.

It can be seen in Fig. 6(a) how the flying snow particles that are generated from the upper right undergo free fall and are then swept away by the airflow, resulting in snow accretion to the cube-shape model. It can be seen in Fig. 6(b) that the velocity of the airflow field at the snow accretion tip portion is small. In this analysis, the calculation time interval was set to 0.0004 s for the airflow calculation and 0.00016 s for the snow accretion calculation, and 60,000 steps were conducted for the snow accretion calculation. Analyses were done with a total of approximately 80,000 particles.

Figure 7 shows the results of the snow accretion experiment and snow accretion analysis of the cube-shape model. The yellow dashed line of the snow accretion analysis is the shape of the snow accretion in the snow accretion experiment. It can be confirmed as a result of comparing these that the snow accretion shape is generally reproduced.

Figure 8 shows the results of a comparison of changes in the snow accretion tip between experiments and analyses. Figure 8 shows changes in the snow accretion tip between experiments and analyses. The relationship between the snow accretion elongation amount and tip height between the snow accretion experiments and analyses was generally consistent. Therefore, the state in the snow accretion experiment, where the snow accretion tip increases in height while the snow accretion elongation amount increases as snow accretion progresses due to the flying snow coming from above, is also reproduced in the snow accretion analysis. Here, it is thought that the snow accretion analysis had a slightly higher tip position due to the tilting of the cube-shape model forward and downward in the snow accretion experiment.

Figure 8 can be used to associate the elapsed time of the snow accretion experiment with the number of steps of the snow accretion

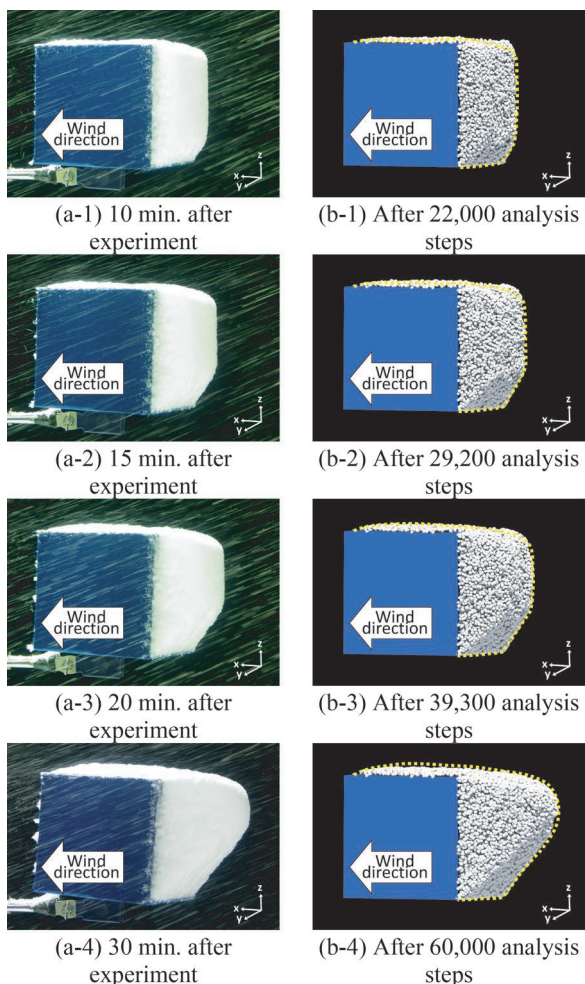


Fig. 7 Snow accretion experiment and snow accretion analysis of cube-shape model

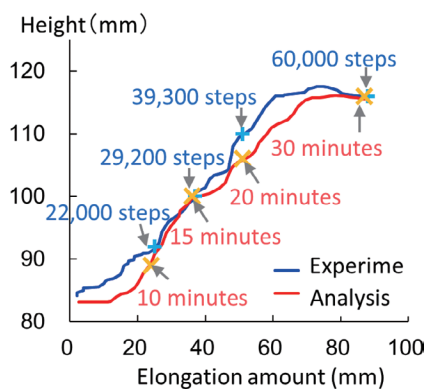
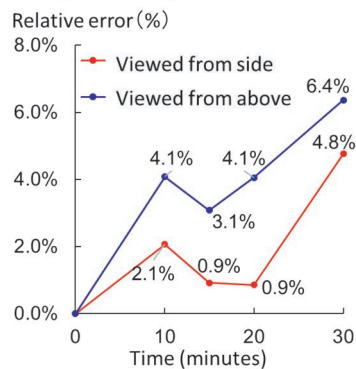


Fig. 8 Comparison of changes in tip of snow accretion in snow accretion experiment and snow accretion analysis

analysis. Therefore, we used Fig. 8 to correlate the elapsed time of the snow accretion experiment with the number of steps in the snow accretion analysis. Specifically, we found the analysis result of the snow accretion elongation amount that was as close as possible to the experimental values after 10, 15, 20, and 30 minutes in Fig. 8, and the number of steps in the analysis was associated with each experimental value. The “After ○ analysis steps” in Fig. 7 refers to

	Viewed from side	Viewed from above
Experiment		
Analysis		
Experiment and analysis		

(a) Obtaining relative error



(b) Changes in relative error

Fig. 9 Relative error of snow accretion analysis in projected area of snow accretion experiment

the number of analysis steps associated with the elapsed time of the experiment using this method.

Figure 9(a) shows how to obtain the relative error of the snow accretion analysis in the projected area of the snow accretion experiment, and Fig. 9(b) shows the changes in relative error. In the snow accretion experiment, the “Experiment” in Fig. 9(a) is the photographed result. The projection of the result in the snow accretion analysis onto the projection plane that matches the cube-shape model is the “Analysis” in Fig. 9(a). Figure 9(b) shows the result of the relative error based on the snow accretion experiment. In Fig. 9(b), the horizontal axis is the elapsed time of the snow accretion experiment, and a correspondence with the snow accretion analysis was made using Fig. 9(b). It can be confirmed with the analysis of the images taken from above and the side that the snow accretion analysis reproduces the snow accretion experiment with a relative error of approximately 6% of the projected area.

5. Snow accretion analysis of railway vehicle model

In this section, we conducted a snow accretion analysis that reproduced a snow accretion experiment of a railway vehicle model in order to validate the snow accretion calculation algorithm in a complex airflow field such as a railway vehicle bogie. A vertical cover model (Fig. 10(a) and Fig. 10(c)) and tilting cover model (Fig. 10(b) and Fig. 10(d)) were used in order to investigate whether the snow accretion distribution and amount of snow accretion in the experiment could be reproduced by analysis even if the cover shape changed.

The physical property values used in the snow accretion analy-

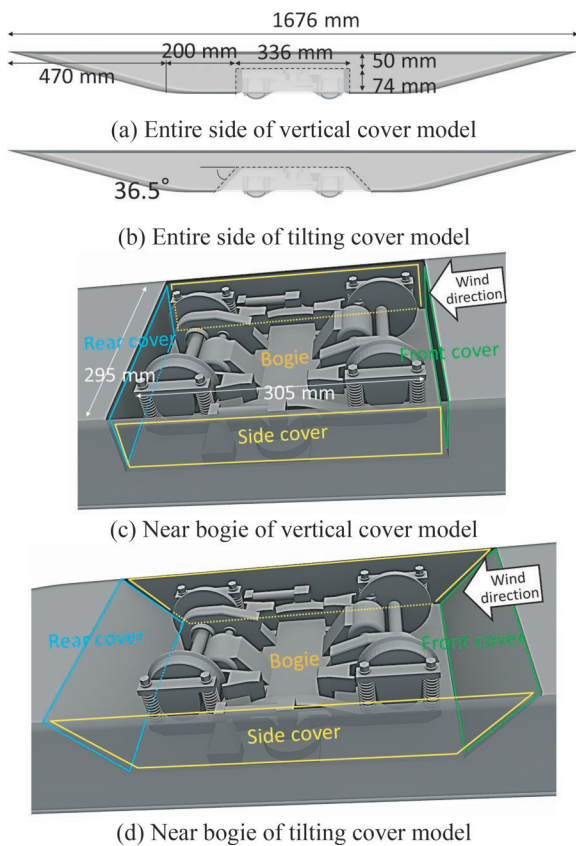


Fig. 10 Railway vehicle model

sis were an inflow wind speed of 10.0 m/s, air density of 1.3 kg/m³, and flying snow density of 100 kg/m³. The diameter of the flying snow particles was set to a value generated by normal random numbers with an average of 1 mm and standard deviation of 0.4 mm, and the flying snow drag coefficient was set to a value generated by normal random numbers with an average of 1.04 and standard deviation of 0.2. The standard deviation of the diameter of the flying snow particles was set to be larger than that of the cube-shape model given that the flying snow particles collide with the snow surface and break apart.

The grid used for airflow calculation was a nonuniform grid with a minimum grid spacing of 2 mm, 855 grids in the *x* direction, 220 grids in the *y* direction, and 125 grids in the *z* direction, with 23,512,500 grid points. Snow accretion calculations were conducted using coarse-grained particles with a diameter of 2 mm.

For the generation of flying snow particles, 408 flying snow particles were placed in a grid pattern at intervals of 10 mm (1 in the direction of the wind channel, 34 in the width direction, and 12 in the height direction), and the position of the flying snow particles was randomized using uniform random numbers within 20 mm intervals. Flying snow particles were regenerated at intervals of 0.001 s because they were flowed into the wind tunnel. In this case as well,

the amount of flying snow generated in the snow accretion analysis was intentionally greater than the amount of flying snow supplied from the snowfall device in the snow accretion experiment.

The calculation time intervals were set as 0.0002 s for the airflow calculation and 0.00004 s for the snow accretion calculation, and the snow accretion calculation was conducted with 3 million steps. The total number of particles analyzed was approximately 5.5 million particles.

Figure 11 shows an overview of the snow accretion analysis of the railway vehicle model. Large white spheres attached near the bogie are the snow accretion particles, small white dots floating in air are the flying snow particles, lines are streamlines, and colors are the velocity magnitudes. Streamline seeds were placed at both ends and the center of the rear cover, which were sites with large amounts of snow accretion. It can be confirmed from the streamline that the snow flying behind the vehicle was caused by turbulence in the airflow.

Figure 12(a-1) and Fig. 12(a-2) are the results after 10 minutes of the snow accretion experiment, and Fig. 12(b-1) and Fig. 12(b-2) are the results after 3 million snow accretion analysis steps. The white spheres in Fig. 12(b-1) and Fig. 12(b-2) are the snow accretion particles. When focusing on the snow accretion distribution within the red dashed line where a large amount of snow accretion occurs in order to investigate the changes in the snow accretion distribution when the cover was changed, it can be confirmed that the experiments were similar to the analyses.

Figure 13 shows the results of snow accretion analysis after 3 million steps of a snow accretion analysis of a vehicle model simulating a snowfall wind tunnel experiment with streamlines added. The white spheres attached near the bogie are the snow accretion particles, the lines are streamlines, and the colors are the magnitudes of the velocity. Streamline seeds were placed at both ends and the center of the rear cover, which were sites with large amounts of snow accretion. In Fig. 13, the snow accretion occurs in the front of the wheels because the wheels are stationary. The generation of streamlines as it weaves between the devices at the bottom of the bogie can be seen. It can be seen in the vertical cover model that the flow entering from near the front cover stagnates near the rear cover, resulting in a large amount of snow accretion. It can be seen in the tilting cover model that most of the flow coming in from near the front cover hits the rear cover and flows out near the rear cover without stagnating. It can be seen in the vertical cover model that the flow is slow and stagnant near the bogie, which facilitated snow accretion. However, in the tilting cover model, the flow was fast near the rear cover, which made snow accretion difficult.

Figure 14 shows the results of comparing the snow accretion elongation amount in the cover snow accretion analysis and experiment. The snow accretion experiment was the result of measurements after 10 minutes, and the snow accretion elongation amount was 17 mm for the vertical cover model and 5 mm for the tilting cover model. In the snow accretion analysis, the snow accretion elongation amount after 3 million steps was 18.13 mm for the vertical cover model and 5.25 mm for the tilting cover model. It can be

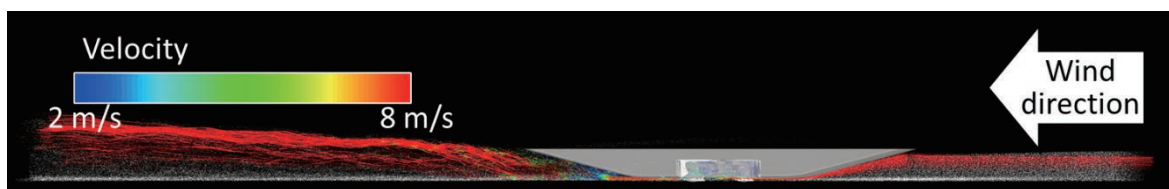


Fig. 11 Snow accretion analysis of railway vehicle model (entire side)

seen that the result after 3 million steps of snow accretion analysis is close to the result after 10 minutes of snow accretion experiment. When comparing snow accretion suppression effect due to differences in the cover between the snow accretion experiment and snow accretion analysis, it can be seen that the snow accretion elongation amount decreased by 70% and 71% in the snow accretion experiment and analysis, respectively, showing good agreement between the two. This indicates that the change in snow accretion elongation

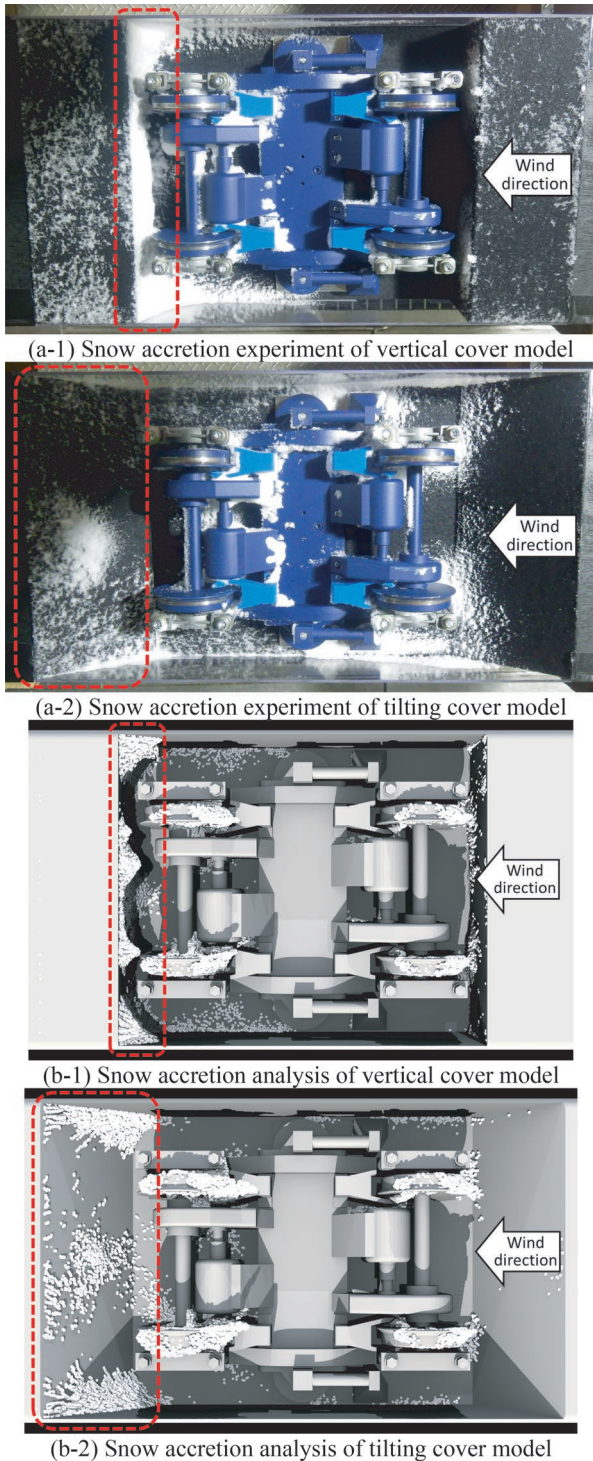


Fig. 12 Snow accretion experiment and snow accretion analysis of railway vehicle model

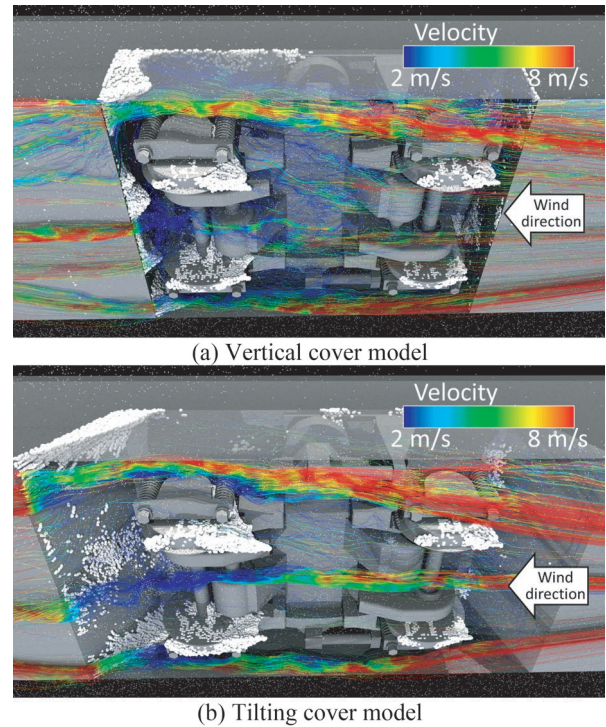


Fig. 13 Snow accretion analysis of railway vehicle model

amount due to the change in shape of the cover that was implemented in the snow accretion experiment could also be reproduced in the snow accretion analysis.

Figure 15 shows the results of comparing the snow accretion volume of analysis and the snow accretion weight of the experiment regarding snow accretion in the cover. The snow accretion volume is calculated from the number of snow accretion particles. Since the snow accretion weight is obtained by multiplying the snow accretion volume by a constant density, the two values are comparable. The snow accretion experiment was the result of measurements after 10 minutes, and the snow accretion weights were 22.4 g in the vertical cover model and 11.1 g in the tilting cover model. In the snow accretion analysis, the snow accretion volumes after 3 million steps were 117.4 cm³ for the vertical cover model and 65.0 cm³ for the tilting cover model. Assuming that the results after 3 million steps of snow accretion analysis were close to the results after 10 minutes of snow accretion experiment, the snow accretion suppression effect of the snow accretion experiment was a 50% decrease in snow accretion, and the snow accretion suppression effect in the snow accretion analysis was a 45% decrease in the snow accretion

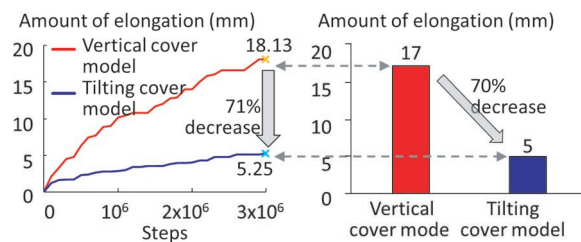


Fig. 14 Snow accretion elongation amount in cover snow accretion analysis and experiment

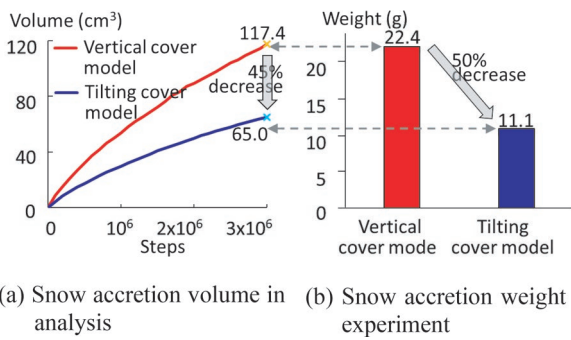


Fig. 15 Snow accretion in cover snow accretion analysis and experiment

suppression effect. As such, the results showed good consistency between the two. This indicates that the change in the snow accretion amount due to the shape change of the cover that was implemented in the snow accretion experiment could also be reproduced in the snow accretion analysis. Figure 14 shows the changes in the snow accretion amount at sites where snow accretion was most pronounced, and Fig. 15 shows changes in the overall amount of snow accretion. It was confirmed from the above that the snow accretion analysis of the railway vehicle model reproduced the snow accretion experiment well.

6. Conclusion

In this study, we developed a snow accretion analysis method that can reproduce the growth of snow accretion with the aim of developing a railway vehicle shape where snow accretion is difficult. The snow accretion analysis method under development is a combination of airflow calculation, trajectory calculation, and snow accretion calculation, and the temporal changes in snow accretion shape and snow accretion volume can be calculated.

We validated the snow accretion analysis method by comparing the results of two types of snow accretion experiments using the

snowfall wind tunnel. First, it was confirmed in the snow accretion experiment on the cube-shape model that the snow accretion analysis reproduced the projected area of the snow accretion in the snow accretion experiment with a relative error of approximately 6%. Next, we compared the snow accretion suppression effect due to differences in covers with those in the snow accretion experiment for the railway vehicle model, which has a complex airflow field. The results showed that the changes in snow accretion elongation caused by changing the cover shape in the snow accretion experiment could be reproduced in the snow accretion analysis. Furthermore, it became possible to consider the reasons why snow accretion elongation and snow accretion were smaller in the tilting cover model than in the vertical cover model in the snow accretion experiment using the snow accretion analysis.

Acknowledgments

In this research, we used computational resources of the K computer provided by the RIKEN Advanced Institute for Computational Science and the FX100 provided by the Nagoya university through the HPCI System Research project (Project ID: hp170067, hp180014).

References

- [1] Kamata, Y., Murotani, K., Nakade, K., Takahashi, D., Sato, K., and Nemoto, M., "Development of snow accretion simulator for railway vehicles (Part 1) —Examination of snow accretion development conditions by basic experiments—," *Seppyo*, Vol. 83, No. 1, pp. 79-96, 2021 (in Japanese).
- [2] Murotani, K., Nakade, K., and Kamata, Y., "Development of snow accretion simulator for railway vehicles (Part 2) —Validation of snow accretion method using snow accretion development conditions by experiment—," *Seppyo*, Vol. 83, No. 5, pp. 465-487, 2021 (in Japanese).

Authors



Kohei Murotani, Ph.D.
Senior Researcher, Computational Mechanics Laboratory, Railway Dynamics Division
Research Areas: Computational Mechanics



Yasushi Kamata, Ph.D.
Senior Chief Researcher, Head of Meteorological Disaster Prevention Laboratory, Disaster Prevention Technology Division
Research Areas: Snow Disaster Prevention



Koji Nakade, Ph.D.
Senior Chief Researcher, Head of Computational Mechanics Laboratory, Railway Dynamics Division
Research Areas: Fluid Mechanics, Computational Fluid Dynamics

Measures Against Snow Accretion Around Shinkansen Bogies Using Running Wind

Hajime TAKAMI

Yuto ARAKI

Vehicle Aerodynamics Laboratory, Environmental Engineering Division

Kohei MUROTANI

Hidenori ISHII

Computational Mechanics Laboratory, Railway Dynamics Division

Yasushi KAMATA

Meteorological Disaster Prevention Laboratory, Disaster Prevention Technology Division

In this study, we investigated measures against snow accretion on bogies of high-speed trains by utilizing high-speed air flow through inlets on the sides of trains. The effectiveness of this method was confirmed through model experiments and numerical analysis. The results showed that this method is expected to reduce snow accumulation onto covering body panels at the rear of bogies by about half.

Key words: snow accretion, fluid dynamics, high-speed train, inlet, model experiment, CFD

1. Introduction

When frozen and hardened snow falls from Shinkansen trains traveling in snowy areas and flies at high speed, it can hit the ground equipment and vehicles, causing damage. Snow-melting operations are carried out at intermediate stations to prevent excessive snow accretion around bogies. However, since this snow-melting operation is time and labor intensive, it is not a valid measure when snow accretion occurs over short periods of time while trains are running.

Therefore, a new method for suppressing snow accretion on bogies by utilizing the high-speed air flow around vehicles was investigated. The effectiveness of this method was confirmed through model experiments and numerical analyses.

2. Measures against snow accretion using running wind

2.1 Snow particle movement on snow accretion

Figure 1 shows the motion of snow particles on a snow accretion surface [1]. When snow particles which have a larger mass than the air are floating in the flow, they cannot follow the flow near the wall, because the streamline bends sharply in front of the wall, so snow particles collide with the wall due to the large inertial effect.

In order to prevent snow particles from colliding and sticking to the wall, the inertial force of snow particles caused by tangential velocity, expressed by $v \sin \theta$, needs to exceed the snow adhesion force, expressed by F_a . The magnitude of the snow adhesion force varies depending on the temperature, snow quality, and wall surface condition. However, if the inertial force of snow particles by the tangential velocity is sufficiently high, snow accretion can be suppressed.

Therefore, a common measure is to slope the wall in the flow direction to decrease the impact angle and increase the tangential velocity of snow particles. When it is difficult to slope the wall due to constraints such as equipment configuration or easy maintenance, external force which forcibly changes the tangential velocity of snow particles is valid.

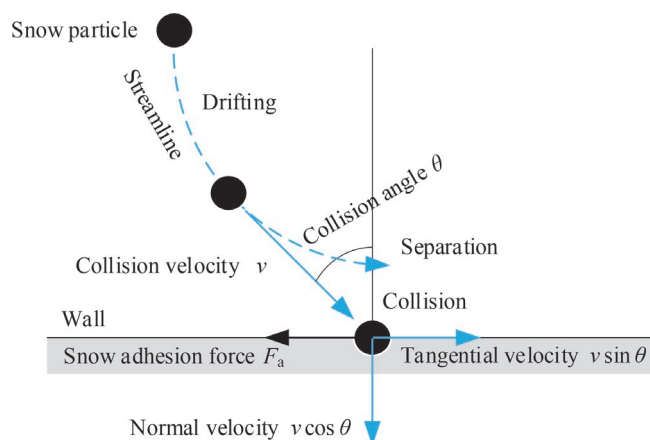


Fig. 1 Motion of snow particles

2.2 Application of intake and nozzle

As the external force which forcibly changes the tangential velocity of snow particles, we utilized the high-speed air flow around vehicles (running wind) without a power source. This measure consists of intakes that draw running wind from the sides of the bogie, and nozzles that blow the air from the outlets of the intakes to the wall downstream of the wheel (Fig. 2).

This measure is expected to change the angle of snow particle flows in front of the wall and makes the inertial force by the tangential velocity of the snow particles greater than the snow adhesion force.

3. Model experiments by moving model train facility

In order to investigate measures against snow accretion, we developed a new experimental apparatus that can run a model train (moving model train facility). This facility can simulate a series of phenomena: snow floating from the track surface as the train runs, and snow particles drifting in the flow around the train and adhering to the wall around the bogie.

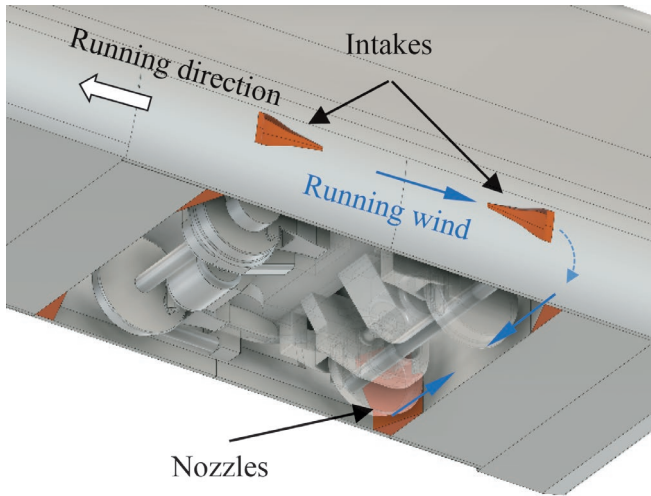


Fig. 2 Intake and nozzle layout

3.1 Schematic of experimental apparatus

The moving model train facility consists of a 1/11 scale model track laid out on a viaduct over a straight line of approximately 400 m (Fig. 3). The maximum length of the model train is 13.2 m (6 cars), and the maximum speed is 27.8 m/s (100 km/h). The acceleration and deceleration of the model train are controlled by a traction device with ropes connected to the leading and trailing cars.

Compared to wind tunnel experiments, which are commonly used to investigate the flow around a train, this experiment can simulate the following phenomena:

- Couette flow between the under-floor of the train and the track
- Rotational winds at the wheels
- Winds and pressure fluctuations induced by train passage acting on the track

In addition, by spreading simulated-snow particles on the track, the following phenomena can be also simulated:

- Snow particles floating from the track as the train runs
- Snow particles drifting in the flow around bogies

However, reproduction of actual snow accretion phenomena is difficult using simulated-snow particles, therefore in this experiment, quantitative comparison with the amount of particle adhesion on the actual train is not performed.

3.2 Physical similarity rule

In the case of wind tunnel experiments for snow on buildings, activated clay (a fine powder obtained by heat-treating montmorillonite) has been commonly used to simulate snow particles [2]. It has relatively high similarity to the motion of snow particles and white appearance which looks like actual snow. Activated clay is not suitable for this experiment when used outdoors, as its properties are likely to change with atmospheric humidity because of its high hygroscopicity.

For this reason, walnut shell powder, which has similar physical properties as activated clay, was used in this experiment. Table 1 shows the similarity laws of the model experiments. This table shows that the Reynolds number, which represents the ratio of the inertial and viscous forces of the flow, is two orders of magnitude smaller than that of the actual flow. But, if the flow around the bogie is in a turbulent state, the viscous effect can be ignored, and this similarity rule is relaxed.

Test section with simulated-snow particles (90 m)

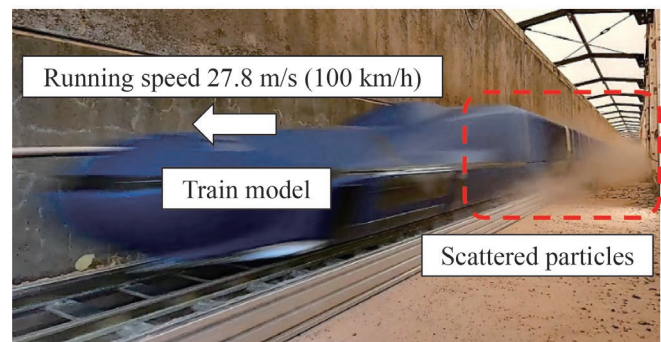
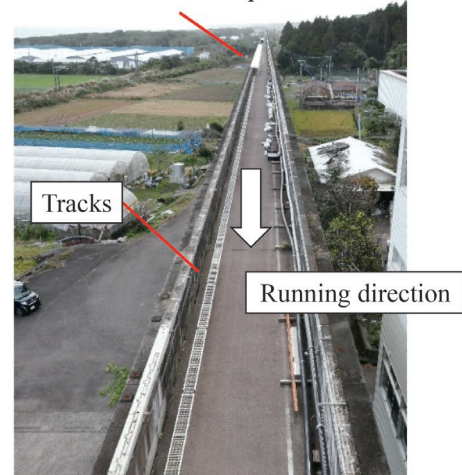


Fig. 3 Moving model train facility

Following parameters between actual snow and simulated-snow particles are almost equal:

- Ratio of threshold shear velocity for snow particles creeping on the snow surface and mainstream velocity
- Froude number for snow particles floating from the snow surface
- Ratio of terminal velocity for snow particles and mainstream velocity
- Stokes parameter for snow particles tracking the flow [3]

Since the Stokes parameters of both the actual and the model exceed 1, snow particle motion does not coincide with fluid motion in the bogie, and complex snow particle motion is estimated.

Table 1 Similarity laws of model experiment

	Actual snow	Snow-simulating particle
Flow velocity under vehicle U_b	36.1 m/s	14.0 m/s
Hight of cavity at bogie L_b	1.0 m	0.09 m
Particle diameter L_p	1.1 mm	0.125 mm
Density of particles	920 kg/m ³	1400 kg/m ³
Response time of particles	0.2 s	0.05 s
Raynolds number	2.4×10^6	8.5×10^4
Ratio of threshold shear velocity	7.6×10^{-3}	9.3×10^{-3}
Froude number	1.6×10^2	1.4×10^2
Ratio of terminal velocity	2.8×10^{-2}	3.4×10^{-2}
Stokes parameter	2.0	2.6

Train speed is 260 km/h and $U_b = \text{train speed} \times 0.5$

In actual snow adhesion, snow adheres by mechanical entanglement of snow particles, surface tension between snow and a solid surface, and sintering between ice particles [4]. In contrast, simulated-snow particles in dry conditions adhere by Coulomb force (electrostatic force), and it is two orders of magnitude smaller than the adhesion force of actual snow. Therefore, the amount of adhesion with simulated-snow particles will be less than that of actual snow.

However, this model experiment using simulated-snow particles allows comparison and verification under certain conditions without snow quality changes due to various weather conditions.

3.3 Snow floating and drifting by running train model

Figure 4 shows the volume of simulated-snow particles scattered by running the train model. Here, the volume of particles scattered is obtained by measuring the number of particles with a diameter of 0.05 mm or larger in the airflow with a particle counter installed next to the track. From this figure and the high-speed video installed next to the track, simulated-snow particles float up from the track as the model train runs, and simulated-snow particles are scattered by the flow around the train.

When the bottom of the bogie section, except for the wheels, was smoothed, the volume of scattered particles decreased significantly. This suggests that the cavity in the bogie section under the train was the main cause of snow particles floating up.

Figure 5 shows the volume of scattered particles integrated with the duration of the train passing. The approximate line was obtained by the least-squares method from the data of each running speed. The volume of scattered particles tends to increase by a factor of 2 to 3 when the running speed increases by a factor of 1.3 ($\approx 21.6/16.2$ m/s). This suggests that the amount of snow scattered is highly dependent on train running speed, and the large amount of snow will flow into bogies on high-speed trains.

However, since the amounts of snow scattered in the upper observation points were much smaller than those near the track surface, the intakes placed at a height of $h/L_b > 0.5$ can take in high-speed running winds without snow.

3.4 Verification of snow accretion measures

The effectiveness of the measure against snow accretion, which consists of intakes and nozzles on both the bogie side covers (see Fig. 2), was examined by moving train model experiments. The running speed was 27.8 m/s (100 km/h).

Figure 6 shows the adhesion of simulated-snow particles on covering body panels at the rear of bogies (hereafter referred to as targeted panel). The white color indicates the adhesion of simulated-snow particles after running the train model. Here, the average luminance of the RGB signals from the photo of the targeted panel with the adhesion of simulated-snow particles, excluding the background color, was converted to a grayscale image.

In normal conditions without any measures taken, simulated-snow particles tend to adhere in the following locations:

- Lower part of the targeted panel "A" in Fig. 6(a), where the impact angles of particles against the targeted panel are almost vertical
- Side corner "B" and upper corner "C" in Fig. 6(a), where the flow is stagnant.

In contrast, when measures are taken with intakes and nozzles, the running wind is drawn in through the intakes and reaches the area near the wheels in the bogie, and there is a reduction in the adhesion of simulated-snow particles in the red frame area in Fig. 6(b).

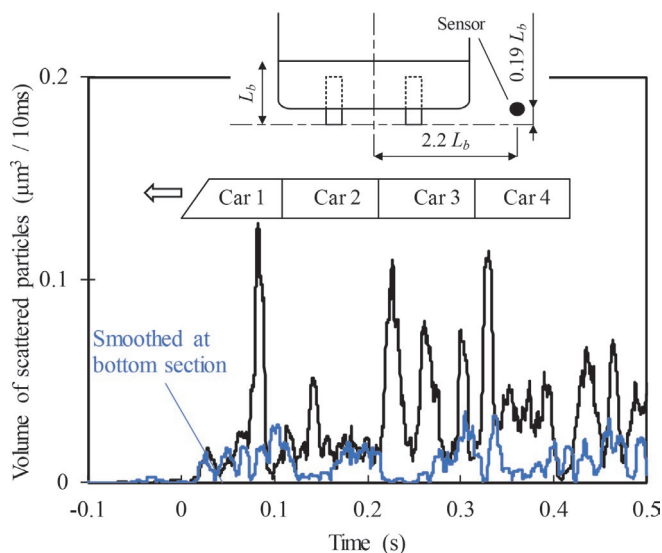


Fig. 4 Volume of particles scattered by running train model

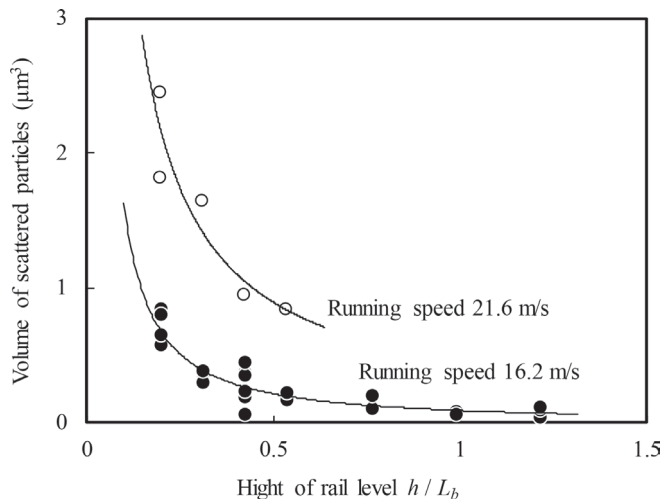


Fig. 5 Volume of scattered particles integrated with duration of train passage

4. Verification by wind tunnel facility

Wind tunnel experiments equipped with a snowfall machine were carried out at Snow and Ice Research Center, National Research Institute for Earth Science and Disaster Prevention [5].

Figure 7 shows the experimental apparatus. Due to the limitation of the wind tunnel scale, only the under-floor parts of the lead car of the model train were used, and snow accretion was evaluated on the rear bogie of the lead car. Felt cloth was attached to the surface of the targeted panel to facilitate snow accretion. The mainstream velocity was 20 m/s, the airflow temperature was -2°C , and snow was supplied from the upstream floor for 10 minutes. The snow was powder stellar dendrite crystal snow made by the snowfall machine.

Figure 8 shows snow accretion on the targeted panel. In the case of normal conditions without measures, snow tends to accrete on the lower part of the targeted panel "A" in Fig. 8(a), side corners "B", and upper corners "C". The locations of their accretion are near to those of the moving model experiments (see Fig. 6(a)).

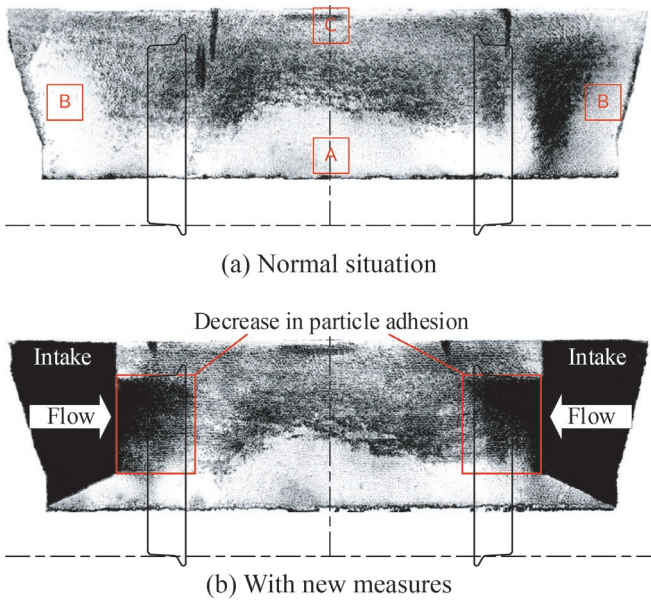


Fig. 6 Particle accretion in moving model experiment

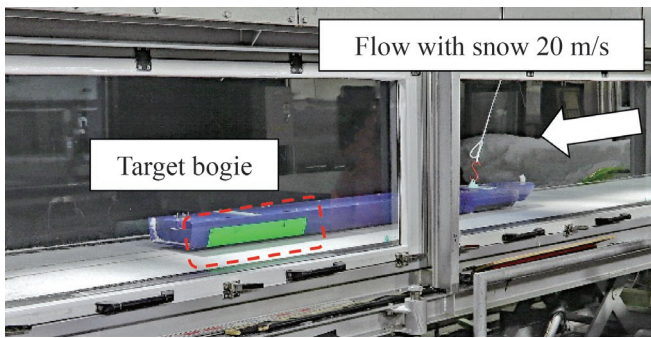


Fig. 7 Wind tunnel facility with snowfall machine

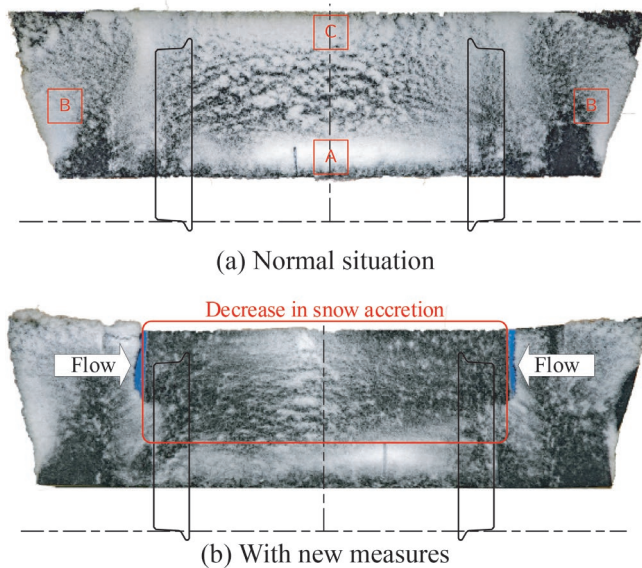


Fig. 8 Snow accretion in wind tunnel experiment

In contrast, when measures are taken with the intakes and the nozzles, snow accretion was suppressed in a wide area from the nozzle outlet to the center area of the targeted panel.

Figure 9 shows the mass of snow accretion for each condition. The mass was the average of two 10-minute snowfall experiments. The measures against snow accretion reduced the amount of snow accretion on the targeted panel by about half.

5. Verification by numerical simulation

Numerical simulation coupled with air flow analysis and snow accretion analysis was carried out to validate the measures against snow accretion using running winds.

5.1 Airflow analysis

The “Airflow Simulator” developed by RTRI was used [6]. In this simulator, unsteady and uncompressed flow around a model car was analyzed using Large Eddy Simulation (LES). The model train consists of a lead car body and two bogies, and the geometry of the measures taken, with intakes and nozzles, was set up for the rear bogie as the evaluation site. The computational grids consisted of 606 grids in the rail direction(x), 740 grids in the lateral direction(y), and 214 grids in the vertical direction(z), for a total of approximately 100 million unequally spaced orthogonal grids. The boundary conditions of the inflow and track surface were fixed to a running speed of $U=20$ m/s, and the wheel boundaries were given tangential velocities corresponding to the running speed.

Figure 10 shows the mean velocity distribution (vector absolute value) in the bogie. The measures condition in Fig.10(b) shows that the running wind taken in from the intakes blow out to the targeted panel near the downstream of the wheels. The xz-sectional view also shows that in normal conditions, the airflow enters the bogie from the bottom of the bogie center toward the top of the rear wheel. When measures are taken, the airflow from the nozzle outlet obstructs this flow.

5.2 Snow accretion calculation

The “Snow accretion simulator” developed by RTRI was used

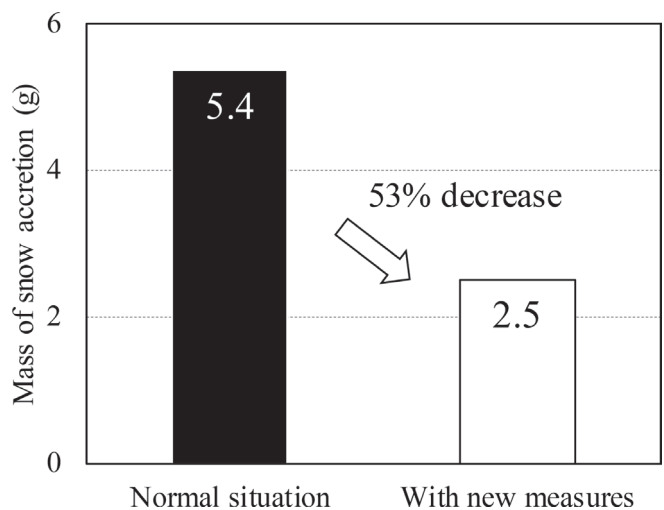
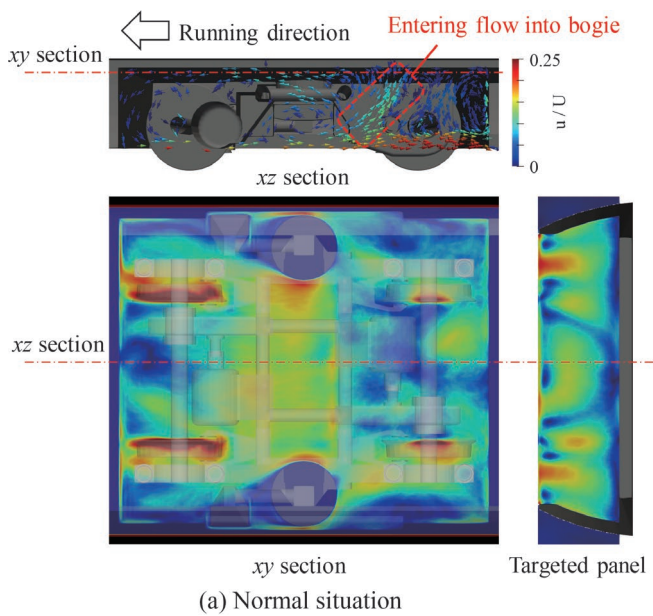
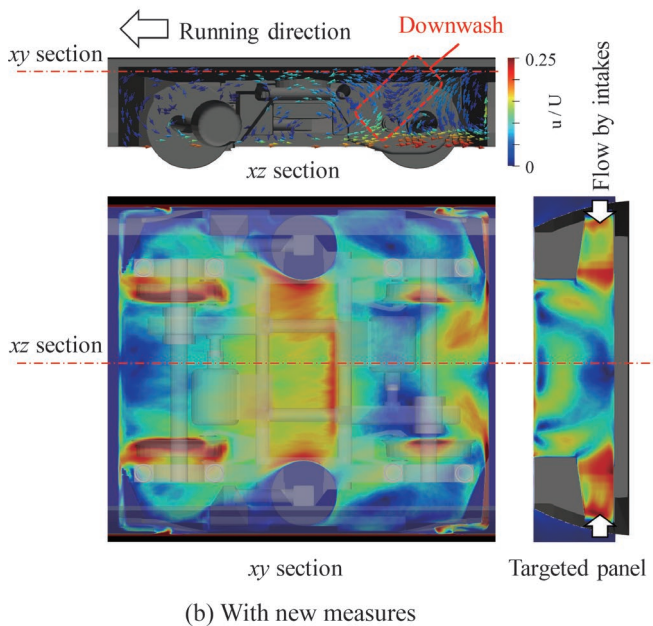


Fig. 9 Mass of snow accretion in wind tunnel experiment



(a) Normal situation



(b) With new measures

Fig. 10 Mean velocity distribution in bogie

to conduct a computer simulation of the process of snow accretion around bogies [7]. The simulator repeats three categories of calculations: calculations to analyze airflow around the object, to trace movements of flying snow particles and to assess the growth of snow accretion. These calculations reflect the airflow around the object whose surface shape evolves as snow accretion increases in the simulation.

Figure 11 shows the snow accretion on the targeted panel with snow particles indicated by white color. A comparison of the shape of accretion when measures are taken to the shape obtained in normal conditions, shows that snow accretion is suppressed near the outlet of the targeted panel and on the top surface of the bogie. According to the airflow calculation in Fig. 10, these areas where the snow accretion is suppressed correspond to the area where the flow is accelerated by the intakes.

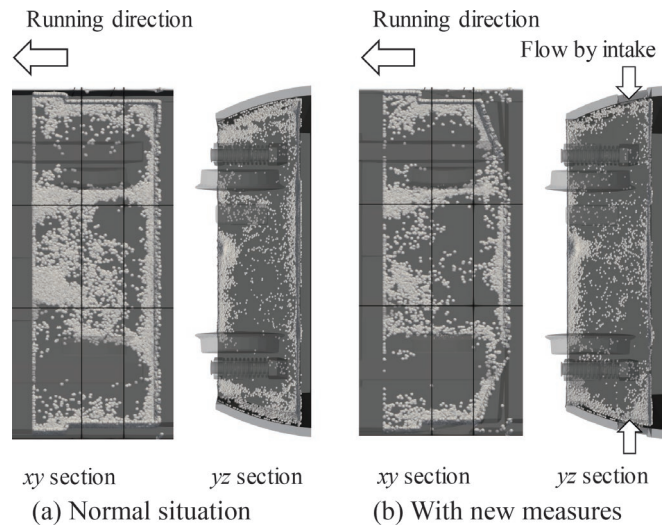


Fig. 11 Snow accretion in CFD

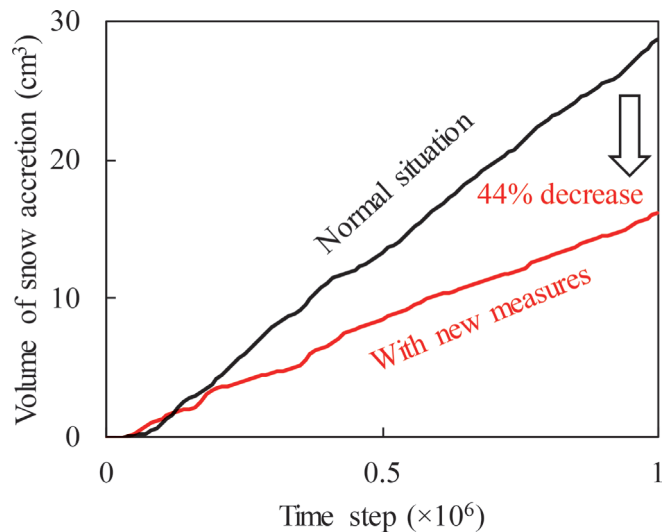


Fig. 12 Snow accretion volume in CFD

Figure 12 shows the snow accretion volume in the calculated area consist of the targeted panel and the top surface of the bogie. From this figure, based on the shape of accretion when measures are taken, it is estimated that taking measures reduces the volume of snow accretion by 44% compared to normal conditions.

6. Conclusions

In this study, a new method for suppressing snow accretion was investigated for covering body panels at the rear of bogies which are prone to snow accretion. The measures introduced utilize the high-speed air flow through intakes and nozzles on both sides of a train.

The results show that this method is expected to reduce snow accretion onto covering body panels at the rear of bogies by about half.

However, it is still unclear whether this method is effective enough in the actual vehicle environment where snow characteristics vary depending on weather conditions. Verifications in actual train environments with snow will be carried out in the future.

References

- [1] Kamata, Y., Murotani, K., Nakade, K., Takahashi, D., Sato, K. and Nemoto, M., “Development of snow accretion simulator for railway vehicles (Part 1),” *J. of the Japanese Soc. of Snow and Ice*, Vol. 83, No. 1, pp. 79-95, 2021 (in Japanese).
- [2] Mitsuhashi, H., “Snowdrifting on building and wind tunnel experiment using model snow,” *J. of the Japanese Soc. of Snow and Ice*, Vol. 65, No. 3, pp. 287-295, 2003 (in Japanese).
- [3] Oikawa, S., Tomabechi, T. and Ishihara, T., “Study of Wind Tunnel Similarity of Snowdrift around Buildings,” *J. of Snow Eng. of Japan*, Vol. 23, No. 2, pp. 13-32, 2007 (in Japanese).
- [4] Maeno, N., “Adhesion and friction of ice,” *J. of the Japanese Soc. of Snow and Ice*, Vol. 68, No. 5, pp. 449-455, 2006 (in Japanese).
- [5] Tsutsumi, T., “Full-Scale-Tests of Snow and Ice with Wind Tunnel,” *Wind Eng., JAWE*, Vol. 43, No. 2, pp. 155-158, 2018 (in Japanese).
- [6] Nakade, K., “LES of the underfloor flow for a railway vehicle,” *30th symposium on computational fluid dynamics*, 2016.
- [7] Murotani, K., Nakade, K. and Kamata, Y., “Development of snow accretion simulator for railway vehicles (Part 2),” *J. of the Japanese Soc. of Snow and Ice*, Vol. 83, No. 5, pp. 468-487, 2021 (in Japanese).

Authors



Hajime TAKAMI, Ph.D.
Senior Chief Researcher, Vehicle
Aerodynamics Laboratory, Environmental
Engineering Division
Research Areas: Aerodynamics



Hidenori ISHII
Researcher, Computational Mechanics
Laboratory, Railway Dynamics Division
Research Areas: Computational Mechanics



Yuto ARAKI
Researcher, Vehicle Aerodynamics
Laboratory, Environmental Engineering
Division
Research Areas: Aerodynamics



Yasushi KAMATA, Ph.D.
Senior Chief Researcher, Head of
Meteorological Disaster Prevention
Laboratory, Disaster Prevention Technology
Division
Research Areas: Snow Disaster Prevention



Kohei MUROTANI, Ph.D.
Senior Researcher, Computational Mechanics
Laboratory, Railway Dynamics Division
Research Areas: Computational Mechanics

Reducing Micro-pressure Waves Using Train Nose Optimization Based on Linear Acoustic Theory

Tokuzo MIYACHI

Hidehiko OKUBO

Heat and Air Flow Analysis Laboratory, Environmental Engineering Division

Katsuhiko KIKUCHI

Vehicle Aerodynamics Laboratory, Environmental Engineering Division (Former)

The shapes of train noses have been optimized for several decades to reduce the peak values of the micro-pressure waves radiating from tunnel portals of high-speed railways. This study optimized the shapes of multistep noses using three transfer functions based on the theory of compact Green's function (W_T), experimental results (W_E), and the average value of W_T and W_E (W_M). Model experiments were performed to measure the maximum pressure gradients of compression waves generated by each train nose entering a tunnel for offset running. For optimized train noses based on W_T or W_E , the values of the maximum pressure gradient could not be sufficiently reduced, and the pressure gradient waveforms were not trapezoidal. Although the optimized noses based on W_M reduced the maximum pressure gradients considerably, the maximum pressure gradient values were larger than those for the optimized noses based on the computational fluid dynamics.

Key words: compact Green's function, moving model rig, acoustic theory

1. Introduction

A train entering a tunnel compresses the air in front of it and generates a compression wave. A pulsive wave, referred to as a micro-pressure wave (MPW), radiates outward when the compression wave arrives at the tunnel exit. Because the MPWs can cause severe noise around the exit, the peak values of the MPWs must be reduced for high-speed railways. The peak value of an MPW is proportional to that of the pressure gradient of the compression wave arriving at the exit. Therefore, the maximum pressure gradients of the compression waves must be reduced to reduce the MPWs. Optimizing train nose shapes and tunnel hoods [1] are practical countermeasures that are widely used in the Shinkansen in Japan.

Kajiyama et al. [2] reported the effect of train nose length before the 1990s, and Maeda et al. [3] and Iida et al. [4] showed that effective train nose shapes have a small gradient of cross-sectional area distribution, except at the tip and end. In Japan, train noses have been optimized (referred to as conventional noses in this paper) based on the outcomes of the aforementioned studies. Thus, train noses have large and small increments in height and width around a driver's cab, respectively, to avoid a large gradient of cross-sectional area.

On the contrary, several studies [5]-[13] have reported optimizing train noses to reduce MPWs. Miyachi et al. [14] and Miyachi et al. [15] showed that multistep train noses effectively reduce the MPWs when the responses to each step do not overlap. Therefore, the distance between individual steps should be larger than half the wavelength of the response. The unit response is calculated according to the linear acoustic theory (LAT) using the compact Green's function [16], [17]. Although the basic idea of the multistep train noses is qualitatively based on the LAT, because the LAT does not consider flow separation and large flow separation results in an increase in the MPWs [18], the flow separation in quantitative optimization using this method is not ideal. Miyachi et al. [15] optimized train nose shapes using the axisymmetric computation fluid dynamics to consider the nonlinear effect and flow separation at each step when a train runs at the center of the tunnels (center running).

Because all Shinkansen tunnels are double-track and trains al-

ways run at offset positions in the tunnels (offset running), the three-dimensional effect should also be analyzed using three-dimensional computational fluid dynamics (3D-CFD). However, this may further increase the calculation time required. In contrast, the LAT can instantaneously predict the impact of train nose shapes by calculating the convolution between the cross-sectional area distribution of the train nose and the transfer function for offset running. Although the optimum train noses based on the LAT have discontinuous steps, by setting bounds to the optimization design space for avoiding such sharp steps and exploring only rounded multistep noses, the train noses can be optimized for offset running within a short time.

This study optimized the shapes of multistep noses using three transfer functions based on the theory of compact Green's function (W_T), experimental results (W_E), and the average value of W_T and W_E (W_M) for the offset running. Model experiments were undertaken to evaluate the optimized noses.

2. Linear acoustic theory

2.1 Howe's acoustic theory

A compression wave is generated when a high-speed train enters a tunnel, which then causes an MPW. As the peak value of the MPW is proportional to that of the pressure gradient of the compression wave, the performance of the train nose on MPW mitigation can be evaluated using the maximum pressure gradient of the compression wave. The waveform of the pressure gradient of the compression wave with a low Mach number assumption, which is obtained when the correction for nonlinear effect is applied to Howe's acoustic theory [16][17], is expressed as [19]

$$\frac{\partial p}{\partial t}(x, t) = \frac{\Delta p_H}{r_0/U} \int_0^{L_s} \frac{dA^*}{dX}(\theta) W([T] - \theta) d\theta, \quad (1)$$

$$\Delta p_H = \frac{1}{2} \rho U^2 \frac{1 - (1 - R)^2}{(1 - M)(M + (1 - R)^2)}, \quad (2)$$

where U is the train speed, $X = x/r_0$, (x, y, z) are the rectangular coordinate axes, $T = t/(r_0/U)$, $[T] = T - M(X - \ell/r_0)$, $\ell \sim 0.61r_0$ is the end correction, $M = U/c_0$ is the train Mach number, c_0 is the speed of sound, $L_n = \ell_n/r_0$, r_0 is the equivalent radius of the tunnel, ℓ_n is the train nose length, $A^* = A/A_0$, A is the cross-sectional area distribution of the train nose, A_0 is the maximum cross-sectional area of the train, W is the transfer function, R is the blockage ratio between the train and tunnel ($R = A_i/A_0$), A_0 is the cross-sectional area of the tunnel, and ρ is the air density. The equivalent radius r_0 is defined according to the mirror image of the tunnel, $r_0 = \sqrt{2A_0/\pi}$, and Δp_H is the pressure rise of the compression wave [19][20] without significant flow separation. The origin of the coordinate is taken at ground level in the plane of the tunnel entrance. The tunnel extends along the negative x axis.

As the pressure rise does not depend on the train nose shape when there is no flow separation, as shown in Eq. (2), it is well known that the waveform of the pressure gradient (time vs. pressure gradient) should be a symmetric trapezoid [4].

2.2 Multistep train nose

Figure 1 shows the transfer function W_T theoretically defined based on the compact Green's function [16]. Here, W_T has a Gauss function-like waveform with a single peak, and it is a pressure gradient waveform generated by a snub nose train (zero-nose-length train). This means that the waveform is the unit response to $(dA^*/dX) = \delta(X)$. W_T includes the impact of the offset position, i.e., $W_T = W_T(t, (y, z))$.

Miyachi et al. [14] showed that when W_T is approximated using a triangle pulse with a width of 2λ , the optimum train nose shape is expressed as follows:

$$\ell_n/\lambda = k, \quad (3)$$

$$\frac{dA^*}{dX} = \frac{1}{k+1} \sum_{i=0}^k \delta(X - i\lambda/r_0), \quad (4)$$

$$A^* = \frac{1}{k+1} \sum_{i=0}^k H(X - i\lambda/r_0), \quad (5)$$

where k is a natural number. Equations (3)-(5) show a multistep train nose shape, consisting of discontinuous $(k+1)$ steps with $A_i/(k+1)$ of cross-sectional area at every λ of width.

Figure 2 shows the pressure gradient waveform generated by a train nose expressed by Eqs. (3)-(5) for $\ell_n/\lambda = k = 2$, the three-step nose, using the triangle transfer function. Because the peaks of the triangle responses to each step do not overlap, the pressure gradient wave exhibits a trapezoidal waveform.

2.3 Optimization problem

An optimization problem was considered where the design variables expressing the gradient of the cross-sectional area distribution of the train nose, dA^*/dX , were optimized to minimize the objective function $(\partial p/\partial t)_{\max}^* \equiv \max[(\partial p/\partial t)^*]$, where $(\partial p/\partial t)^* \equiv (\partial p/\partial t)/(\Delta p_H U/2r_0)$ is the non-dimensional pressure gradient with the constrained conditions $dA^*/dX > 0$ and $0 \leq \int_0^X dA^* = A^*(X) \leq 1$. Therefore, the cross-sectional area distribution does not exceed A_i . The problem is summarized as follows:

Min:

$$\left(\frac{\partial p}{\partial t}\right)_{\max}^* = \max \left[2 \int_0^{L_n} \frac{dA^*}{dX}(\theta) W([T] - \theta) d\theta \right]; \quad (6)$$

Subject to:

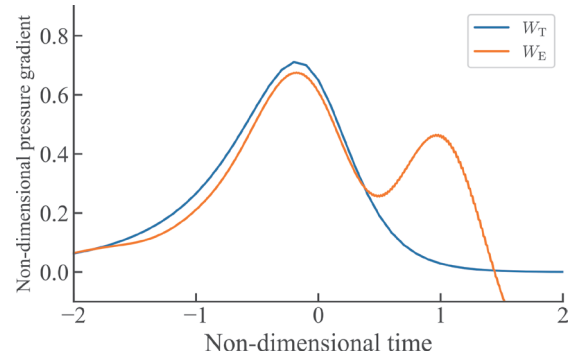


Fig. 1 Transfer functions

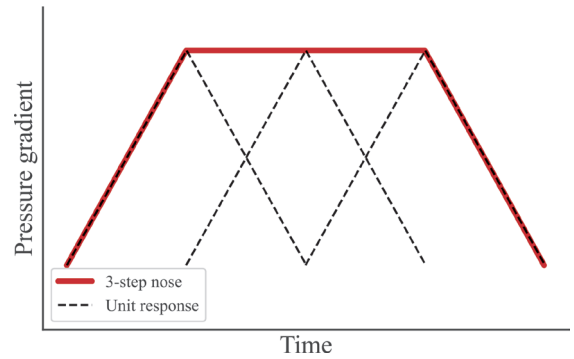


Fig. 2 Schematic diagram of the pressure gradient waveform generated by a three-step train nose using a triangle transfer function

$$\frac{dA^*}{dX}(X) > 0, \quad (7)$$

$$0 \leq \int_0^X dA^* = A^*(X) \leq 1. \quad (8)$$

Here, because $(\partial p/\partial t)_{\max}^*$ is non-dimensionalized by Δp_H and $2r_0/U$, the train speed and blockage ratio do not affect the optimization result.

As the three-step train noses for the center running suggested by Miyachi et al. [15] are assumed in this study, the gradient of cross-sectional area distribution, dA^*/dX , is expressed by three Gaussian functions as follows:

$$\frac{dA^*}{dX} = \sum_{i=0}^{m-1} f \frac{c_i}{\sqrt{\pi}} \exp \left[-\frac{(X - b_i)^2}{\sigma_i^2} \right], \quad m = 3, \quad (9)$$

$$\frac{L_n - d}{m} ((i - 1) + 0.001) \leq b_i < \frac{L_n - d}{m} \times i, \quad (10)$$

$$0 \leq i < m - 1, \quad (11)$$

where b_i , c_i , and σ_i are the center, weight, and width of each Gaussian function, respectively, and m is the number of steps ($m = 3$). Here, σ_i denotes the steepness of each step, and the steps are steeper for smaller values of σ_i . Further, d is the buffer where the center of the final step should not exist around the end of the train nose, and f is a weighting function to smooth the end of the train nose. The following bounds were set to avoid small values of σ_i :

$$\sigma_{\min} < \sigma_i < \sigma_{\min} + 0.4 \quad (12)$$

The weighting function f that smooths the last two meters of noses in full scale is defined as follows:

$$\text{For } X > L_n - 2r_0$$

$$f = \frac{1}{2} \left[1 + \cos \left(\frac{X - \left(L_n - \frac{2}{r_0} \right)}{\frac{2}{r_0}} \pi \right) \right]; \quad (13)$$

For $X \leq L_n - 2/r_0$
 $f = 1.$ (14)

The parameters σ_{\min} , d , and f were used to avoid steep steps causing flow separation. The number of design variables is $3m - 2$. A simple generic algorithm was used to optimize the design values.

Table 1 shows the specifications of five train noses optimized in this study, referred to as N02, W02, W02B, S02, and W01. For W02, W02B, and W01, the weighting functions in Eqs. (13) and (14) were used.

2.4 Optimization using W_T

The train noses optimized using W_T are labeled as ‘-T.’ Figure 3 shows the gradients of cross-sectional areas of N02-T, W02-T, and W02B-T, where $A_0 = 63.4 \text{ m}^2$, $\ell_n = 12 \text{ m}$, and the train offset is 2.2 m in full scale. Evidently, the waveforms of the first and third steps are large peaks, and those of widths are small. Further, the waveforms of the second steps have small peak values and are extensive.

Table 1 Specifications of train noses

Index	Type	f	d	σ_{\min}
1	N02	1	0	0.2
2	W02	Eqs. (13), (14)	σ_{\min}	0.2
3	W02B	Eqs. (13), (14)	$2\sigma_{\min}$	0.2
4	S02	1	σ_{\min}	0.2
5	W01	Eqs. (13), (14)	σ	0.1

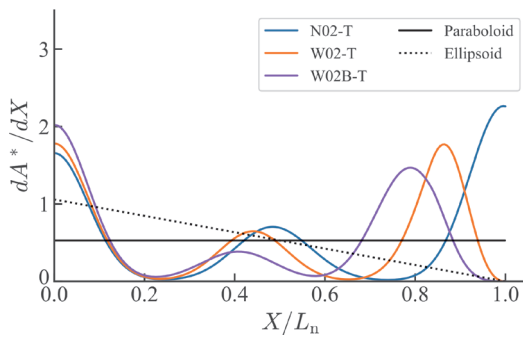


Fig. 3 Gradients of the cross-sectional area optimized using W_T ($\ell_n = 12 \text{ m}$ in full scale)

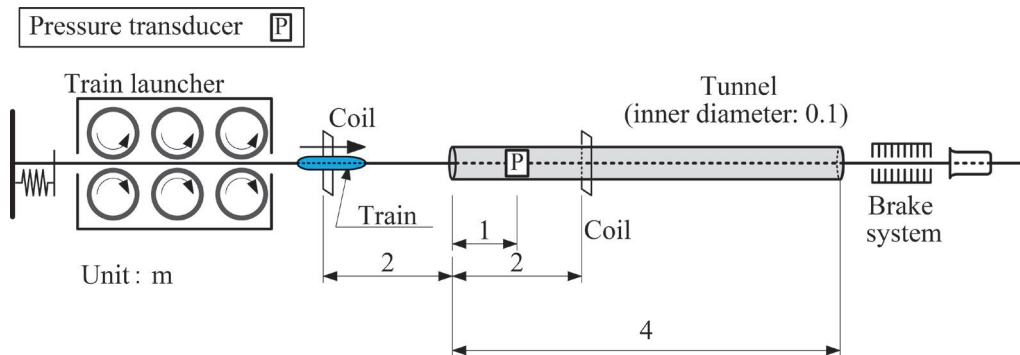


Fig. 4 Schematic of the experimental apparatus

3. Model experiment

3.1 Experimental apparatus

Experiments were performed to measure the value of $(\partial p / \partial t)_{\max}^*$ generated by noses optimized in Sec. 2.3 using the moving model rig [21]. Table. 2 shows specifications of model experiments. Figures 4 and 5 show the schematic of the experimental apparatus and the moving model rig, respectively. The scale of experiments was 1/127 based on the assumption that the Shinkansen tunnels have a cross-sectional area of 63.4 m^2 in full scale, based on the method of images. The speed and blockage ratio of model trains were 360 km/h and 0.17, respectively. Pressure signals were measured using two pressure transducers (Kulite XCS-190-5G) flush-mounted on a pipe of diameter 100 mm. The speed of the train was measured using two coils shown in Fig. 4 and the magnets installed in the model trains. The pressure gradient waveforms were calculated according to the central difference. The five noses, N02-T, W02-T, W02B-T, ellipsoid, and paraboloid, were tested. The ellipsoid nose is used as the reference for non-separation waveforms. Here, $(\partial p / \partial t)_{\max}^*$ for the paraboloid nose, is an indicative value (target value) of optimization as it generates a relatively small value of $(\partial p / \partial t)_{\max}^*$ although it is a simple shape.

3.2 Experimental results

Figures 6 and 7 show the non-dimensional waveforms of pressure and pressure gradients generated by N02-T, W02-T, and W02B-T, respectively. Here, the pressure and time are non-dimensionalized with Δp_H and $2r_0/U$, respectively. The nose tip of the trains passes the entrance of the tunnel at $T = 0$. As the non-dimensional pressure rises for N02-T, W02-T, and W02B-T are approximately one and equal to that for ellipsoid regarded as the non-flow-separation nose, there is no significant flow separation

Table 2 Specifications of model experiments

Blockage ratio R	0.17
Speed U (km/h)	360
Tunnel diameter (mm)	100
Nose length (mm)	94.5
Train length (mm)	1190
Train offset (mm)	17
Scale ratio	1/127
Trail shape	Ellipsoid
Nose length in full scale (m)	12



Fig. 5 Moving model rig

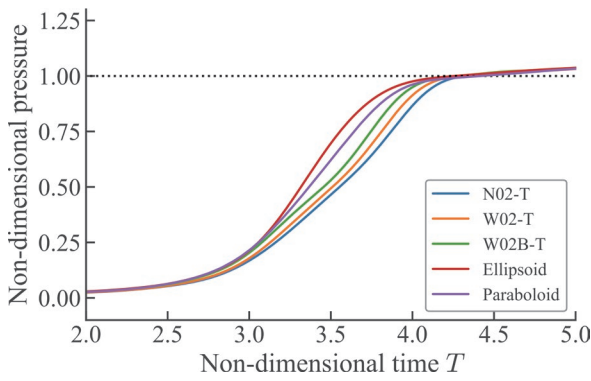


Fig. 6 Experimental results of non-dimensional waveforms of pressure generated by noses optimized with W_T (Train speed: 360 km/h)

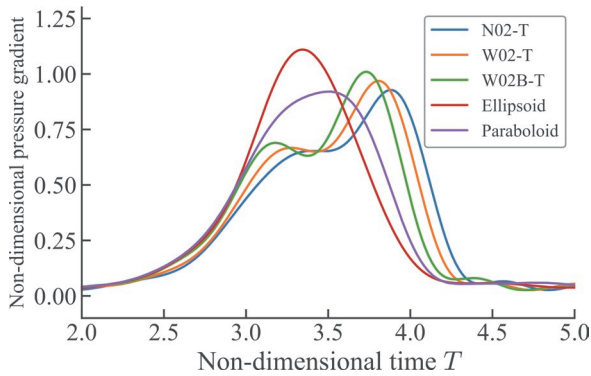


Fig. 7 Experimental results of non-dimensional waveforms of pressure gradient generated by noses optimized with W_T (Train speed: 360 km/h)

around these three noses. This implies that the three parameters, σ_{\min} , d , and f , helped avoid large flow separation. Figure 7 indicates that the waveforms of the pressure gradient for N02-T, W02-T, and W02B-T are not symmetric, and the values of $(\partial p/\partial t)_{\max}^*$ are greater than that of the paraboloid nose, which is the target value. Therefore, the optimization is insufficient and fails because the LAT does not consider the nonlinear effect.

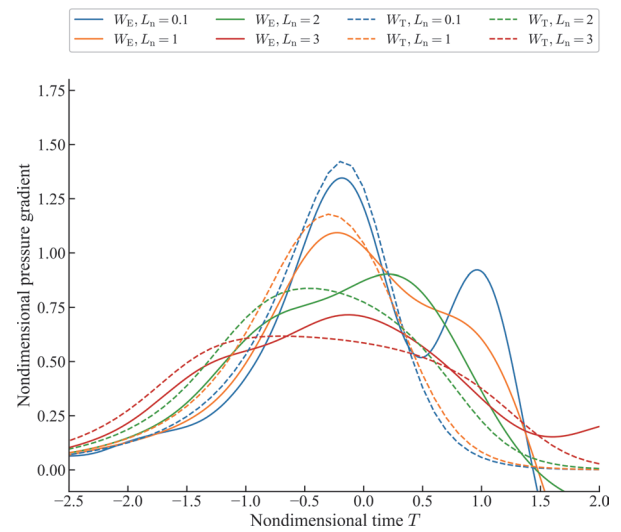


Fig. 8 Comparisons of the pressure gradient waveforms calculated using W_T and W_E for a paraboloid

4. Optimization using Wiener filter

4.1 Transfer function W_E based on experimental results

To consider the nonlinear effect in Eq. (1) without using the 3D-CFD, the transfer function based on experimental results, W_E , was introduced using the Wiener filter. The cross-sectional area distribution and the waveform of pressure gradient for W02B-T, which generated the largest value of $(\partial p/\partial t)_{\max}^*$ among all noses tested in Sec. 3 (i.e., the worst nose), are regarded as input and output, respectively.

Figure 1 shows the obtained transfer function W_E , which has two peaks: the first peak is greater than the second. The W_T , however, has a single peak. Figure 8 compares the pressure gradient waveforms using W_T and W_E for a paraboloid. When using W_T , the pressure gradient waveforms have a single peak for $L_n = \ell_n/r_0 \leq 2$, and the waveform is downward to the right for $L_n = 3$. When using W_E , the pressure gradient waveforms have two peaks, and the waveforms are downward to the right for $L_n \leq 1$, wherein the first peak is greater than the second peak, whereas the waveforms are upward to the right for $L_n \geq 2$. The waveform of the experimental result for $L_n = 1.89$ shown in Fig. 8 is upward to the right, and this tendency is similar to that of the calculation result using W_E for $L_n = 2$ in Fig. 8.

4.2 Optimization using W_E

The train noses were optimized by considering the nonlinear effect using W_E . As the convolution in Eq. (6) only corresponds to the LAT, even if the transfer function W_E is substituted to W in Eq. (6), the nonlinear effect cannot be fully considered for all input functions. Thus, the transfer function is corrected as follows:

$$W(\alpha) = (1 - \alpha) W_T + \alpha W_E, \quad (15)$$

where α is a correction factor. As $\alpha = 0$ and $\alpha = 1$ express W_T and W_E , respectively,

$$W_T = W(0), \quad (16)$$

$$W_E = W(1), \quad (17)$$

The average of W_T and W_E is defined as W_M , i.e.,

$$W_M = W\left(\frac{1}{2}\right) = \frac{1}{2} (W_T + W_E). \quad (18)$$

The noses optimized using W_E and W_M are labeled as ‘-E’ and ‘-M.’ Figure 9 compares the gradients of cross-sectional areas of N02-T, N02-E, and N02-M, which are optimized for N02 shown in Table 1. The third peak of dA^*/dX of N02-E is smaller than that of N02-T, and the second peak of N02-E moves to the front (negative direction in X). This is why the Wiener filter is used to correct the experimental result of N02-T, which is upward to the right, considering the nonlinear effect.

Four types of noses, N02, W02, S02, and W01, were optimized using W_E and W_M . Table 3 lists the names of the optimized noses. Figure 10 compares the gradients of cross-sectional area optimized using three transfer functions for all noses. Figure 11 shows the model of W01-M for the moving model rig.

4.3 Experimental results

The values of $(\partial p/\partial t)_{\max}^*$ for the seven train noses listed in Table 3 were measured in experiments. Figures 12 and 13 show the measured pressure and pressure gradient waveforms, respectively. The two facts, (1) the waveforms of pressure gradient generated by noses ‘-E’ and ‘-T’ are downward and upward to the right, respectively, and (2) the flow separation does not significantly impact the

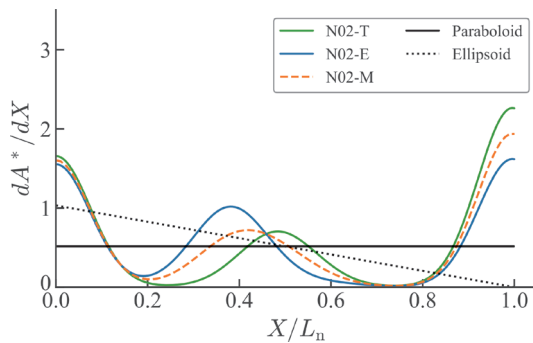


Fig. 9 Comparisons of the gradients of the cross-sectional area optimized using three weighting functions for N02

Table 3 Train noses optimized using W_E and W_T

Type	W_M	W_E
N02	N02-M	N02-E
W02	-	W02-E
S02	S02-M	S02-E
W01	W01-M	W01-E

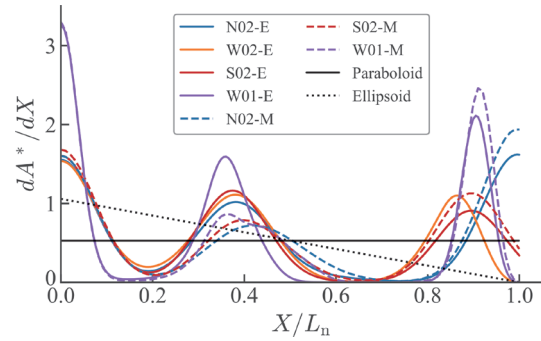


Fig. 10 Comparisons of the gradients of cross-sectional area optimized using three weighting functions for all noses



Fig. 11 Model of W01-M

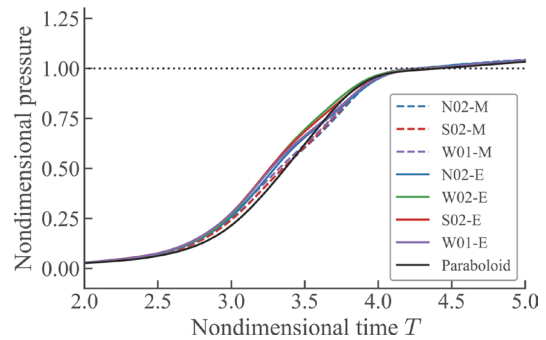


Fig. 12 Experimental results of non-dimensional waveforms of pressure generated by noses optimized using W_E and W_M (Train speed: 360 km/h)

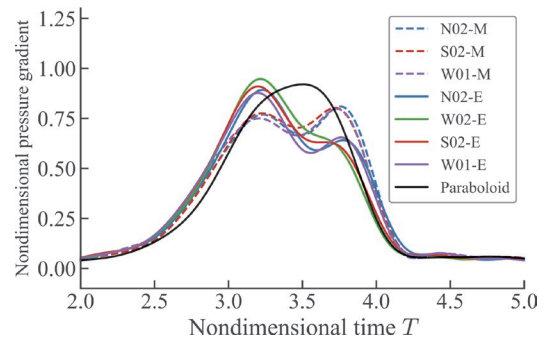


Fig. 13 Experimental results of non-dimensional waveforms of pressure gradient generated by noses optimized using W_E and W_M (Train speed: 360 km/h)

results as the values of non-dimensional pressure rise caused by them are approximately one, indicate that W_E overestimates the nonlinear effect and the correction using it was excessive. The waveforms of pressure gradient generated by noses ‘-M’ are symmetric and values of $(\partial p/\partial t)_{\max}^*$ are smaller than that of a paraboloid. Therefore, optimization using W_M is advanced.

Figure 14 shows a comparison of $(\partial p/\partial t)_{\max}^*$ for all noses, where the values of $(\partial p/\partial t)_{\max}^*$ are normalized with the values of the paraboloid. Among all the tested noses, W01-M was the optimum nose. The normalized $(\partial p/\partial t)_{\max}^*$ for W01-M is 0.87, while that for the best nose optimized in [15] using CFD and the conventional noses are 0.78 and 0.82, respectively, even for the center running. Therefore, the optimization of W01-M using W_M should still be improved.

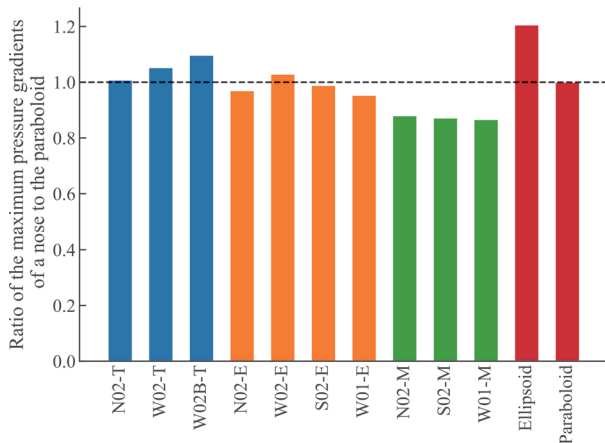


Fig. 14 Comparison of $(\partial p/\partial t)_{\max}^*$ for all noses

5. Conclusions

This study optimized the train noses based on the linear acoustic theory to consider the train offset in double-track tunnels. Three transfer functions based on the compact Green’s function W_T , model experiments W_E , and their average W_M , were used. The pressure gradient waveforms generated by the optimized noses were measured using the moving model rig. The following results were obtained:

(1) Waveforms of the pressure gradient generated by noses optimized using W_T , which is the transfer function based on the theory of compact Green’s function, were upward to the right. Further, the maximum pressure gradients, $(\partial p/\partial t)_{\max}^*$, were larger than that of the paraboloid nose.

(2) The transfer function W_E was introduced based on the experimental results using the Wiener filter to consider the nonlinear effect. The waveforms of pressure gradient generated by noses optimized using W_E were downward to the right. Further, the maximum pressure gradients, $(\partial p/\partial t)_{\max}^*$, were larger than that of the paraboloid nose. Therefore, the correction on the nonlinear effect using W_E was excessive.

(3) The waveforms of pressure gradient generated by noses optimized using W_M , which is the average value of W_T and W_E , were symmetric. As the ratio of $(\partial p/\partial t)_{\max}^*$ for the best nose among all optimized noses to the paraboloid was 0.87, the optimization can be considered successful. However, as the ratio $(\partial p/\partial t)_{\max}^*$ for the best nose optimized using CFD to the paraboloid were reported as 0.78, the optimization using W_M should be further improved.

References

- [1] Ozawa, S., “Studies of micro-pressure waves from a tunnel exit.” *Railway Technical Research Report*, No. 1121, 1979 (in Japanese).
- [2] Kajiyama, H., Kinoshita, M., Maeda, T., Tanemoto, K., “Model experiments on effect of extension of train nose on reducing micro-pressure waves generated upon train entry into tunnel.” *Railway Technical Research Report*, No. A-87-119, 1987 (in Japanese).
- [3] Maeda, T., Matsumura, T., Iida, M., Nakatani, K., Uchida, K., “Effect of Shape of Train Nose on Compression Wave Generated by Train Entering Tunnel.” *Proceedings of the International Conference on Speedup Technology for Railway and Maglev Vehicles*, pp. 315-319, 1993.
- [4] Iida, M., Matsumura, T., Fukuda, T., Nakatani, K., Maeda, T., “Optimization of train nose shape for reducing impulsive pressure wave from tunnel exit,” *Transactions of the Japan Society of Mechanical Engineer Series B*, Vol. 62, pp. 1428-1435, 1996 (in Japanese).
- [5] Ogawa, T., Fujii, K., “Numerical Simulation of Compressible Flow Induced by a Train Moving in a Tunnel,” *Computational Fluid Dynamics Journal*, Vol. 3, pp. 63-82, 1994.
- [6] Ogawa, T., Fujii, K., “Theoretical algorithm to design a train shape for alleviating the booming noise at a tunnel exit,” *Transactions of the Japan Society of Mechanical Engineer Series B*, Vol. 62, pp. 2679-2686, 1996 (in Japanese).
- [7] Kwon, H., Jang, K., Kim, Y., Yee, K., Lee, D., “Nose Shape Optimization of High-speed Train for Minimization of Tunnel Sonic Boom,” *JSME International Journal Series C*, Vol. 44, pp. 890-899, 2001.
- [8] Lee, J., Kim, J., “Kriging-based Approximate Optimization of High-speed Train Nose Shape for Reducing Micropressure Wave,” *Journal of Rail and Rapid Transit*, Vol. 221, pp. 263-270, 2007.
- [9] Lee, J., Kim, J., “Approximate Optimization of High-speed Train Nose Shape for Reducing Micropressure Wave,” *Structural and Multidisciplinary Optimization*, Vol. 35, pp. 79-87, 2008.
- [10] Ku, Y.-C., Rho, J.-H., Yun, S.-H., Kwak, M.-H., Kim, K.-H., Kwon, H.-B., Lee, D.-H., “Optimal Cross-sectional Area Distribution of a High-speed Train Nose to Minimize the Tunnel Micro-pressure Wave,” *Structural and Multidisciplinary Optimization*, Vol. 42, pp. 965-976, 2010.
- [11] Kikuchi, K., Iida, M., Fukuda, T., “Optimization of Train Nose Shape for Reducing Micro-pressure Wave Radiated from Tunnel Exit,” *Journal of Low Frequency Noise, Vibration and Active Control*, Vol. 30, pp. 1-19, 2011.
- [12] Muñoz-Paniagua, J., García, J., Crespo, A., “Genetically Aerodynamic Optimization of the Nose Shape of a High-speed Train Entering a Tunnel,” *Journal of Wind Engineering and Industrial Aerodynamics*, Vol. 130, pp. 48-61, 2014.
- [13] Ozawa, Y., Asano, K., Nonomura, T., Oyama, A., Fujii, K., Matori, H., “Characteristics of a train shape for alleviating the booming noise at tunnel exit,” *Proceedings of the Symposium on Computational Fluid Dynamics*, D09-4, 2015 (in Japanese).
- [14] Miyachi, T., Iida, M., Fukuda, T., Arai, T., “Nondimensional Maximum Pressure Gradient of Tunnel Compression Waves Generated by Offset Running Axisymmetric Trains,” *Journal of Wind Engineering and Industrial Aerodynamics*, Vol. 157, pp. 23-35, 2016.
- [15] Miyachi, T., Kikuchi, K., Hieke, M., “Multistep Train Nose for Reducing Micro-pressure Waves,” *Journal of Sound and Vibration*

- tion, Vol. 520, 116665, 2022.
- [16] Howe, M. S., "The compression wave produced by a high-speed train entering a tunnel," *Proceedings of The Royal Society of London A*, Vol. 454, pp. 1523-1534, 1998.
- [17] Howe, M. S., Iida, M., Fukuda, T., Maeda, T., "Theoretical and Experimental Investigation of the Compression Wave Generated by a Train Entering a Tunnel with a Flared Portal," *Journal of Fluid Mechanics*, Vol. 425, pp. 111-132, 2000.
- [18] Sakuma, Y., Miyachi, T., Fukuda, T., Takasaki, T., "The compression wave generated by a bluff-nose train entering a tunnel (1st report, Properties of the compression wave and abatement measures on the infrastructure)," Vol. 76, pp. 2472-2479, 2010 (in Japanese).
- [19] Miyachi, T., "Non-linear Acoustic Analysis of the Pressure Rise of the Compression Wave Generated by a Train Entering a Tunnel," *Journal of Sound and Vibration*, Vol. 458, pp. 365-375, 2019.
- [20] Hara, T., "Aerodynamic force acting on a high speed train at tunnel entrance," *Bulletin of JSME*, Vol. 26, No. 171, pp. 1581-1586, 1960.
- [21] Fukuda, T., Iida, M., "Model experiments on aerodynamics in train-tunnel system," *The Journal of the Acoustical Society of Japan*, Vol. 63, pp. 543-548, 2007.

Authors



Tokuzo MIYACHI, Ph.D.
Senior Researcher, Heat and Air Flow
Analysis Laboratory, Environmental
Engineering Division
Research Areas: Tunnel Aerodynamics,
Micro-pressure Wave



Katsuhiro KIKUCHI, Ph.D.
Senior Chief Researcher, Vehicle
Aerodynamics Laboratory, Environmental
Engineering Division (Former) Research
Areas: Fluid Engineering in Railway



Hidehiko OKUBO
Researcher, Heat and Air Flow Analysis
Laboratory, Environmental Engineering
Division
Research Areas: Aerodynamics

Method to Evaluate Aerodynamic Bogie Noise from Shinkansen High-speed Trains by Considering Acoustic Fields

Nobuhiro YAMAZAKI

Noise Analysis Laboratory, Environmental Engineering Division

Masato NAKAYAMA

Osaka Sangyo University

Takanobu NISHIURA

Ritsumeikan University

Aerodynamic bogie noise was quantitatively estimated at a wayside observation point by using spatial distribution of the sound pressure level (SPL) obtained by a two-dimensional microphone array in a wind tunnel test. In order to evaluate the SPL, it is necessary to appropriately consider noise generation and sound field with respect to various acoustic properties such as ground reflection and insertion loss of a bogie side cover. In this study, the transfer function between the integrated spatial distribution of SPL and results obtained by an omnidirectional microphone were calculated using a numerical method. The SPL of aerodynamic bogie noise of Shinkansen trains can be estimated using this transfer function and compared with the results obtained in field tests.

Key words: railway noise, microphone array, transfer function, acoustic numerical calculation

1. Introduction

For environmental reasons, it is necessary to reduce noise generated by high-speed Shinkansen trains. Noise generated beneath vehicles in particular is a key source of noise, and several studies have been conducted over the years to reduce this noise [1]. We have already quantitatively estimated aerodynamic bogie noise generated from bogie sections of a Shinkansen train, in wind tunnel tests by applying a beam-forming analysis of a microphone array. The results show that the aerodynamic bogie noise becomes dominant, especially below 500 Hz [2].

Since the sound pressure level calculated by the beam-forming analysis of microphones (directive SPL) depends on a directivity pattern and is affected by the arrangement of microphones and distance from the source, it is necessary to use a transfer function to convert the directive SPL to the standard SPL (measured by the omnidirectional microphone). The conventional method uses a transfer function obtained experimentally in wind tunnel tests. However, flow distribution and side cover conditions simulated in wind tunnel tests are different from target conditions, with full side covers under the flow condition of middle cars, to obtain a sufficient signal-to-noise ratio even by a single omnidirectional microphone. Therefore, the sound source and sound propagation cannot be simulated correctly, and its effect on the transfer function applied to the beam-forming analysis has not been clarified yet.

This paper presents a method to estimate the aerodynamic bogie noise quantitatively by applying the transfer function that reflects the influence of the sound field on the directive SPL formed by the ground and bogie cavities. The purpose of this study is to clarify the physical properties (reflection caused by the ground and bogie cavity and insulation loss caused by side covers) of the transfer function in an estimation process. In this proposed method, the transfer function between noise sources inside the cavity and the directive SPL is calculated using a three-dimensional numerical simulation based on the boundary element method (BEM). Secondly, we estimate SPL at a wayside observation point by applying a transfer function between

a source and the observation point which is also obtained by a numerical simulation. Finally, the proposed method is validated by comparing estimated noise from the lower part of cars and measured noise from a field test.

2. Acoustic field around the bogie section

Before studying this method for estimating aerodynamic bogie noise, we carried out an acoustic test using a 1/7 scale train model in an anechoic room in the Large-Scale Low-Noise Wind Tunnel at RTRI. Figure 1 shows the experimental setup. A bogie cavity and side covers were simulated under a train model which was installed on the stage representing the ground. Setup 0 is a condition without the train body and without the ground (free condition). Setup 1 is a condition where the train model was set upside down to remove the influence of the ground. In Setup 2, the train model was placed in normal conditions on the stage with a width of 5.5 m and a length of 7 m. The length of the bogie cavity was 571 mm and the width was 476 mm at the ceiling and 400 mm at the bottom. The coordinate system of the train model was set such that x represents the rail direction, y the sleeper direction and z the vertical direction.

Based on the reciprocal theory, microphones (BK, Type 4935) with a diameter of 1/4 inch and a length of 65 mm were body. This layout is also suitable to gain a sufficient signal-to-noise ratio by using a large speaker with high power compared to when a very small one is used inside the bogie cavity. The influence of the vertical source position was investigated by setting microphones installed at $x = 0, y = 0, z = 41, 71, 101$ mm. White noise emitted by the speaker was recorded by a data recorder (TEAC, WX-7000). The difference in SPL G [dB] is defined as Eq. (1).

$$G(f,z) = L(f,z) - L_0(f,z) \quad (1)$$

Here, L is sound pressure level measured by the microphone and L_0 is SPL measured in the free space condition (Setup 0). All frequencies described in this paper are converted to the real scale.

Figure 2 shows the differences in SPL under the different con-

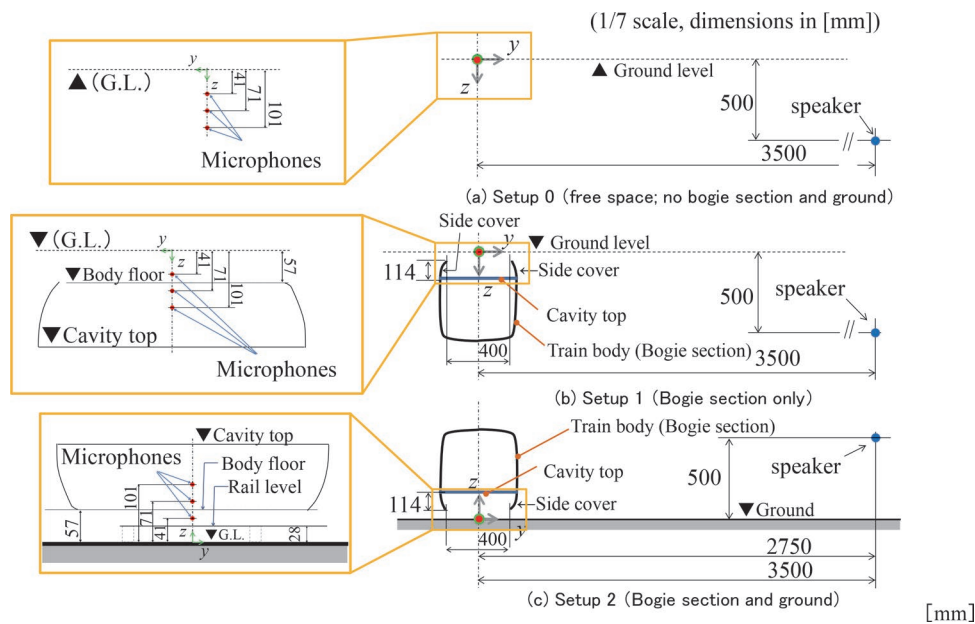


Fig. 1 Experimental setup of the acoustic test, with the speaker and microphone in an anechoic room in the wind tunnel set oppositely based on the reciprocal theorem.

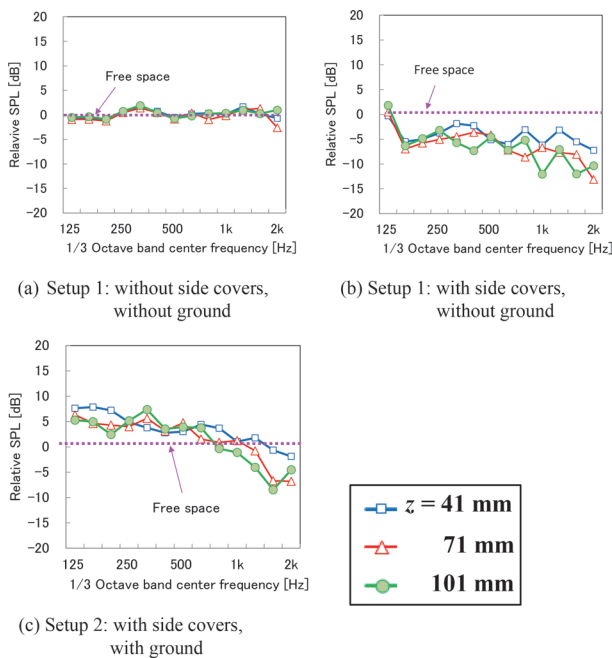


Fig. 2 Relative SPL beside the bogie cavity (Acoustic test)

conditions of the ground and side covers. We can see that the decreases are apparent above the 160 Hz band owing to sound insulation by the side covers from a comparison of Fig. 2(a) and (b), whereas G increases below the 500 Hz band in the case with side covers and the ground as shown in Fig. 2(c).

3. Methods to estimate aerodynamic bogie noise considering the acoustic field

3.1 Estimation procedure

This section outlines the proposed method to evaluate aerodynamic bogie noise by considering the acoustic field. Figure 3 shows schematically the positions of noise source inside the bogie cavity, the microphone array and the wayside observation point. The difference between the conventional and proposed estimation methods is described below. In the conventional method, 2D directive SPL around the bogie section is calculated by a delay and sum method [3] (Step 1) and integrated within a constant region (Step 2). The power of this integrated directive SPL is proportional to that of the noise source. Standard SPLs (measured by the omnidirectional microphone) at the measurement point in the wind tunnel test section are calculated by applying the transfer function obtained experimentally. Then SPLs at a wayside observation point are calculated considering the inverse square law of distance, and finally, aerodynamic bogie noise is estimated (Step 4). Here, the transfer function in Step 3 is obtained through wind tunnel tests in which the flow distribution at the inlet of the bogie section in a leading car is removed to simulate the sleeper direction without side covers to obtain sufficient S/N with a single omnidirectional microphone. Hence, the conditions of aerodynamic source positions and propagation characteristics of sound waves, such as reflection on the ground and insulation by side covers, are supposed to be different from that of the bogie condition with side covers in the inlet flow condition of middle cars [2].

Since the transfer function is affected by the reflection and the insulation around the bogie section, it is desirable to use one which reflects the suitable acoustic field. In the proposed method, the transfer function applied to the integrated directive SPL is obtained considering the acoustic field around the bogie section, and the acoustic power level of the aerodynamic source is estimated (Step 3'). Furthermore, the SPL at the wayside observation point is estimated in consideration of the acoustic field in the same manner. This proce-

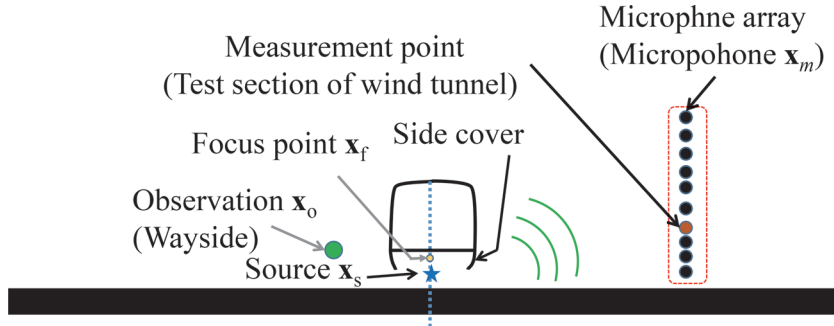


Fig. 3 Positions of noise sources inside bogie cavity, microphone array and wayside observation point

ture clarifies the influence of the reflection due to the ground and cavities or insulation loss by bogie side covers on the integrated directive SPL and produces more credible results.

The procedure of the proposed method is as follows: suppose that one omnidirectional source (virtual source) exists inside the bogie cavity which has a sound power level of L_w^C and that the acoustic wave generated by the source is observed with a microphone array installed beside the train body as shown in Fig. 3. Here, L_w^C is the value which would be 0 dB at the point 1 m away from the virtual source in free space. Sound waves reach each microphone while reflecting on the ground or cavity walls and are attenuated by the side cover. The directive SPLs $L_d^C(f, \mathbf{x}_s, \mathbf{x}_f)$ are represented by a complex Fourier spectrum of the sound wave measured by microphone m , $S_m^C(f, \mathbf{x}_s, \mathbf{x}_m)$ by applying a general delay and sum method.

$$S_m^C(\mathbf{x}_s, \mathbf{x}_f, \mathbf{x}_m, f) = S_m^C(\mathbf{x}_s, \mathbf{x}_m, f) e^{ikr_m^F(\mathbf{x}_f, \mathbf{x}_s)} r_m^F(\mathbf{x}_f, \mathbf{x}_m) \quad (2)$$

$$L_d^C(\mathbf{x}_s, \mathbf{x}_f, f) = 10 \log_{10} \left[\frac{1}{M^2 - M} \sum_{m \neq m'} S_m^C \{ S_{m'}^C \}^* \right] + 94 \quad (3)$$

Here \mathbf{x}_f is the focal point, f is the frequency, k is the wave number, M is the total number of microphones and r_m^F is the distance between the focus point and each microphone in free space. This distance corresponds to the propagation distance in the free field. * indicates the conjugate of the complex number. This directive SPL is influenced by the directive pattern of the microphone array for the acoustic wave emitted from the virtual source which has the power level of L_w^C at position \mathbf{x}_s . Next, the directive SPL inside the analysis region is summed, which yields the integrated SPL, L_1^C . The integrated SPL for the aerodynamic bogie noise, L_1^B measured in the wind tunnel test is also calculated in the same manner. Supposing that the virtual sound source position and directivity are the same as those of the aerodynamic source in the wind tunnel test, the acoustic power of the directive SPL for the virtual sources obtained by Eq. (3) is proportional to that measured by the wind tunnel test at each analysis node. Hence, the power of the integrated directive SPL L_1^C is also proportional to that of the L_1^B .

Here, it is reasonable to expect that aero-acoustic noise sources are distributed inside the bogie cavity, while we only considered one source in the previous discussion. Therefore, a transfer function, $L_1^{CT_a}$, for N uncorrelated virtual sources which have the same acoustic power is determined by Eq. (4).

$$L_1^{CT_a}(f_{\text{oct}}) = 10 \log_{10} \left(\frac{1}{N} \sum_{n=1}^N 10^{\left\{ \frac{L_1^C(f_{\text{oct}}, \mathbf{x}_n^s)}{10} \right\}} \right) \quad (4)$$

Here \mathbf{x}_n^s is the position vector of n -th source and T_{sd} is the distribution pattern of the virtual sources. In the same manner, a relative SPL at a wayside observation point from the multiple sources is expressed in Eq. (5)

$$L^{\beta T_a}(f_{\text{oct}}, \mathbf{x}_0) = 10 \log_{10} \left(\frac{1}{N} \sum_{n=1}^N 10^{\{L^{\beta}(f_{\text{oct}}, \mathbf{x}_n^s, \mathbf{x}_0)/10\}} \right) \quad (5)$$

Here $L^{\beta}(f_{\text{oct}}, \mathbf{x}_n^s, \mathbf{x}_0)$ is the SPL at the wayside observation point \mathbf{x}_0 when a virtual source exists at \mathbf{x}_n^s . Finally, SPL at \mathbf{x}_0 can be estimated by Eq. (6)

$$P_{\text{fin}}(f_{\text{oct}}, \mathbf{x}_0) = L_1^B(f_{\text{oct}}) - L_1^{CT_a}(f_{\text{oct}}) + L_{X_{sd}}^{\beta T_a}(f_{\text{oct}}, \mathbf{x}_0) + A(f_{\text{oct}}) + 10 \log_{10}(2) \quad (6)$$

Here $A(f_{\text{oct}})$ is an A-weighted factor and the last term indicates the contribution of 2 bogies to the noise generated by a gap section between two adjacent train cars passing through.

3.2 Transfer function by numerical calculation

Since amplitude and phases applied to S_m^C in Eq. (2) depend on source and microphone positions, it is difficult to obtain such a large amount of information experimentally. On the other hand, the boundary element method (BEM) is a suitable numerical analysis method for analyzing an acoustic field (Cunefare et al., 1989), and applied for complex model in consideration of diffraction loss. In this study, a Fourier spectrum S_m^C in Eq. (2) is calculated by three-dimensional BEM using a commercial software, SYSNOISE. Figure 4 shows the bogie cavity model used in this numerical analysis. A curved side cover is modeled considering an actual shape. In this study, the bogie itself is not considered. The x and z directions are defined as the main flow and upward directions, respectively, and the y direction is defined as the orthogonal direction to x and z . The range for analysis was set as $x = -500$ to 500 mm, and the microphone array center was set at $x = 500$ in 1/7 scale to match the condition of the wind tunnel test previously carried out [2].

Mesh size was set to be less than 1/6 of the wavelength of analytical frequency. The speed of sound was set to 340 m/s. In calcu-

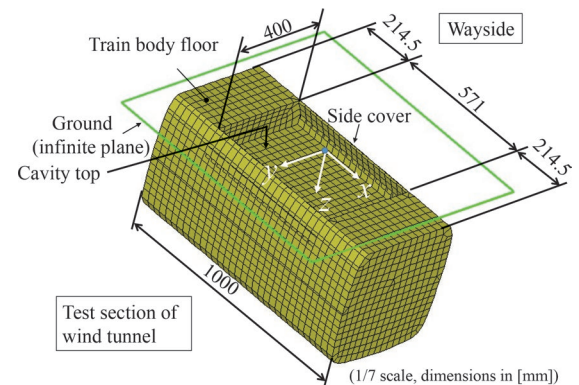


Fig. 4 Bogie cavity model for numerical calculation

lating the transfer function L_1^{CT} , the power of the SPL was averaged for the discrete frequencies at even intervals in common logarithms within a frequency band of the 1/3 octave band. The reflection on the ground was simulated by setting an infinite rigid plane at $z = 0$. The normal incidence reflectivity at the wall is set to 97% (acoustic impedance $27,350 \text{ kg/m}^2\text{s}$). A wayside observation point \mathbf{x}_o was set at $y = 2.716 \text{ m}$ and $z = 0.6 \text{ m}$ (in numerical calculation, $y = -0.388 \text{ m}$, $z = 0.0857 \text{ m}$ in 1/7 scale). Considering that the SPL is measured within the time interval where the gap section between two adjacent train cars is passing in front of the point \mathbf{x}_o , and considering the symmetry of the model shape, L^{β} is averaged by changing $x_o = -200, -100, 0, 100, 200 \text{ mm}$ instead of shifting the train body. Virtual noise sources inside the bogie cavity were arranged as shown in Fig. 5.

3.3 Spatial distribution of transfer function

Spatial distributions of the transfer functions L_1^C and L^β are shown in Figs. 7 and 8. These results are power-averaged for the z direction and plotted on the x - y plane as shown in Fig. 6. The white areas indicate where the SPL in the analysis area is at least 10 dB lower than the maximum SPL indicated in the color bar. It should be noted that change in the transfer function toward the y direction is less than 10 dB in the whole area, while it changes drastically toward the x direction between the 125 to 200 Hz bands. An apparent difference can be observed in the 125 and 160 Hz bands; the SPL peaks at the center in the y direction in the 125 Hz band in both transfer functions, while it reaches the positive ($y = 0.1 \text{ m}$) and negative ($y = -0.1 \text{ m}$) position in L_1^C and L^β respectively at the 160 Hz band. This indicates that these transfer functions are affected by the

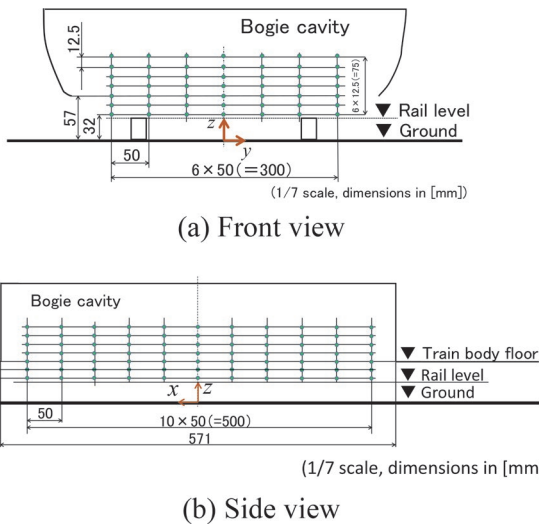


Fig. 5 Arrangement of noise sources inside bogie cavity

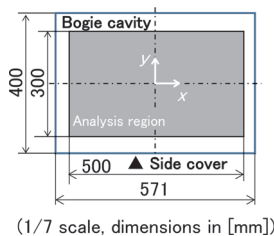


Fig. 6 Analysis region of spatial distribution of transfer functions L_1^C and L^β

acoustic interaction between direct waves passing from a source to the microphone array (or diffraction around the side cover near the measurement point) and the reflected waves on the bogie cavity wall and the ground.

Figure 9 shows the frequency characteristics of the transfer function $L_1^{CT_{sd}}$ and $L^{\beta T_{sd}}$ in the case of the bogie section and free space. Since $L_1^{CT_{sd}}$ which corresponds to the acoustic power of the sources monotonically decreases with increasing frequency, whereas $L^{\beta T_{sd}}$ remains constant, the transfer function ($-L_1^{CT_{sd}} + L^{\beta T_{sd}}$) monotonically increases with increasing frequency. Here, it should be noticed that $L^{\beta T_{sd}}$ for free space is approximately 8 dB, due to the inverse square law of direct distance for a monopole source from a virtual

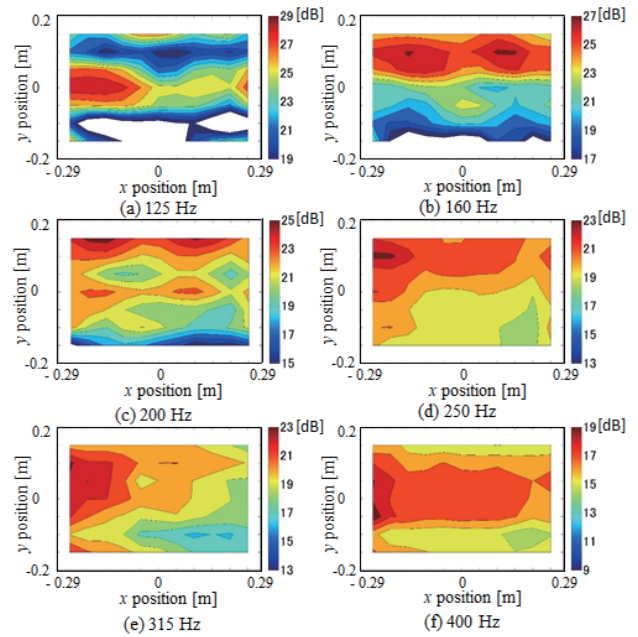


Fig. 7 Spatial distribution of transfer function L_1^C (averaged in the vertical direction)

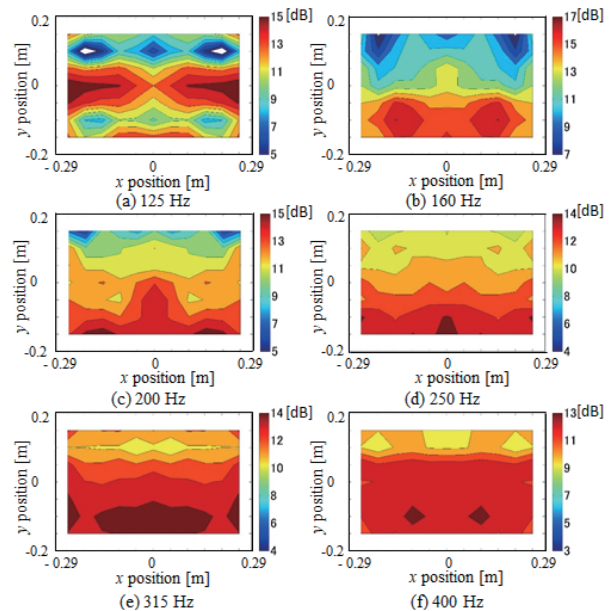


Fig. 8 Spatial distribution of transfer function L^β (averaged in the vertical direction)

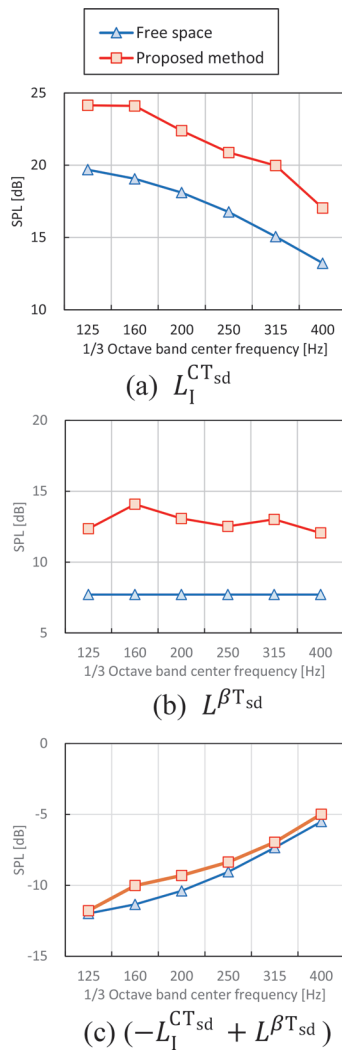


Fig. 9 Frequency characteristics of the transfer functions

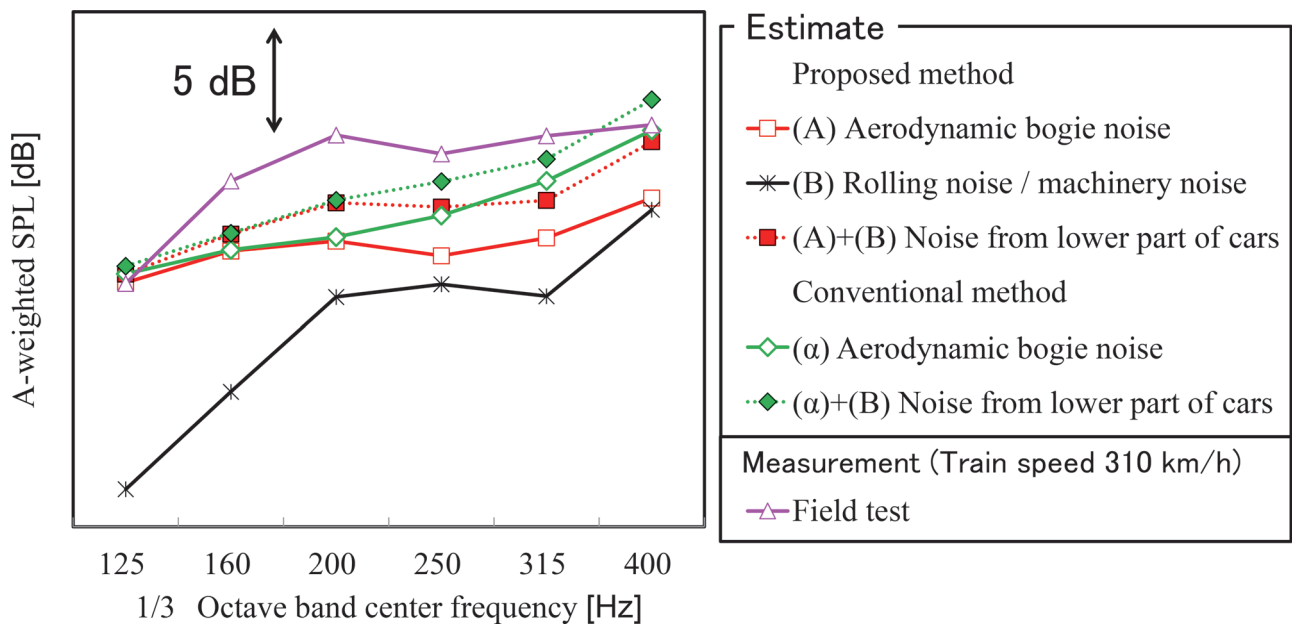


Fig. 10 Noise from the lower part of cars of the Shinkansen train

source inside the bogie cavity to the point x_0 . In the case with the bogie cavity, L_1^{CTsd} and $L^{\beta Tsd}$ increase due to the reflection on the ground and the wall of the bogie cavity, compared to those obtained with the free space. However, these differences from the free space do not significantly affect the estimated SPL at the point x_0 because they are canceled in a resultant transfer function ($-L_1^{CTsd} + L^{\beta Tsd}$).

3.4 Comparison with field test results

We compared the estimated noise from the lower part of cars of Shinkansen trains with field test measurements to evaluate estimated aerodynamic bogie noise. Figure 10 shows the noise from the lower part of cars of the train [5]. Here measured field test data was acquired from near a rail track (a slab track with acoustic barriers, with visibility of the train section from the wayside observation point) while a gap section between two adjacent train cars passed through at an average speed of 310 km/h. Plot (A) is the estimated aerodynamic bogie noise obtained with the proposed method and (B) is the rolling noise and machinery noise estimated using the TWINS model [4]. And (α) is the aerodynamic bogie noise estimated using the conventional method. The train to be analyzed consists of 8 cars, each of which was 25 m long and 3.4 m wide.

The results show that with the conventional method, the difference in the SPL between measured and estimated values at the 160 and 200 Hz bands was larger than that above the 250 Hz band, and that this method overestimated values for the 400 Hz band. On the other hand, in the proposed method, the spectrum shape coincides with that of the field test, i.e., the difference is almost constant from the 160 to 400 Hz bands with an error of less than 3 dB. Hence, the proposed method is a reasonable way to estimate the aerodynamic bogie noise. Here, it should be noted that the proposed method underestimated the SPL from the field tests. One of the suggested reasons for this is that the proposed method does not consider the effect of acoustic reflection caused by acoustic barriers behind the wayside observation point.

4. Conclusion

In this paper, we propose a method to estimate the aerodynamic bogie noise at a wayside observation point using a wind tunnel test. In this method, a transfer function considering an acoustic field around a bogie section is applied in analyzing the spatial source distribution obtained by a 2D microphone array. The results are as follows.

- (1) Aerodynamic bogie noise at a wayside observation point increases due to multiple reflections caused by bogie cavity walls and the ground, below the 500 Hz band.
- (2) Spatial distribution of the transfer function applied to a beam-forming analysis shows that it changes in the sleeper direction drastically at the 125 and 160 Hz bands: it is asymmetrical at the 160 Hz band but it remains almost constant above the 250 Hz band.
- (3) The estimated noise from the lower part of cars obtained by combining the proposed method and the TWINS model coincided with the measured levels at the observation point along a wayside, with an error of less than 3 dB.

References

- [1] Kurita, T., and Mizushima, F., "Environmental Measures along Shinkansen Lines with FASTECH360 High-Speed Test Trains," *JR EAST Technical Review*, No. 16, pp. 47-55, Spring 2010.
- [2] Yamazaki, N., "Evaluation Method for Aerodynamic Noise Generated from the Lower Part of Cars in Consideration of the Characteristics of Under-floor Flows on Shinkansen Trains," *Quarterly Report of RTRI*, Vol. 57, No. 1, pp. 61-68, 2016.
- [3] Flanagan, J. L., Johnston, J. D., and Elko G. W., "Computer-steered microphone arrays for sound transduction in large rooms," *Journal of the Acoustical Society of America*, Vol. 78, No. 5, pp. 1508-1518, 1985.
- [4] Kitagawa, T., and Thompson, D. J., "Comparison of wheel/rail noise radiation on Japanese railways using the TWINS model and microphone array measurements," *Journal of Sound and Vibration*, Vol. 293, Issues 3-5, 13, pp. 496-509, 2006.
- [5] Yamazaki, N., et al., "A method to evaluate the aeroacoustic bogie noise of Shinkansen high-speed trains by considering the acoustic field," *Transactions of the JSME (in Japanese)*, Vol. 85, No. 869, pp. 18-00316, 2019.

Authors



Nobuhiro YAMAZAKI, Ph.D.
Senior Researcher,
Noise Analysis Laboratory,
Environmental Engineering Division
Research Areas: Railway Noise



Takanobu NISHIURA, Ph.D.
Ritsumeikan University
Research Areas: Acoustic Science and
Engineering



Masato NAKAYAMA, Ph.D.
Osaka Sangyo University
Research Areas: Acoustic Signal Processing

Summaries of Papers in RTRI REPORT (in Japanese)

Roller-rig Test of Instrumented Wheelset Utilizing Shear Strains on Wheel Web

Takatoshi HONDO

(Vol.37, No.2, 1-6, 2023.2)

Instrumented wheelsets are widely utilized in railway industries for the purpose of the measurement of wheel-rail interaction forces. In the conventional instrumented wheelset, the measurement accuracy of lateral forces is reduced due to the bending moment induced by wheel loads. The authors have proposed a new configuration of the instrumented wheelset to reduce the influence of the wheel load on the measurement of the lateral force. This proposed configuration utilizes the shear strains of wheel webs as a measure of lateral forces. This paper describes the accuracy verification of the proposed configuration under wheel rotating conditions. Single-wheelset roller-rig tests are carried out and the test results show that the proposed method can reduce the influence of wheel loads even under rotating conditions.

Experimental Verification of Handrail Effect on Injury Reduction for Passengers Seated in Long Seats in the Event of Collision

Kazuma NAKAI, Shota ENAMI

(Vol.37, No.2, 7-12, 2023.2)

In order to enhance the safety of passengers seated in long seats, it is important to identify the risk to passengers in the event of a collision. In a prior study, case studies using numerical analysis showed that the installation of handrails reduced the secondary impact velocity of the passenger's head. The purpose of this study is to investigate the effect of handrails in reducing the severity of injury to passengers by some physical tests. The experiment results showed that passengers seated third from bench-end partitions in long seats are at higher risk, and that the severity of head and thorax injury decreased significantly because of handrails.

Track Maintenance Using Track Irregularity Anomaly Detection Method Based on Cluster Analysis

Mami MATSUMOTO, Masashi MIWA, Tatsuo OYAMA

(Vol.37, No.2, 13-18, 2023.2)

When a train repeatedly runs on a track, track irregularities, which are the distortion of tracks, gradually increase by wheel loads. The track irregularity is normally inspected periodically to perform a maintenance when a large track irregularity is detected. However, in rare cases, the track irregularity may increase locally and rapidly. To ensure the safety of train operation, preventive maintenance is required to detect the signs of such rapid increase of the irregularity to perform maintenance before it occurs. In this study, to identify a location in advance where large track irregularities are likely to occur, we have developed a mathematical model for the identification by applying the cluster analysis to historical data of track irregularity and maintenance records.

Evaluation Method of Growth Process of Rail Corrugation by Monitoring Rail Vertical Vibration

Hirofumi TANAKA, Kazuhiro KAJIHARA

(Vol.37, No.2, 19-24, 2023.2)

Rail corrugations cause noise, vibrations and deterioration of track components, which increase the frequency of track maintenance work. However, a measurement method that efficiently evaluates the growth of rail corrugation has not been established. The authors of this paper have developed a monitoring system for rail corrugations that enables long-term remote measurement of rail vibrations by means of battery-powered accelerometers

and a wireless sensor network. In this study, the relationship between rail vertical vibration characteristics and actual rail corrugations measured on business line was investigated to verify the applicability of the developed system for identifying the growth process of rail corrugations.

Test Method for Loading Tracks Composed of a Set of Rail Fastening Systems for Rail Joints

Shingo TAMAGAWA, Tadashi DESHIMARU, Tomoyuki YAMAMOTO

(Vol.37, No.2, 25-31, 2023.2)

This study aims to establish a test method for loading test tracks composed of a set of rail fastenings for rail joints. The authors of this paper constructed FEM models for railway tracks which represent rail joint parts accurately and performed the FEM analysis. The FEM results are in good agreement with the results of a loading test on a test track composed of plural sets of rail fastenings. On the basis of the FEM model, the authors proposed the test method for loading test tracks composed of a set of rail fastenings and compared the test results of a set of rail fastenings and plural sets of rail fastenings. The results show that rail head displacement and rail tilting angles obtained from a single set of rail fastenings are in good agreement with those obtained from plural sets of rail fastenings. Therefore, the proposed method based on the FEM model is available to evaluate the performance of rail fastenings system for rail joints.

Evaluation Method for Seismic Active Earth Pressure Acting on Back of Retaining Wall with Cohesive Backfill

Takumi OZAKI, Susumu NAKAJIMA, Taisuke SANAGAWA

(Vol.37, No.3, 1-7, 2023.3)

In Japan, seismic reinforcement of retaining walls has been actively carried out. In the current Japanese seismic design standard of railway structures, seismic active earth pressure is evaluated without taking account of backfill cohesion effect. However, the approach results in an overestimation of seismic active earth pressure acting on the retaining wall. On the basis of the above, by conducting a series tests using models, the authors aim to clarify the effect of backfill cohesion on appearing characteristics of seismic active earth pressure acting on retaining walls in this study. The authors propose an evaluation method for seismic active earth pressure considering the effect of cohesion mobilized on failure planes and the adhesion force mobilized on the back surfaces of retaining walls.

Recovery Mechanism on the Lateral Resistance of Ballasted Track by Stabilization Work

Takahisa NAKAMURA, Maiku TAKAURA, Takahiro KAGEYAMA, Yohei HAYAKAWA

(Vol.37, No.3, 9-15, 2023.3)

On ballasted tracks, it is known that the lateral resistance of track beds is reduced by performing tamping work and restored by track bed stabilization work using stabilizers. However, the mechanism in which the lateral resistance changes due to these operations has not been sufficiently investigated. In this study, we measured the lateral resistance properties on each side of sleepers by tamping work and stabilization work using a 1/5 scale model test. The results show that the recovery mechanism of the lateral resistance by stabilization work has been clarified.

Numerical Analysis Method for Corrosion of Segment Joint of Shield Tunnel Caused by Chloride Attack

Kaho KINOSHITA, Takashi USHIDA
(Vol.37, No.3, 17-22, 2023.3)

Deterioration caused by chloride ions may occur in some shield tunnels located in waterfront areas or near tidal rivers. In this paper, we propose a three-dimensional finite element method for the maintenance of shield tunnels effected by chloride ions. In proposing this method, we developed a modeling method for deteriorated segment joints by reducing stiffness. In addition, we verified the validity of the method by loading tests of tunnel lining specimens.

Methods for Applying Public Communication Network to Communication-Based Train Control Systems

Takayasu KITANO, Akihiro GION
(Vol.37, No.3, 23-28, 2023.3)

A method for applying public communication networks to communication-based train control systems is proposed. The application of public communication networks to train control systems differs from conventional systems in that transmission lines which cannot be controlled by railway operators, intervene between safety equipment. Therefore, in order to construct a system in which safety techniques can be applied without depending on transmission lines, a configuration in which train control function and information transmission are independent of each other is presented. Furthermore, threats posed by information transmission function from the perspective of the train control function and countermeasure requirements are presented, as well as implementation methods which satisfy these requirements at the current techniques.

Designing Auditory Warnings for Preventing Arousal-Level Decline during Train Operation and Examining its Effectiveness

Kei HOSHINO, Ayako SUZUKI, Masahiro HONDA, Takeshi HARA
(Vol.37, No.3, 29-35, 2023.3)

Train driving is characterized by late-night and early-morning shifts when operators may be prone to drowsiness. This study developed and evaluated a system aimed at maintaining and improving arousal level by presenting auditory warnings. First, auditory warnings were designed based on survey of the opinions of train operators. In our experiments, designated auditory warnings were scored and selected in terms of three conditions ("audibility," "distinctiveness," and "arousal function") under train noise. The result shows that the arousal effects of the warning auditory were confirmed by presenting the designed sound during a monotonous task with the train driver environment.

Evaluation of Relationship between Water Flow Rate and Tangential Contact Force of Wheel/Rail Using Twin-disc Rolling Machine

Daisuke YAMAMOTO
(Vol.37, No.4, 1-7, 2023.4)

In this study, to investigate the effects of various experimental conditions such as circumferential velocity of the test wheel, amount of water spray, and contact pressure on the tangential contact force characteristics, experiments to measure the tangential contact force were carried out at a maximum circumferential velocity of 130 km/h. The results show that a small amount of water on the contact surface has a great influence on a decrease in the tangential contact force. Furthermore, it is clarified that the amount of water between actual wheels and rails when running in rainy conditions may be extremely small, when the amount of water intervenes on the contact surface is considered as an inverse problem from the experimental re-

sults under several water flow rate conditions. This tendency is similar for all contact pressure conditions and is qualitatively consistent with the actual phenomenon.

Numerical Analysis of Local Scour Around Pier Based on 3D Movements of Sediment Particles

Hidegori ISHII, Kohei MUROTANI, Koji NAKADE
(Vol.37, No.4, 9-15, 2023.4)

This paper describes a numerical model developed to simulate the flow and scour around a bridge pier. The flow is modeled by large eddy simulation. The morphological change of riverbeds is calculated by coupling sediment transport with models for sediment pick-up and deposition. The sediment transport is calculated by 3D momentum equations of sediment particle. Sediment pick-up and deposition are modeled by stochastic models for the purpose of reducing computational demand. The numerical model was applied to the local scour around a vertical cylinder pile under clear water condition. The results agreed well with experimental data, except shape of downstream riverbed. It is concluded that this model can evaluate a local scour on the upstream side considering 3D movements of sediment particles.

Evaluation of Service Life of Aged Prestressed Concrete Sleeper

Tsutomu WATANABE, Keiichi GOTO, Shintaro MINOURA, Manabu IKEDA
(Vol.37, No.4, 17-23, 2023.4)

PC sleepers have been treated as replacement track materials that are replaced each time deformation occurs. For this reason, currently no criteria have been established for quantitative soundness assessment nor for replacement of sleeper. In this research, to establish a new maintenance management system, we collected aged PC sleepers, conducted a survey of aging deterioration, conducted various tests such as bending tests specified by JIS, and evaluated the load-bearing capacity of aged PC sleepers through numerical analyses using a three-dimensional FEM model. Based on these results, a guideline for the service life of PC sleepers was proposed.

Rail Profile Selection Method to Reduce Gauge Corner Cracking Initiation

Masahiro TSUJIE, Masaharu KONO, Yoshiaki TERUMICHI
(Vol.37, No.4, 25-32, 2023.4)

Gauge corner cracking (GCC) occurs on heat treated rails of the high rail in curved sections with a radius of 600 to 800 m. In our previous research, we proposed a countermeasure method for suppressing the GCC initiation by applying a rail with worn profiles to the high rail in curved sections to reduce contact pressure between wheel and rail. In this study the cross-sectional rail profile that is the most effective in suppressing crack initiation was selected by numerical analysis for the high rail in curved sections with a radius of 600 to 800 m.

Inspection System for Evaluating Wooden Sleeper Deterioration Using Image Analysis of Video

So KATO, Yosuke TSUBOKAWA, Nozomi NAGAMINE, Wataru GODA, Riho MAEDA, Kensuke ITOI
(Vol.37, No.4, 33-38, 2023.4)

In order to save labor work in inspecting track facilities using a low-cost and simple inspection system, we have developed a system for inspecting wooden sleepers using forward view images of camcorders from train cabs. The system uses deep learning to judge the deterioration of wooden sleepers from images. In this paper, we report the outline of the system: judgment accuracy, and verification results to see if the progress of deterioration can be assessed.

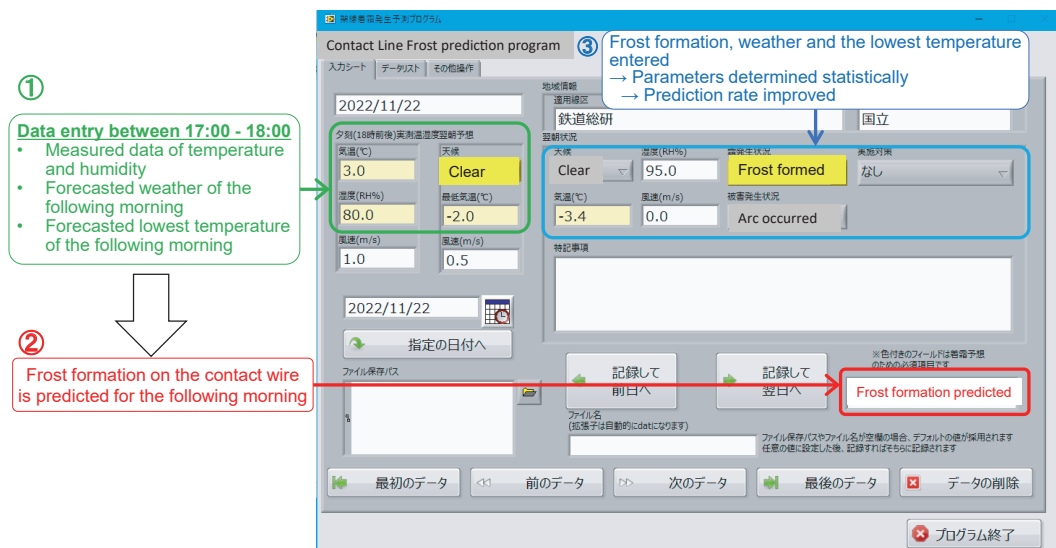
May 2023 Vol. 64 No. 1 - No. 2

- 5th generation mobile communication system, 103
 8-figure shaped coil, 67
 abnormality detection, 90
 acceleration integration, 115
 acceleration test, 96
 acoustic numerical calculation, 142
 acoustic theory, 135
 aerodynamic brakes, 86
 aerodynamics, 86
 Analytical Study on the Influence of Friction on Unstable Oscillation of Pantograph (P), 109
 autonomous train operation, 77
 ballast scattering, 86
 battery powered train, 67
 beam theory, 115
 bridge seismic isolation, 81
 camera, 90
 capacitor self-excitation phenomenon of induction machines, 49
 CBM, 96
 CFD, 129
 compact Green's function, 135
 Configuration and Safety Confirmation Method of Image Processing System
 Applicable to Signalling Systems (P), 90
 critical current, 56
 cross wind, 86
 deflection monitoring, 115
 design standard, 1
 Development of Inverter-less Excitation Method for a Linear Rail Brake (P), 49
 Development of Simulator to Accurately Reproduce Snow Accretion Phenomenon for Railway Vehicles Traveling in Snowy Areas (P), 121
 digital maintenance, 77
 digital technology, 77
 disaster prevention, 43
 early recovery, 7
 earthquake early warning, 33
 effective rainfall index, 43
 electromagnetic excitation tests, 61
 electronic signalling equipment, 96
 Evaluation of Vibration Resistance of Levitation and Guidance Ground Coils by Electromagnetic Excitation Tests Using a Superconducting Magnet (P), 61
 excitation system, 49
 Fabrication and Characterization of High-temperature Superconducting Materials with High Magnetic Field (P), 56
 feeder cable, 11
 fluid dynamics, 129
 FRMCS, 103
 ground coils, 61
 high temperature superconductivity, 56
 highspeed test facility for pantograph/OCL system, 81
 high-speed train, 129
 high-temperature superconductivity, 11
 hybrid train, 67
 image measurement, 81
 image processing, 90
 Improvement in Rapidness of Earthquake Early Warning Using Ocean Bottom Seismic Data (P), 33
 inlet, 129
 invert, 16
 lifetime, 96
 Lifetime Estimation of Electronic Signalling Equipment Based on Sensing Data from Usage Environment (P), 96
 linear motor, 49
 lining, 16
 Local 5G, 103
 longitudinal direction, 27
 maglev, 11
 Maglev Technology and Research Trends on Superconductivity (Per), 11
 magnetic field, 56
 maintenance, 43
 Measures Against Snow Accretion Around Shinkansen Bogies Using Running Wind (P), 129
 Method for Updating Operational Regulation Standards Considering Seismic Risk of Railway Facilities (P), 37
 Method to Evaluate Aerodynamic Bogie Noise from Shinkansen High-speed Trains by Considering Acoustic Fields (P), 142
 microphone array, 142
 model experiment, 129
 mountain tunnels, 16
 moving model rig, 135
 ocean bottom seismic data, 33
 onboard measurement, 81
 operation control, 7
 operation regulation, 43
 operational regulation standards, 37
 pantograph, 109
 Performance Verification of Design Method for Plain Concrete Linings and Inverts Assuming Ground Displacement after Completion (P), 16
 performance-based design, 16
 performance-based design method, 27
 performance-verification design method, 1
 power storage, 11
 processing method, 61
 Proposal of Snowmelt Disaster Warning Criteria Using Effective Rainfall Index Which Reflects Snowmelt (P), 43
 public network, 103
 P-wave alarm, 33
 rail brake, 49
 railway noise, 142
 real-time hazard map, 7
 rebar stress, 115
 Recent Research and Development on Disaster Prevention Technology (Per), 7
 Recent Research on Railway-specific Dynamic Issues (Per), 81
 Recent Studies on Railway Aerodynamics (Per), 86
 Recent Trends in Design Technology for Railway Tunnels and Summary of Revisions in Design Standards for Railway Tunnels (Per), 1
 recharging, 67
 Reducing Micro-pressure Waves Using Train Nose Optimization Based on Linear Acoustic Theory (P), 135
 RESEARCH 2025, 77
 safety, 90
 segment, 22
 seismic countermeasures, 37
 seismic design, 27
 Seismic Design Method for Shield Tunnels in Ground Conditions Subject to Change in the Longitudinal Direction (P), 27
 seismic risk, 37
 severe disaster, 7
 shield machine, 22
 shield tunnel, 22, 27
 sliding friction, 109
 slope, 43
 snow accretion, 86, 129
 snow accretion analysis method, 121
 snow accretion for a train bogie, 121
 snow melting, 43
 stability analysis, 109
 strong local wind, 81
 structural optimization, 81
 structural performance, 115
 Structural Performance Evaluation of Existing Bridges Based on Acceleration Monitoring (P), 115
 superconducting bulk, 56
 superconducting magnet, 11, 61

temperature, 96
train draft, 86
train operation, 103
transfer function, 142
trend analysis, 22
Trend Analysis of Segments and Tunnel Boring Machines for Railway
Shield Tunnels (P), 22
Trends in Research and Development Activities Related to Railway Signal-
ling and Telecommunication Systems (Per), 77
tunnel, 1
tunnel pressure fluctuation, 86
two-way coupling analysis, 121
unstable oscillation, 109
usage environment, 96
Verification of the Applicability of Fifth Generation Mobile Communication
Systems to Railway Operations (P), 103
verification procedures, 16
wireless power transfer, 67
Wireless Power Transfer System for Railway Vehicles with Improved Pow-
er Density of Onboard Coil (P), 67

RTRI Develops a Program to Predict Frost Formation on the Contact Wire

RTRI Developed a Program to Predict Frost Formation on the contact wire to accurately predict frost formation on the contact wire on the early winter morning based on the weather data along the railway line. This program will be useful to efficiently implement measures to prevent frost formation on the contact wire.



A screen displaying the predicted result of the program

QUARTERLY REPORT of RTRI

第 64 卷 第 2 号

2023 年 5 月 1 日 発行

監修・発行所：公益財団法人鉄道総合技術研究所

〒 185-8540 東京都国分寺市光町 2-8-38

発行人：芦谷公稔

問い合わせ：鉄道総研広報

Vol. 64, No. 2

Published date: 1 May 2023

Supervision/Publisher: Railway Technical Research Institute

Address: 2-8-38 Hikari-cho, Kokubunji-shi, Tokyo 185-8540, Japan

Issuer: Dr. Kimitoshi ASHIYA

Contact us: Public Relations, Railway Technical Research Institute

Mail Address: www-admin @ rtri.or.jp

QUARTERLY
REPORT of
RTRI